A DYE – SENSITIZED SOLAR CELL MODULE WITH ENHANCED CHARGE COLLECTION EFFICIENCY

AZHAR FAKHARUDDIN

Dissertation submitted in fulfilment of the degree of
Doctor of Philosophy in
Advanced Materials

FACULTY OF INDUSTRIAL SCIENCE & TECHNOLOGY
UNIVERSITI MALAYSIA PAHANG

February 2015

THESIS CONFIDENTIAL STATUS

UNIVERSITI MALAYSIA PAHANG

DECLARATION OF THE THESIS AND COPYRIGHT

Author's full name: AZHAR FAKHARUDDIN

Date of birth: 20/07/1987

Title: "A DYE – SENSITIZED SOLAR CELL MODULE WITH ENHANCED CHARGE COLLECTION EFFICIENCY"

Academic Session : 2014/2015

I declare that this thesis is classified as:

CONFIDENTIAL (Contains confidential information under the official Secret Act 1972)*

☐ **RESRICTED** (Contains restricted information as specified by the organization where research was done)*

☐ **OPEN ACCESS** I agree that my thesis to be published as online open access (Full text)

☐ I acknowledge that Universiti Malaysia Pahang reserve the right as follows:

1. The Thesis is the Property of Universiti Malaysia Pahang
2. The Library of Universiti Malaysia Pahang has the right to make copies for the purpose of research only
3. The Library has the right to make copies of the thesis for academic exchange

Certified By:

____________________	____________________
(Student's signature)	(Signature of Supervisor)
Azhar Fakharuddin	Prof. Jose Rajan
(Student)	(Name of Supervisor)
Date :	Date :

SUPERVISOR'S DECLARATION

I hereby declare that I have checked this thesis and in my opinion, this thesis is adequate in terms of scope and quality for the award of the degree of Doctor of Philosophy in Advanced Materials.

Signature ______________________________
Name of Supervisor: Jose Rajan
Position: Professor, Faculty of Industrial Science & Technology
Date: 5 February 2015

STUDENT'S DECLARATION

I hereby declare that the work in this thesis is my own except for quotations and summaries which have been duly acknowledged. The thesis has not been accepted for any degree and is not concurrently submitted for award of another degree.

Signature ____________________
Name: Azhar Fakharuddin
ID number: PKD11005
Date: 5 February 2015

'To those who live for humanity'

ACKNOWLEDGEMENT

First and foremost, I am thankful to Almighty Allah (SWT) for the strength granted to complete my PhD journey.

I would like to express my sincere gratitude to my supervisor Prof. Jose Rajan for his continuous support during my PhD research, for his patience in teaching me, guiding and correcting me and for sharing his immense knowledge. I couldn't have reached this stage without his support. I am ever grateful to him for "teaching me how to fish" instead of "giving me the fish"!

I would like to thank the postgraduate school of my university for awarding me a doctoral scholarship, my faculty members for their comments and feedback during seminars and colloquiums, the technical team of my department for their cooperation in my lab work, my group members especially Irfan and Qamar for being so helpful and patient with me, and to Salman for useful discussions throughout.

I would also like to thank Dr. Ivan Mora-Sero of UJI Spain for discussion on my research work, Professor Juan Bisquert of UJI Spain for his comments on diffusive volume and also on the "future of DSM technology", Dr. James Jennings of NUS Singapore for useful discussion on impedance spectroscopy modelling of DSCs and diffusion length, and Professor Thomas M. Brown of URTV Rome, Italy for his opinions on DSM cost analysis, and the potential future of the technology.

My deepest gratitude to my beloved father who has always been my mentor, siblings for the continuous prayers, sacrifice, love and support, and to my beautiful wife who has been so patient and supportive throughout my study. This would not have been possible without her love and compassion through these difficult years. "*Thangssss*"

Finally, I appreciate the financial support from Ministry of Higher Education Malaysia (MOHE) under FRGS 120102 and PRGS 120801.

Azhar, February 2015

ABSTRACT

Intense research in the field of dye-sensitized solar cells (DSCs) brought them to a level of delivering ~13% efficiency (η) using mesoporous TiO_2 particles, inorganic dyes, and redox electrolyte. High η and IPCEs are so far reported in devices of rather smaller area (≤ 0.2 cm^2), a size that put limitations on the scalability of the device. On the other hand, large area modules (DSMs) are developed by up scaling the DSCs to give either added voltages (series connection), such as S –type, W–type and Z–type, or currents (parallel connection) with appreciable output voltage (~8 V) and current (~2 – 3 A), respectively, in separate devices of active areas in the 20 – 1000 cm^2 range. The highest achieved η in DSMs is ~ 8.2%, ~36% smaller than their laboratory scale devices. We note that such designs are invariably built in the form of interconnected TiO_2 strips (≥ 3 cm^2) and the photocurrent density (J_{SC}) in these designs is merely 30 – 50 % then that of single cells.

We have investigated the effects of DSC photoelectrode area upon its η and identified that, within the limits of our study, threshold area is the key in achieving the J_{SC} and clearly not the expanded photoelectrode area as adopted conventionally in a DSM fabrication. Upon increasing the photoelectrode area, the η decreased biexponentially, the main contributor to which was the $J_{SC.}$ The upshots of the electrochemical studies revealed that the electrons from an area above a threshold are never collected due to a competition between electron lifetime (τ_n) and transit time (τ_d). We suggest that if larger electrodes are fabricated, then electrons from smaller spatial domains contribute to the short circuit current density. The diffusion length (L_n) in DSCs, which is defined as the distance travelled by electrons before recombining with the hole species in electrolyte, $L= (D_n \tau_n)^{1/2}$, where D_n is the electron diffusivity, considered only film thickness so far. Our findings reveal that area of the electrode is also to be considered when the L is defined.

Based on the insights, we fabricated alternative designs to build DSMs with increased charge collection (η_c). In our specially designed experiments, we altered the photoelectrode design by splitting the electrode into multiple fractions to restrict the electron diffusion pathways. We observed a correlation between the device physical dimensions and its charge collection efficiency via current-voltage and impedance spectroscopy measurements. Our electrode designs showed >50 % increased J_{SC} due to shorter τ_d, higher recombination resistance and 20 – 50% higher η_c compared to the conventional ones despite their similar active volume (~3.36 × 10^{-4} cm^3). If high efficiency DSCs is targeted using commercial TiO_2 paste on account of its high specific surface area, results from our studies would be helpful in designing new device structures to build high efficiency DSMs.

ABSTRAK

Penyelidikan yang giat dalam bidang sel suria terpeka pewarna (dye-sensitized solar cells (DSCs)) telah membawa ke tahap penyampaian ~13% kecekapan (η) menggunakan zarah mesoporous TiO_2, pewarna tidak organik, dan elektrolit redoks. Ketinggian η dan IPCEs setakat ini dilaporkan di dalam peranti yang agak kecil luasnya (≤ 0.2 cm^2), saiz yang meletakkan batasan ke atas kebolehukuran peranti. Selain itu, modul berkeluasan besar (large area modules (DSMs)) dihasilkan dengan menambahukur DSCs yang bertujuan menambah voltan (sambungan bersiri), seperti jenis S, jenis W dan jenis Z, atau arus (sambungan selari) dengan output voltan yang jelas (~8 V) dan arus (~2 – 3 A), masing-masing, dalam peranti berasingan yang mempunyai keluasan aktif dalam julat 20 – 1000 cm^2. Tahap tertinggi η dalam DSM yang tercapai ialah ~ 8.2%, iaitu ~36% lebih kecil daripada peranti skala makmal. Kami mengenalpasti bahawa rekabentuk ini dibina secara tetap dalam bentuk strip TiO_2 (≥ 3 cm^2) dan ketumpatan fotoarus (J_{SC}) dalam rekabentuk ini adalah hanya 30 – 50 % daripada yang digunakan untuk sel tunggal.

Kami telah mengkaji kesan-kesan luas fotoelektrod DSC terhadap η dan mendapati, dalam linkungan kajian ini, luas ambang adalah kunci dalam mencapai J_{SC} dan bukan luas fotoelektrod yang besar seperti digunapakai secara konvensional dalam fabrikasi DSM. Setelah penambahan keluasan fotoelektrod, η berkurangan secara biesksponen,dengan penyumbang utama adalah $J_{SC.}$ Hasil kajian elektrokimia menjelaskan bahawa elektron dari luas lebih tinggi dari luas ambang tidak dikumpul disebabkan persaingan di antara jangka hayat (τ_n) dan masa transit (τ_d). Dicadangkan bahawa jika elektrod yang lebih besar direka, maka elektron dari domain berkeluasan lebih kecil menyumbang kepada kepadatan arus litar pintas. Panjang difusi (L_n) dalam DSC, yang ditakrifkan sebagai jarak perjalanan elektron sebelum bergabung semula dengan cas positif dalam elektrolit, $L= (D_n \tau_n)^{1/2}$, di mana D_n ialah kebolehsebaran elektron, yang setakat ini mengambil kira ketebalan filem. Penemuan ini membuktikan bahawa luas elektrod mesti diambil kira apabila L_n ditakrifkan.

Berdasarkan pengetahuan ini, kami menghasilkan rekabentuk alternatif DSM yang boleh dibina dengan menambahpengumpulan cas (η_c). Dalam eksperimen ini yang direka khas, kami mengubahsuai rekabentuk fotoelektrod dengan memecahkan elektrod ke beberapa pecahan untuk mengehadkan laluan difusi elektron. Pemerhatian menunjukkan korelasi antara dimensi fizikal peranti dan keberkesanan pengumpulan cas melalui arus-voltan dan pengukuran impedans spektroskopi. Rekabentuk elektrod kami menunjukkan >50 % peningkatan J_{SC} disebabkan τ_d yang lebih pendek, rintangan rekombinasi yang lebih tinggi dan 20 – 50% η_c lebih daripada kaedah konvensional meskipun isi padu aktif yang sama (~3.36×10^{-4} cm^3). Jika DSC berkecekapan tinggi disasarkan menggunakan pes TiO_2 komersil disebabkan luas permukaan spesifik yang tinggi, keputusan kajian ini akan membantu dalam merekabentuk struktur peranti baru dalam membina DSM berkecekapan tinggi.

LIST OF FIGURES

Figure number **Page no.**

LIST OF TABLES

LIST OF ABBREVIATIONS

BIPVs	Building integrated photovoltaics
CE	Counter electrode
CPE	Constant phase element
DSCs	Dye-sensitized solar cells
DSMs	Dye-sensitized solar modules
DSPs	Dye solar panels
EIS	Electrochemical impedance spectroscopy
FF	Fill factor
FTO	Fluorine doped tin oxide
HTM	Hole transport media
I-V	Current-Voltage
J_{SC}	Short circuit current density
l-DSCs	Liquid electrolyte based dye-solar cells
PCE	Photoconversion efficiency
PV	Photovoltaic
s-DSCs	Solid-state dye solar cells
SEM	Scanning electron microscopy
TCO	Transparent conducting oxide
UV	Ultraviolet
V_{OC}	Open circuit voltage
WE	Working electrode
XRD	X-ray diffraction

LIST OF SYMBOLS

R_T	Charge transport resistance
R_{CT}	Recombination resistance
R_S	Series resistance
R_{SH}	Shunt resistance
ξ	Molar extinction coefficient
τ_n	Electron lifetime
τ_d	Electron transit time
C_μ	Chemical capacitance
α	Absorption
Φ_a	Absorption efficiency
η_c	Electron collection efficiency
Φ_{IN}	Electron injection efficiency
η	Photoconversion efficiency
ω_{rec}	Recombination frequency
μm	Micrometer
η_{cc}	Collection efficiency
L_n	Diffusion length
L or d	Photoelectrode thickness
W	Watt

TABLE OF CONTENTS

Page

CHAPTER 1

INTRODUCTION

1.1 RESEARCH BACKGROUND

1.1.1 An Overview of Global Energy Scenario

Primary supply of clean and sustainable energy is one of the top global issues. A greater portion of today’s energy demand (>85%) is fulfilled by fossil fuel based resources but at the expense of the global warming and consequent severe impact on climate changes (IEA, 2013). The statistics of increasing energy demand and depleting fossil fuels are alarming: (i) the energy demand is expected to increase 2 folds by 2050; and (ii) due to depleting fossil fuel reserves an additional energy demand equal to today’s total energy consumption is expected in next three decades (Grätzel, M., 2009 and Perez et al., 2011). The renewable energy resources such as solar and wind which are cost effective and abundant in nature are fairly distributed across the globe; and therefore, have potential to contribute towards this energy gap (Nelson J., 2013). These resources also eliminate the environment issues associated with the use of fossil fuels. Among the renewable energy resources, solar energy alone has a potential to meet world’s primary energy demand; it requires covering less than 0.4% of our planet’s surface with 15% efficient solar panels (Docampo et al., 2014). Alternatively, using 25% efficient solar panels, a solar farm of area ~400 km × 400 km in the Sahara desert would meet the projected energy demand. Above all, energy from sunlight is 200 times more abundant than all other renewable energy resources combined (Perez, et al., 2011).

1.1.2 Emergence of Photovoltaic Technology

Photovoltaic effect was discovered in the 19th century by Edmond Becquerel. Subsequently, solar energy appears not only as a promising alternative energy resource but also a better off–grid choice in remote applications and in portable electronics. The solar cell technology is divided into three types, (i) crystalline silicon solar cells, (ii) thin film solar cells ($CuInGaSe_2$, CdTe etc.), as their working electrodes comprise much thinner film (typically ~1 μm thick) compared to first generation, and (iii) molecular absorber solar cells in which molecules or inorganic clusters are the primary absorbers. Examples of the last type are polymer solar cells, dye-sensitized solar cells (DSCs), quantum dot solar cells, and recently emerged perovskite solar cells. Over half a century research in silicon based solar cells, which currently dominate the photovoltaic market, resulted in an installed capacity of greater than 40 GW till date, up from 1.5 GW in 2000 as shown in Figure 1.1 (British Petroleum, 2013).

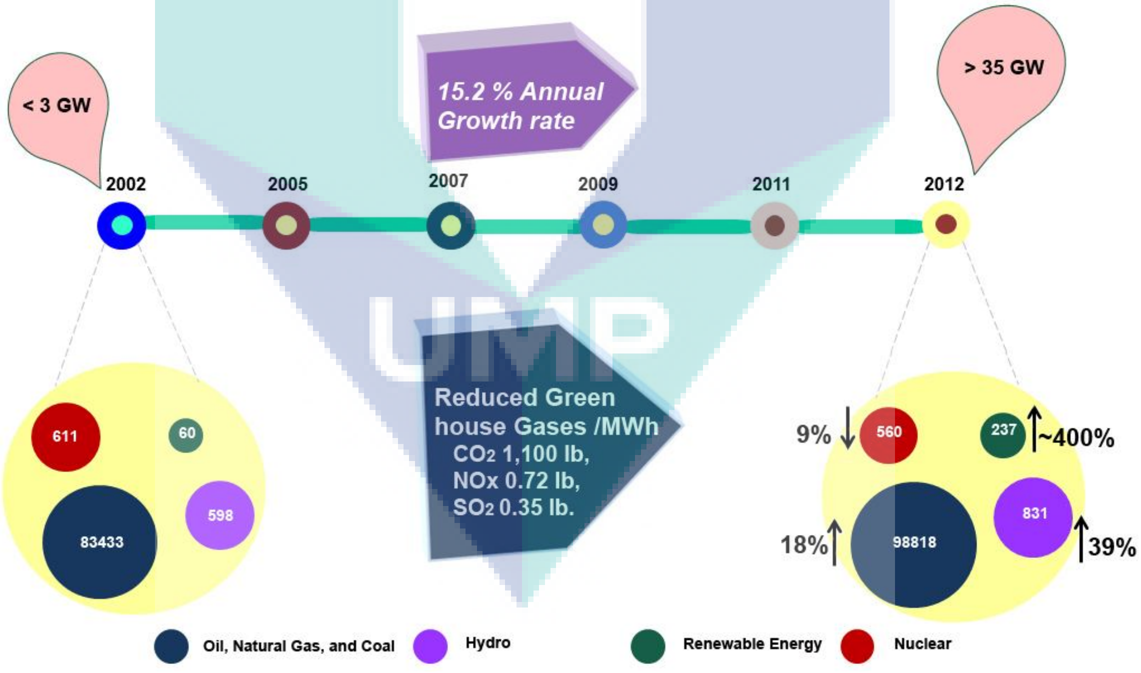

Figure 1.1: A chart showing paradigm shift of the share of renewable energy resources. The values are in million tons of oil equivalents (mtoe).

Source: Fakharuddin A. et al. 2014d

These installations brought solar cells (mostly silicon based) to contribute to energy demand in peak hours; in Germany ~5.3% of daily demand is fulfilled by solar electricity which increases to 20% in longer sunny days (Nelson J., 2013; Wirth, 2013). Commercial modules of silicon solar cells (first generation) of efficiency (η) ~20% are available in the market. On the other hand, thin film solar cells (second generation) based on $CuInGaSe_2$ (CIGS) have achieved η>20% at laboratory scale (ZSW, 2013; NERL, 2014); and modules of η ~15% are commercially available (First Solar, 2013). Despite the rapidly increasing global installations, these solar cells (first and second generation) still suffer from critical issues such as longer payback time (2 – 4 years), high cost associated with extreme purity requirement of the active material, scarcity of materials such as indium and silver, and their low working capability in cloudy hours or in shaded region (Hardin et al., 2012 and Nelson J., 2013). These drawbacks bring into account the third generation photovoltaics, resolving most of the issues of the first two generations. However, the third generation devices currently suffer from lower photoconversion efficiency (η) than the other two.

1.1.3 Molecular absorber solar cells

In general, a solar cell absorbs solar irradiations using a semiconducting material and converts it into electrical energy by splitting up an electron–hole pair (exciton) during absorption. The exciton is separated into mobile carriers at the p–n junctions in silicon solar cells; the charges thereby produced are required to travel ~300 μm thick photoanode layer. A complete collection of photogenerated electron from such thick layer puts stringent conditions on purity of the materials. The second generation solar cells are although few microns thick, their vacuum based fabrication to improve the crystallization of $CuIn_xGa_{1-x}Se_2$ (CIGS) films increase the cost of device fabrication. The molecular absorber solar cells offer remedy to such undesirable fabrication cost; they typically do not require a clean room for fabrication and are often compatible with roll–to–roll industrial production. Among various third generation solar cells, the dye sensitized solar cells (DSCs) are promising as they are light weight, transparent and can be made on flexible substrates. Due to their significantly shorter film thickness (~15 μm), they do not need high quality semiconductors as the photogenerated electrons require relatively shorter transit length compared to silicon solar cells. DSCs offer the second highest photoconversion efficiency (η ~13%) (Mathew et al., 2014) followed by the 20.1% achieved by recently emerged perovskite sensitized solar cells among molecular absorber solar cells (NERL, 2014). Besides, DSCs have shown their working capability in low light unlike the conventional silicon PV technology that requires 200 – 300 watt/m^2 for its start-up operation and 800–900 watt/m^2 for peak performance (Ubertini and Desideri, 2003). In various comparative analyses DSCs showed higher power output compared to similar power ratting silicon and thin film solar panels. This exclusive feature of DSCs, i.e., their working capability in low light, not only increases their operating hours but also enable to deploy them in shaded regions, corners or bends in buildings.

Besides the advantage of DSCs for applications in low-light and flexible conditions, its deployability would strongly depend on the module manufacturing cost and associated economics. The DSCs provide solar electricity at a cost 2 – 3 times cheaper than first two generation of solar cells as despite their much lower η than the latter (the η of the state-of-the-art DSCs and silicon solar cells is ~13% and ~25%, respectively), which could be attributed to the cheaper material cost and easy fabrication. Furthermore, the photoelectrode materials such as TiO2, ZnO, SnO2, are largely abundant unlike indium which is a successful material in thin film solar cells or silver which is a crucial interconnecting material in silicon solar cells (Nelson J., 2013). Notably, two third of the total cost in DSCs arises from materials (dyes, electrolytes, substrates and sealing material). As suggested by Hashmi et al., (2011) a substantial decrement of this price is possible by replacing some of the expensive material components; i.e., replacing glass substrates with flexible plastic, which is one third of its price, will reduces ~30% of the material cost. Besides plastic, replacing FTO by stainless steel sheets can save up to 80% of the substrate cost.

Owning to their unique features of low cost fabrication, transparency and low light workability large scale development of dye-sensitized solar modules (DSMs) is also seen across the globe. The highest certified efficiency in the DSMs is ~8.2% (~25.5 cm^2) which is significantly lower than their laboratory scale analogues (certified η~11.9% in area ≤0.25 cm^2) (Green, et al., 2014 and L. Han et al., 2009). The DSMs (area ≥5 cm^2) are connected in series or in parallel to provide higher output voltage or photocurrent, respectively. The significant loss in η upon up-scaling the laboratory scale DSCs is surprising and has never been reported in the published reports. We have undertaken this study to investigate the factors behind the loss in photovoltaic parameters and also identify the possible designs with improved performance.

1.2 PROBLEM STATEMENT

Intense research during the past two decades brought the DSCs to a level of delivering efficiency (η) ~13% in single cells using mesoporous TiO_2 particles, organic dyes (porphyrin dyes, for example), and suitable electrolytes. The device offers significant difficulties to scale up; most stringent one is the lowering of photovoltaic parameters while the electrode size is increased. Although the above fact is known qualitatively no systematic efforts are undertaken to quantify the lowering of photovoltaic parameters with device area. A thorough quantification is expected to provide new insights on the scalable simple fabrication of high efficiency DSCs.

On the other hand, DSMs are currently fabricated by interconnecting individual strips of area 5 cm^2 in series, parallel or a combination of both. We note that in such designs the primary contribution to the lower η is the photocurrent (J_{SC}); the routinely obtained J_{SC} in DSMs is ~30 – 50% to that of high efficiency DSCs (Table in appendix II and the references therein). Surprisingly, this loss of photoelectrons in DSMs is never explained in published reports.

In order for DSMs to be a cost-effective commercial device, the photovoltaic performance in their commercial modules is to be improved. An insight of photoelectrode area dependent efficiency is therefore crucial to realize the factors behind the inferior performance of DSMs.

1.3 OBJECTIVES

The objectives of this study are:

1. To investigate the dependence of photovoltaic parameters of DSCs as a function of electrode area using commercial choice of materials.
2. To correlate the photovoltaic parameters of DSCs with charge transport parameters as a function of photoelectrode area.
3. To develop alternative device designs with improved charge collection based on the insights gained from area dependent studies.

1.4 SCOPE OF THE STUDY

The study focuses on fundamental insights of charge transport parameters of DSMs via electrical and electrochemical impedance spectroscopic (EIS) characterizations. At first, range of DSCs of photoelectrode area (0.15 – 2 cm^2) are investigated to explore the area dependant charge collection in them. Such experiments will enable us to find the threshold photoanode area for optimum charge collection. The EIS characterizations besides electrical characterizations will open new insights on area dependant charge transport in DSCs.

The study also explores alternative designs to facilitate greater charge collection in large area photoelectrode (~25 and ~100 cm^2). Current-voltage and transmission line model based electrochemical characterization are used to validate the improved electronic transport and efficient charge collection thereby in such novel photoanode designs. Distinctive experiments are designed to compare the performance of such design with conventionally adopted DSM designs. The experiments will yield the information of the factors behind the inferior performance of DSMs compared with their laboratory scale analogues and also lead to the possibilities for high efficiency DSMs.

1.5 SIGNIFICANCE OF THE STUDY

Although the DSCs are a potential photovoltaic technology, their commercial deployment is primarily hindered due to the inferior performance of the modules. As the objectives of this study aim to provide insights of variation in charge transport parameters while up-scaling the DSCs, our results serves as fundamental science for researchers working in organic photovoltaics and also provide design guidelines for engineers and corporate sector to build high efficiency DSMs.

The study is helpful for designing DSMs in particular, and in general, any organic photovoltaic device where the low diffusion co-efficient of the photoanode material induces higher recombination. The study can be applied to other organic solar cells characterized by a diffusive charge transport and where film thickness is several micrometers. Such studies are crucial as the fundamental science is to be well understood for technological development.

1.6 THESIS ORGANIZATION

The present study is organized as follows: Chapter 1 outlines the research background, problem statement, objectives and also the significance of our study. Chapter 2 explain the working principle of the DSCs, list downs key features of DSCs compared to other classes of solar cells, and analyze the progress made in up-scaling the DSCs from laboratory to a commercial deployable scale. In chapter 3, we explain the various materials, experimental protocols and characterization tools utilized in present study. In chapters 4 – 6, we explicate the findings of our study, “the major factors behind the inferior performance of DSMs and also their alternative designs”. Finally in chapter 7, we conclude our observations and make recommendations for high performance and cost effective DSMs fabrication.

CHAPTER 2

LITERATURE REVIEW

2.1 INTRODUCTION

This chapter reviews the progress made in transforming the DSCs from laboratory scale to a commercially deployable device. At first, the working principle of the DSCs is explained and their outstanding features that put them at the photovoltaic technological forefront are compared with other photovoltaic devices. In next section, the progress made in DSM fabrication is reviewed that detail the fabrication processes involved, and types of interconnection such as series, parallel and a combination of both. Progress in deploying the dye-solar panels is also outlined. The limitations of the adopted DSM designs and the optimization carried out for a complete charge collection in large area photoanodes are critically analysed in the last section of this chapter.

2.2 DYE-SENSITIZED SOLAR CELLS: HOW DO THEY WORK?

Many reports are published on the phenomenology of photovoltaic action in DSCs and choice of various materials used (Bisquert J,, 2008; Grätzel M., 2003; Hagfeldt et al.,2010; Wang Q et al., 2006). The DSC is a photoelectrochemical device in which the current flows between a dye-anchored metal oxide semiconductor and a hole-conducting electrolyte upon light absorption. Figure 2.1 is a schematic showing the various materials and their interfaces constituting the DSCs. A mesoporous film of thickness ~10 – 20 μm of a metal oxide semiconductor (MOS, usually TiO_2) is coated on a conducting glass substrate (working electrode, WE). The film is then conjugated with a molecular absorber (dyes); a junction is made by making the film in contact with an electrolyte and subsequently sealed using a counter electrode (CE). A number of counter electrode materials including noble metals, carbon structures, and compound semiconductors are proposed to catalyze the redox reaction in the electrolyte (Brown T.M. et al., 2014; Wang H., & Hu, 2012; Wang W., & Hu, 2014; Wu M., & Ma, 2014).

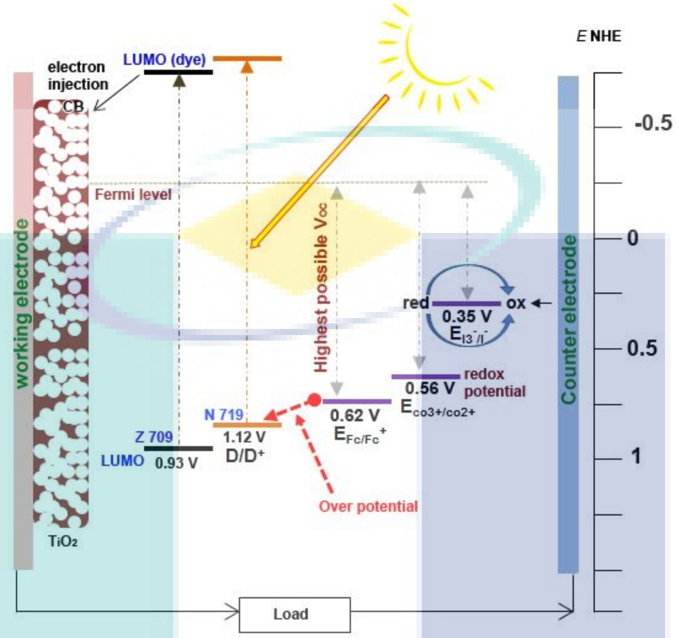

Figure 2.1: Schematics of working mechanism of a DSC. The values are taken from Daeneke et al.,(2011) and Yum et al., (2012).

Source: Figure adopted with permission of ‘The Royal Society of Chemistry’

Upon absorption of sunlight, the dye undergoes a $\pi - \pi^*$ transition and thereby excite an electron from the lowest unoccupied molecular orbital (LUMO) of the dye. This excited electron undergoes a nonradiative transition into the conduction band of the MOS and getting oxidized. The injection of electrons from dye to MOS takes merely picoseconds (Hagfeldt et al., 2010). The oxidized dye (D^+) is reduced by the iodide (I^-) in the redox electrolyte by accepting one electron and forms a complex (D…I). This complex reacts with another iodide and brings the dye to ground state (D) and form I_2 (Boschloo et al., 2009 and Grätzel M., 2003). The oxidation of dye and then its reduction by redox couple can be described by reactions,

$$D^{*} \longrightarrow D^{+} + e^{-}$$
$$D^{+} + I^{-} \longrightarrow (D\ldots I)$$
$$(D\ldots I) + I^{-} \longrightarrow D + I_2^{-}$$
$$2I_2^{-} \longrightarrow I_3^{-} + I^{-}$$

Since the pioneering work of O’Regan and Grätzel (O'Regan, 1991) intensive research on DSC’s material optimization (substrates, MOS, dyes, and electrolytes) is undertaken across the globe (Baxter & Aydil, 2005; Robertson, 2006; Shozo, et al., 2009). Recently, DSCs reached η ~13% (open circuit voltage, V_{OC} ~ 0.91 V, short-circuit current density, J_{SC} ~18.1 mA/cm^2, fill factor, FF ~0.78) in device of area ≤ 0.25 cm^2 (Mathew, et al., 2014).

2.3 Classification of Dye-sensitized solar cells

The DSCs are classified based on the nature of electrodes (n – type or p – type), substrates (rigid or flexible), electrolyte (solid or liquid), and number of active photoanodes (tandem). Most common DSCs are built on fluorine doped tin oxide coated glass substrates (FTO); however, flexible substrates such as conducting plastic and metallic substrates are also employed. Research on all these types of DSCs is undertaken globally such as: (i) redox liquid electrolyte based DSCs which show η up to 13% (Chiba et al., 2006; Liyuan Han et al., 2012; Yella et al., 2011) (ii) solid-state hole conductors based DSCs which replaces the liquid electrolyte by a hole transporting material (HTM) (Bach et al., 1998; Chung, et al., 2012; Wang et al., 2006; Snaith & Schmidt, 2007), (iii) DSCs made on flexible substrates such as low temperature processible conducting plastic (Pichot P, & Gregg, 2000; Weerasinghe et al., 2013), high temperature compatible metallic foils (Ito et al., 2006; Lin et al., 2012), and wire shaped DSCs (Fan et al., 2008; Wu J. et al., 2012), (iv) p-type DSCs where the electron injection takes place from the valance band of a p-type MOS (commonly NiO) to the LUMO of photoexcited dye (Lindström et al., 1999; Odobel et al., 2012; Zhang L. et al., 2011), and (v) tandem designs of DSCs with two photoactive anodes (both n – type and p – type) combined in either series or parallel (Nattestad et al., 2010; Xiong & Chen, 2012). A breakthrough in the third generation solar cells is the emergence of perovskite sensitized solid state solar cells (PSCs) which employ an organic – inorganic hybrid perovskite absorber (commonly $CH_3NH_3PbX_3$, X = Br, Cl, or I) on a very thin MOS layer (< 1μm) (Lee Im., et al; Kim et al., 2013; Park, 2013). Although PSCs initially emerged as a class of DSCs but they are likely to be a new class of solar cells. The η as high as ~20.1% is reported in PSCs which is a four times increment in just four years of its first report (NERL, 2014).

2.4 DSCs Vs. OTHER PHOTOVOLTAIC TECHNOLOGIES

One of the major drawbacks of the conventional silicon PV technology is the amount of solar irradiation required for its start-up operation (200-300 watt/m^2) which increases to 800-900 watt/m^2 for peak performance (Ubertini & Desideri, 2003). Despite the fact that the highest certified η in DSMs (8.2%)(Han L., et al., 2009) are far lower than that is achieved in the first two generation solar cells (~15 – 20%), their working capability in low light conditions and transparency place mark them as a potential photovoltaic. This exclusive feature of DSCs, i.e., their working capability in low light, not only increases their operating hours but also deploys them in shaded regions, corners or bends in buildings. A comparative study by Dyesol Ltd. revealed that DSCs delivers 65–300% higher power output in cloudy days compared to silicon and thin film solar cells as shown in Figures 2.2(a and b). (Dyesol, 2011) Their analysis revealed that the performance of DSCs is higher in days when the solar irradiance is <300kW/m^2. In another six month comparative study by Aisin Seiki CO. Ltd.,(Kalyanasundaram, 2010) DSCs (64 cell modules of size 10× 10 cm^2) showed 10% increased performance in a hot sunny day and 20% higher in a cloudy day than single crystalline Si-modules. The study also showed better performance of DSCs in midmorning and midevening thus widening the available performing hours. A similar performance was demonstrated in Japan in a world solar car rally (July 2008), where a 2×8 m^2 DSMs (developed by Taiyo Yuden Co. Ltd.) were deployed on a test race car and achieved a speed of 11.8 km/h in cloudy weather which was almost similar to 12.5 km/h in sunny weather. These reports spotlight the exclusive features of DSCs and their capability of working in low light conditions that overcome the limitations of the conventional PV technology. Moreover, a recent study by Zardetto et al., (2014) that showed the flexible DSCs when turned into a curve shape outperform a flat device further strengthens the claim on the application diversity of DSCs. Their study showed ~10% higher power output in the flexible DSCs built on a metallic substrate than a flat DSC. All these results are encouraging for DSCs' potential applications at low light areas. As an example, in zero energy buildings the DSCs can be deployed as smart windows to simultaneously add aesthetic while producing solar electricity almost entire day.

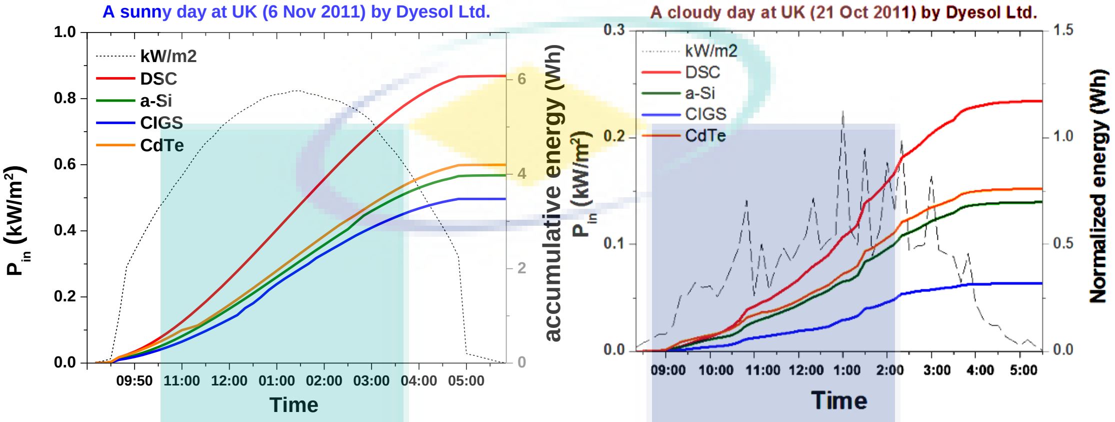

Figure 2.2(a): performance comparison of DSCs' with other photovoltaic technologies on a sunny day, (b) a cloudy day.

Data courtesy to Dr. Damion Milliken of Dyesol Ltd.

Unlike the first two generation solar cells, which require clean room and vacuum based device fabrication facilities, DSCs could be fabricated at ambient conditions. To further ease its fabrication, researchers successfully showed low temperature (<150 °C) binder free coating process in DSCs on plastic substrates and demonstrated η as high as ~8% in their single cells and ~6 % in DSMs (Zardetto et al., 2013).

The performance of DSCs increases at elevated temperatures (from room temperature to ~50 ^{o}C) as the viscosity of the electrolyte decreases upon increase in temperature which meliorates the ionic transport inside the MOS (Hinsch A., 2001; Sommeling et al., 2004). Conversely, silicon based solar cells drops in performance at elevated temperatures as the electrical properties of the semiconductor are dominated by thermally excited photoelectrons (Ray, 2010; Skoplaki & Palyvos, 2009).

2.4.1 Cost-effectiveness of DSCs Vs. Other Photovoltaic Technologies

Besides the advantage of DSCs for applications in low-light and flexible conditions, its deployability would strongly depend on the module manufacturing cost and associated economics. Table 2.1 shows a comparison of manufacturing cost normalized with respect to the peak output power compiled from various sources. The DSCs provide solar electricity at a cost 2 – 3 times cheaper than first two generation of solar cells as (Table 2.1) although their η is much lower than the others, which could be attributed to the cheaper material cost and easy fabrication. Besides, the Photoelectrode MOS such as TiO_2, ZnO, SnO_2, are largely abundant unlike indium which is a successful material in thin film solar cells or silver which is a crucial interconnecting material in silicon solar cells (Nelson J, 2013).

Table 2.1: Cost/W_P and η comparison of various types of solar cells/modules; the values are taken from Green, et al., (2014) and our published review article Fakharuddin A. et al., (2014d) unless stated otherwise.

Device	η in cells (%)	η in modules (%)	Module manufacturing cost/W_p($)
Multijunction (III– V)	44.7 (FhG-ISE)	---	---
Si	24.7 (UNSW)	14.5	~0.8-1*
CIGS	19.8 (NREL)	18.7(FhG-ISE)	1.13
Si (amorphous)	10.1 (AIST)	---	---
CdTe	17.3 (NREL)	11.7	0.74
Organic PVs	10	6.8	0.75-2
Dye solar cells	11.9 (SHARP)	8.2 (SHARP)	0.5-0.94
Perovskite solar cells	15.6 (Oxford PVs)	NA	NA
QDSCs	7	Not developed yet	NA

* Market prices of silicon panels have droped in latest years to as low as ~0.7 $/Wp; however, such prices are from few producers and the realisticity and sustainability of such prices are yet to be determined (http://www.nyse.com). While part of this is due to oversupply in the market, a good portion is also due to advances in technology and economies of scale due to an increase in cumulative worldwide PV production (Fakharuddin et al., 2014d).

Kalowekamo et al., (2009) estimated the manufacturing cost for DSMs and compared it with first two generation solar cells (Table 2.1). The estimated DSM cost varies from 0.5$/$W_P$ (η ~5%) – 1$/$W_P$ (η ~15%). Furthermore, DSMs provided 2-3 times cheaper electricity than silicon solar cells (2.35 $/$W_P$) and thin film solar cells (1.65 $/$W_P$). Although manufacturing cost of DSMs is significantly lower than first two generation solar cells a greater contribution (50 – 60%) to DSMs manufacturing cost arises from their material cost (primarily dyes, electrolyte, and substrates).(Hashmi, et al., 2011) The materials for DSCs are still produced on research scale; the cost would significantly reduce on a commercial scale production. A DSM manufacturer Fujikara Ltd. reported that the manufacturing cost can be reduced to 0.4$/$W_P$ provided an annual production level of 100 MW is achieved (Tanabe N., 2010).

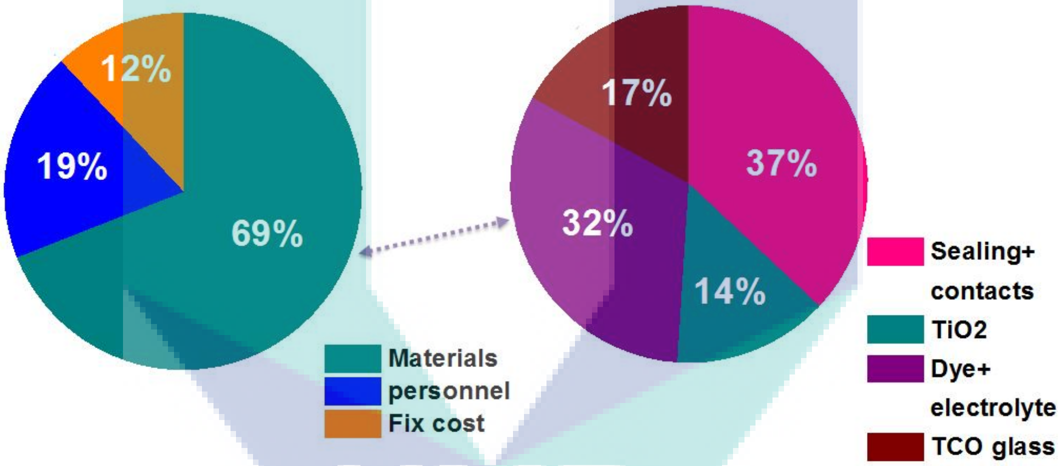

Figure 2.3: Left panel is estimation of the projected share to overall cost during large scale manufacturing and the right panel is cost for various materials while fabricating the 20 MW DSMs (Fakharuddin A. et al., 2014d).

Source: Figure adopted with permission of 'The Royal Society of Chemistry'

Figure 2.3 shows manufacturing cost data for series interconnected DSMs (90 cm × 60 cm, power output 50 W_P/m^2). These statistics are compiled by one of the world leading DSM manufacturers, Solaronix Ltd., for an annual production of ~20 MW_P/year (Toby Meyer, 2009). The DSMs manufacturing cost was estimated to be 0.97 Euro/WP with η ~7% and ~90% process output yield. Notably, two third of the total cost arises from materials where dyes and electrolytes contribute one third (32%), sealing and interconnections cost more than one third (37%) and substrates cost ~17%. As suggested by Hashmi et al (2011), a substantial decrement of this price is possible by replacing some of the expensive material components; i.e., replacing glass substrates with flexible plastic, which is one third of its price, will reduces ~30% of the substrate cost. Besides plastic, replacing FTO by stainless steel sheets can save up to 80% of the substrate cost. Similarly, solid-state device fabrication does not require intensive sealing as in the case of liquid based electrolyte; and therefore, *s*-DSMs would add to significant overall cost reduction.

2.5 EMERGENCE OF DYE-SOLAR MODULES

After the seminal report in 1991 in single cells, the same group reported first DSMs in the year 1996 (Kay & Grätzel, 1996). In their module, six DSCs of area ~3.3 cm^2 were serially connected on FTO substrate to deliver η~5.3%. Since then a number of reports are seen across the globe for the development of various type of DSMs including series, parallel or their combination. A survey of literature shows that efforts in the development of DSMs are rather unimpressive: only one research paper is published for DSMs for each hundred papers on laboratory devices. Figure 2.4(a) shows a summary of research papers and patents published on DSCs and DSMs. A study on the country's involvement in DSMs are also made and shown in Figure 2.4(b). One would observe that China, Japan, Korea, Taiwan and the USA are the leaders in DSM fabrication in the descending order of their contribution.

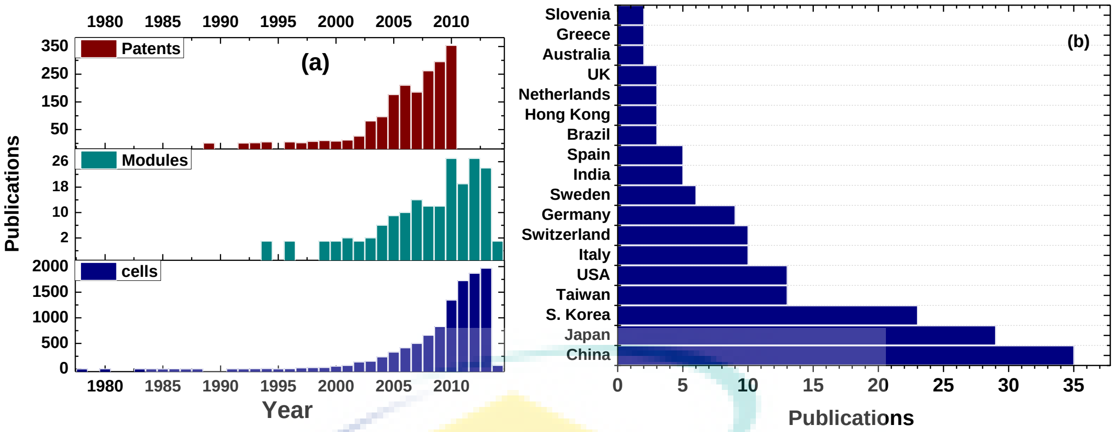

Figure 2.4(a): Research trends in DSCs, (i) bottom panel indicates papers published on single cells, (ii) middle panel represents publications on DSMs, and (iii) patents registered globally (data is taken from Pettersson, et al., (2012), and **(b)** trends shows the affiliation of various countries working on large area development of DSCs. (Data is taken from Scopus on January 2014 using keywords ‘dye-sensitized solar modules’ and ‘large area dye-sensitized solar cells’).

Source: Figure adopted with permission of ‘The Royal Society of Chemistry’

DSMs have now reached a level of deployment as a photovoltaic device. Table 2.2 (appendix I) shows a list of industrial sectors emerged in this photovoltaic device, their core business and key achievements. Owing to the transparency in DSCs, the key venues for installing DSCs are indoor electronic application and BIPVs (Figure 2.5 a – d) (Maçaira et al., 2013) as the DSCs work well in diffused or low light and are less effected by the angle of light incidence. Moreover, BIPVs are preferred on centralized solar power generation as the electricity generated is consumed at the same place thereby avoiding the transmission line losses and infrastructure cost. The DSMs of an active area ~200m^2 are installed at windows of a green building on April 2014 at École Polytechnique Fédérale De Lausanne (EFPL) campus, Switzerland (Figure 2.6 a & b) (Solaronix, 2013). These panels are estimated to be able to generate ~2000 kWh of annual solar electricity. These transparent panels are in five different colors (the unique features of DSCs) and are developed by Solaronix. This massive production is an important milestone for the commercial deployment of DSCs although a number of issues including lifetime of these panels under operating conditions are yet to be addressed.

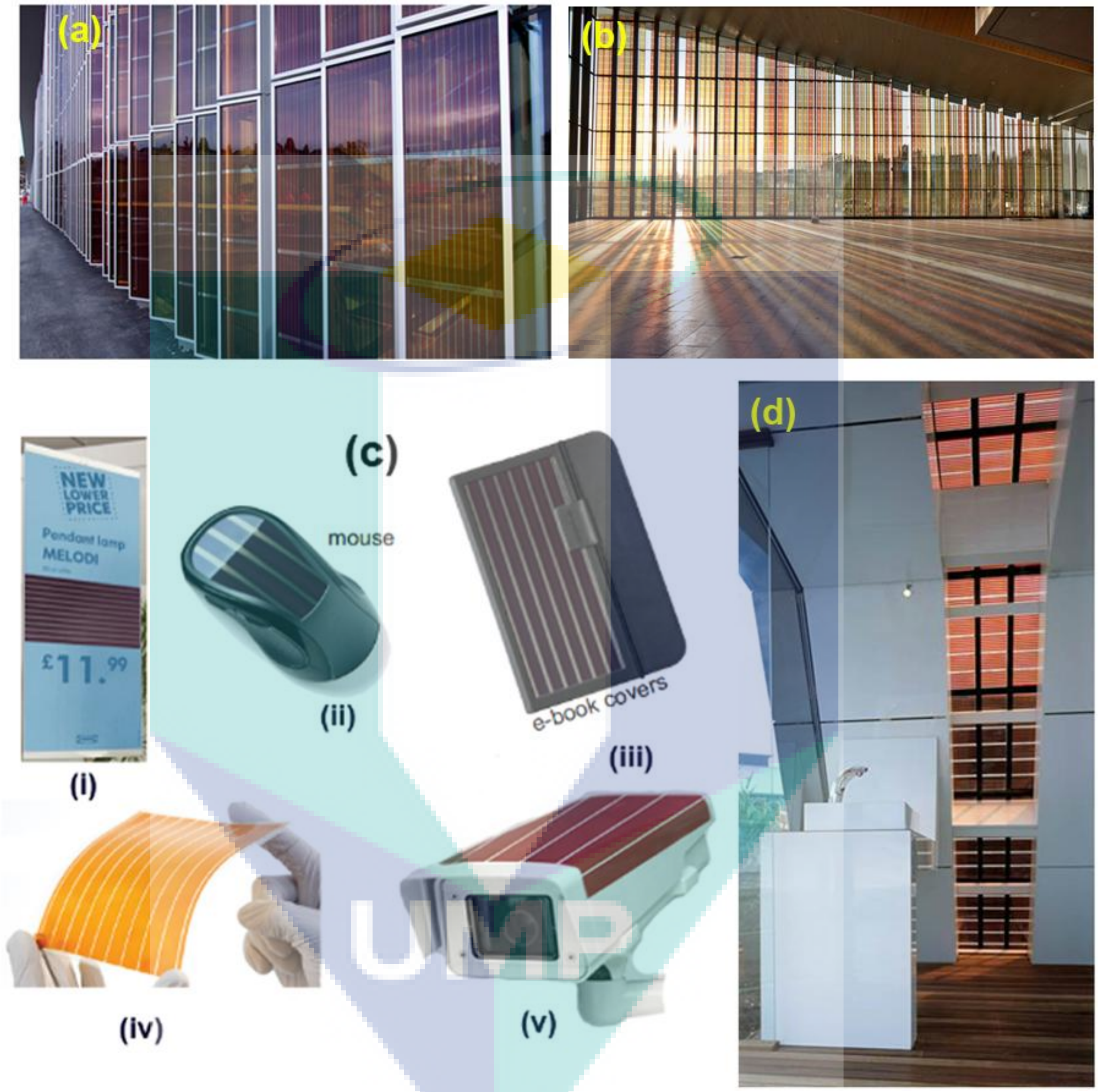

Figure 2.5: (a & b) DSMs installation recently completed at EFPL campus (Photos are courtesy of David Martineau of Solaronix Ltd.), and **(c)** images of few commercial DSC products in market (i—iii are indoor electronics by G24i and iv and v are developed by 3G Solar., and **(d)** DSMs installed as an interior of a washroom by Dyesol Ltd. Image courtesy: Dr. Damion Milliken of Dyesol Ltd.

Source: (Fakharuddin A. et. Al., 2014d)

Dyesol, another leading industrial manufacturer of DSCs, has recently launched projects on integration of DSCs into buildings with their various industrial partners (Tata Steel Europe of UK, Pilkington North America of USA, Timo Technologies of South Korea), and on DSC powered Combined Energy Generation and Storage (CEGS) devices (Dyesol, 2013a). These projects are expected to further reduce the cost/kWh as double coated glass windows in the buildings, meant for UV protection and antireflective coatings, are used as substrates for DSMs. Oxford Photovoltaics, a spin-off company of Oxford University, is working on all solid state perovskite based modules (Table 2.1, Appendix I). The solid state PSMs would significantly improve the lifespan compared to the liquid electrolytes based devices however results on PSMs are to be seen yet.

2.6 CURRENT RESEARCH ON DSMs

Several major advancements are made to upscale DSMs in term of their various interconnection designs, material components, scalable fabrication processes, outdoor stability testing, tandem cells/modules to absorb wider light over solar spectrum, and innovative application such as a hybrid energy harvesting and storage device. These advancements are paving towards the ultimate goal of the technology; their successful commercial deployment as a fossil fuel alternative and compete cost effectively with the incumbent photovoltaics. Such developments include scalable production of DSMs such as fabrication of modules up to 8.2% certified efficiency,(Han L., et al., 2009) emergence of *s*-DSCs and *s*-DSMs owing to their anticipated enhanced lifetime (Crossland et al., 2013; Matteocci et al., 2014), initiation of flexible DSMs and their low temperature processing,(Zardetto, et al., 2013; Zardetto, et al., 2014; Brown T.M et al, 2014)) long term stability and thermal testing of transparent conducting oxide (TCO) based DSCs up to 80^{o}C (Kato et al., 2009), and their application as smart windows (Agarkar et al., 2012). The recent achievements such as the first commercial large scale delivery of DSMs from Solaronix, high efficiency *s*-DSMs from Dyesol (announced η~11.3% at 1 sun, results are to be published yet) (Dyesol, 2013b) and the thermal stability testing up to 90 ^{o}C further orient the successful commercial production of DSMs (Jiang et al., 2013). Figure 2.6 shows a timeline of DSMs development since the first report in 1996 till 2014. It highlights the major achievements of DSMs and also projects their potential future. In this section, we briefly review various developments in DSMs fabrications techniques and various designs.

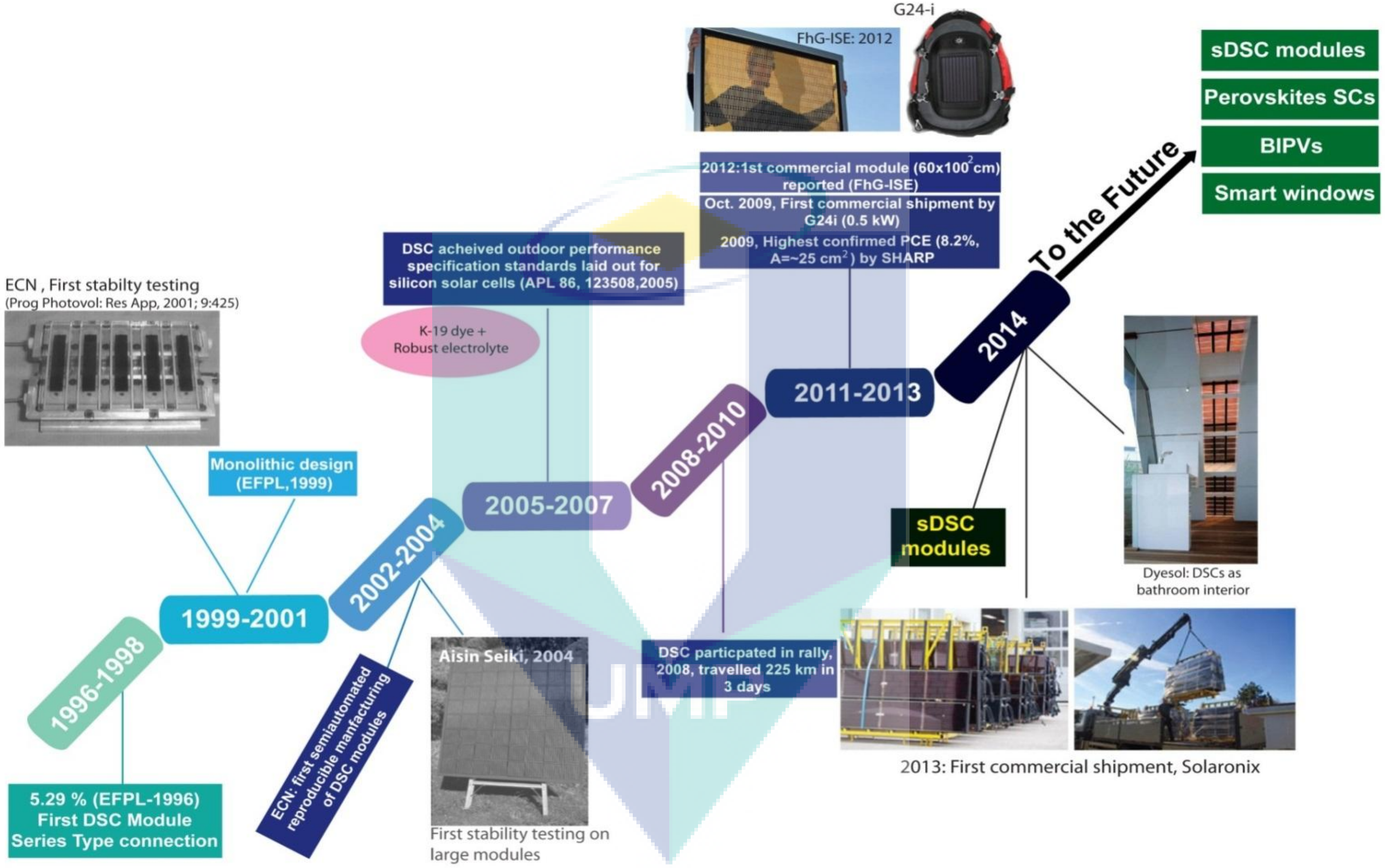

Figure 2.6: Step-by-step historical evaluation of dye-sensitized solar modules (Fakharuddin et al., 2014d).

2.6.1 Fabrication process on DSMs

The fabrication of DSMs differs from that of single cells primarily due to the electrical connections among neighboring cells. Screen printing is usually employed as a coating method for photoanodes of DSMs (Pettersson et al., 2007) as it is compatible with roll-to-roll processing. Screen printing technology is a commercially available method for printing arts and can be used for printing on both glass and plastic substrates. Figure 2.7 shows a block diagram of various processes involved in DSMs fabrication. For details of each section, we refer to the pioneering work by Spath et al., (2003) and a recent review by Hashmi et al., (2011). In brief, the working and pre-drilled counter electrodes are cleaned using trichloroethylene, acetone and ethanol. The electrodes are then etched for series connections. CEs are platinized by depositing Pt precursor pastes and then cured in a furnace.TiO_2 layers are coated on the working electrode (WE) via screen printing to get a desired photoanode thickness (~10 µm). A heat treatment (100 ^{o}C) after each coating cycle is helpful to obtain stability of each layer. In a batch process, the coated FTOs are heated on a belt furnace to remove organic binders in the paste and to sinter TiO_2 nanoparticles together. Interconnections (series) or current collecting fingers (parallel) between neighboring cells are made using conducting media (such as silver). The WEs are sensitized with a dye and device is completed by placing the patterned CEs on the WEs with 30-60 µm thick spacer between them and sealed. The Ag fingers are encapsulated to avoid their contact with the liquid electrolyte. Electrolyte is filled through drilled holes and after filling, the holes are sealed via cover slips and sealant material.

The typical dye-sensitization methods are not suitable for DSM batch production as it require longer soaking hours. Accelerated dye-sensitization process are thereby introduced which require few minutes for dye-anchoring and yield similar photovoltaic performance to that of typical overnight soaking. Such accelerated methods may reduce the batch production time significantly. Energy Center of Netherlands (ECN) researchers introduced a novel dye-anchoring method where they pumped the dye solution in a pre-sealed DSM through two drilled holes. Such method is beneficial when the device is to be sealed using glass frit that requires high temperature (~500 ^{o}C) for adhesion; at which temperatures the dye decomposes. During DSMs fabrication, encapsulation and electrolyte filling are amongst crucial steps. Good encapsulation is crucial for long lifetimes as improper filling would lead to significant performance degradation for similar type of devices. At present, many of the researchers use pre-drilled holes at CE to inject the electrolyte via vacuum back filling. This process is however tedious and a number of automated units for electrolyte filling are now offered by various companies such as Dyesol Ltd. easing the continuous production of DSMs.

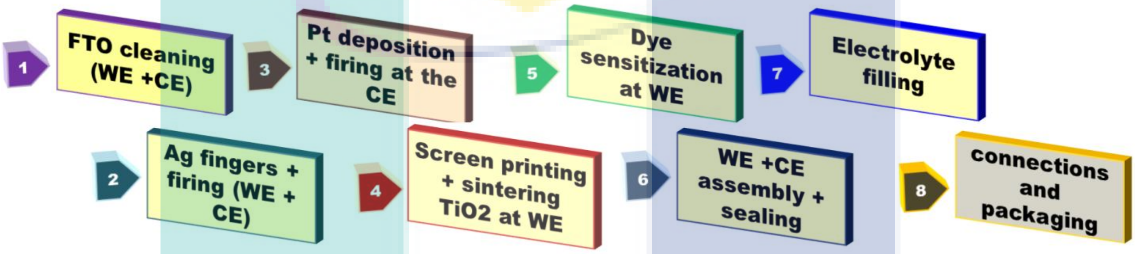

Figure 2.7: A schematic of a parallel DSMs assembly line. The figure is adopted from Fakharuddin et al, (2014d) and the references therein which outlines the steps for parallel modules. For series connected modules the FTO has to be scribed for cell isolation. The W-type modules require no Ag interconnections and for the Z architecture the order of the steps can change.

2.6.2 Designs of DSMs

After intensive research for nearly two decades, commercial DSMs developments are underway (Table 2.2, Appendix I). The fabrication of DSMs is different from a laboratory scale device due to (i) large scale metal oxide coating on TCOs, (ii) extensively impermeable sealing to humidity, air and to prevent liquid electrolyte from drying and leaking, (iii) electrolyte filling, (iv) interconnection for modules (series or parallel) and external electrical connections, and (v) the most important is the anticipated lifetime of the device compared to that offered by silicon based devices (~20 years). Electrical connections need intensive care during fabrication process as an ineffective contact will ultimately lower FF by adding to the series resistance and eventually dropping the η (Giordano et al., 2011; Mastroianni et al., 2012). Two major types of connections are employed for DSMs fabrications, (i) parallel designs which provide high photocurrent and (ii) series designs for high output voltage include Z-type, W-type, and monolithic connections. These designs employ large rectangular strips (area $\geq 3cm^2$) interconnected serially or in parallel as shown in Figure 2.8(a-e). In this section, we highlight the differences in these various interconnections, their advantages and disadvantages and also critically analyze their photovoltaic performance. For convenience, we define three common terms (active area, aperture area, and total area) that will be intensively used in this section. Active area is the area covered by TiO_2 strips only on a substrate; aperture area is the sum of active area and the distance between them; and total area is the total substrate area which also includes the area used for interconnections and blank spaces on the substrate.

Series interconnections: Monolithic design (S-type)

The term monolithic here refers to deposition of electrode material layers sequentially by printing and pressing them successively. The monolithic DSMs are attractive as they are made on a single substrate (Figure 2.9a) and eliminate the need for the CE. Owing to their single substrate architecture, monolithic designs are highly compatible with roll-to-roll processing of flexible DSMs as they do not require continuous photoanode thickness (Wang et al., 2010). These designs also replace expensive platinum by cheaper carbon black as CE; therefore, 20–30% of material cost reduction is estimated in monolithic type of series modules designs compared to the other designs.

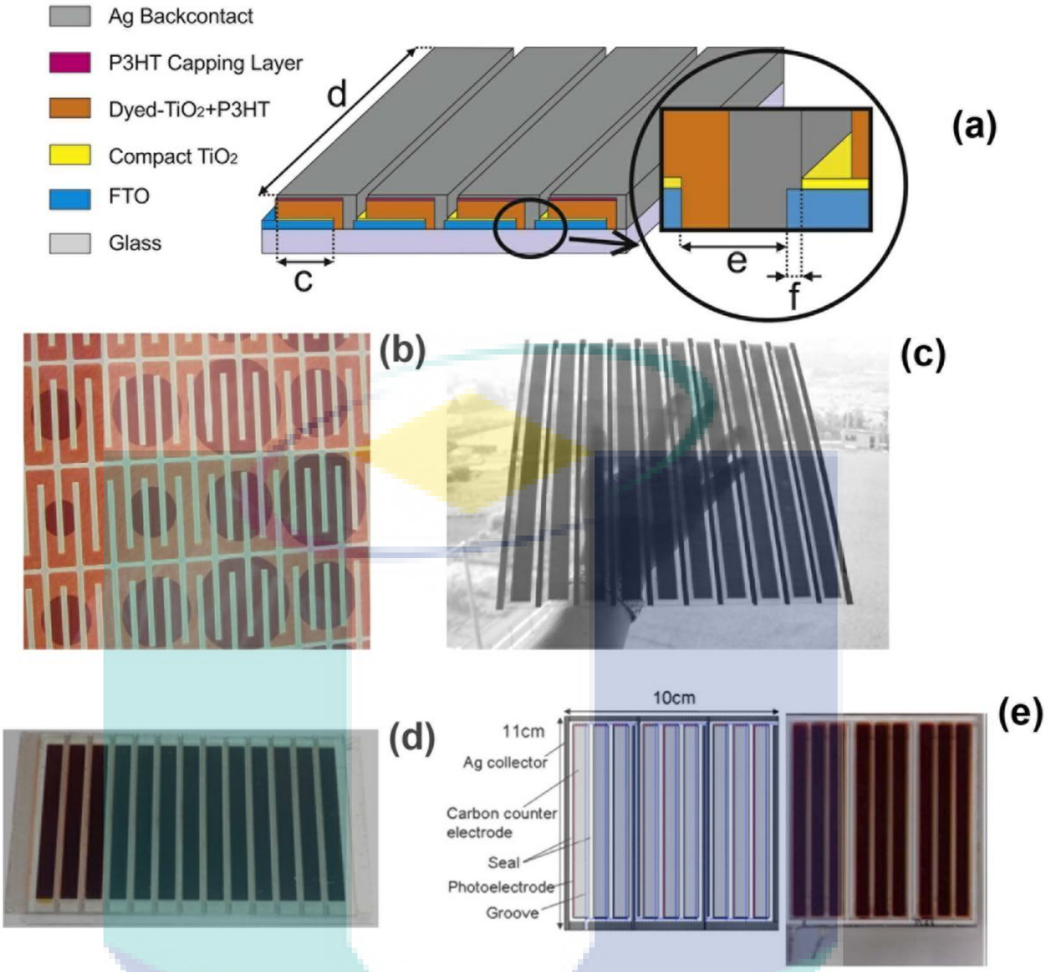

Figure 2.8: Adopted designs of conventional DSMs. (a) design schematics of sDSM, (b) DSMs design for façade application under a Euorpean project COMSOL, (c) a flexible plastic DSMs, (d) a series Z-type module, and (e) a parallel grid type design where the individual strips are surrounded by a metallic curent collecter.

Adopted from Fakharuddin et al., (2014d)

Monolithic design is also called Kay cell, named after the inventor Andreas Kay, who reported the first DSM in 1996 with η ~5.3% (Kay & Grätzel, 1996). The notable achievements in their report are (i) replacement of expensive platinum with porous carbon as CE, (ii) a porous insulating layer between WE and CE to avoid short circuit but letting the electrolyte diffuse through its pores freely, and (iii) a continuous, conveyerized fabrication process of series connected DSMs. Thickness of the photoanode in Kay cell was ~80 µm (TiO_2 10 µm, Rutile spacer 10 µm, & carbon black 60 µm). The DSMs (six strips of 4.7 × 0.7 cm^2 and total area ~21 cm^2) yielded η ~5.3% (V_{OC}~3.90 V, I_{SC}~28.55 mA, & FF ~0.61). Major drawbacks of this design are much lower J_{SC} (1.3 mA/cm^2) despite a high output voltage ~4 V, high opacity, and poor sealing of the device. ZrO_2 is also employed to replace opaque rutile spacer; however, the transparency was lower than that of a conventional Pt electrode (Wang L., et al., 2010).

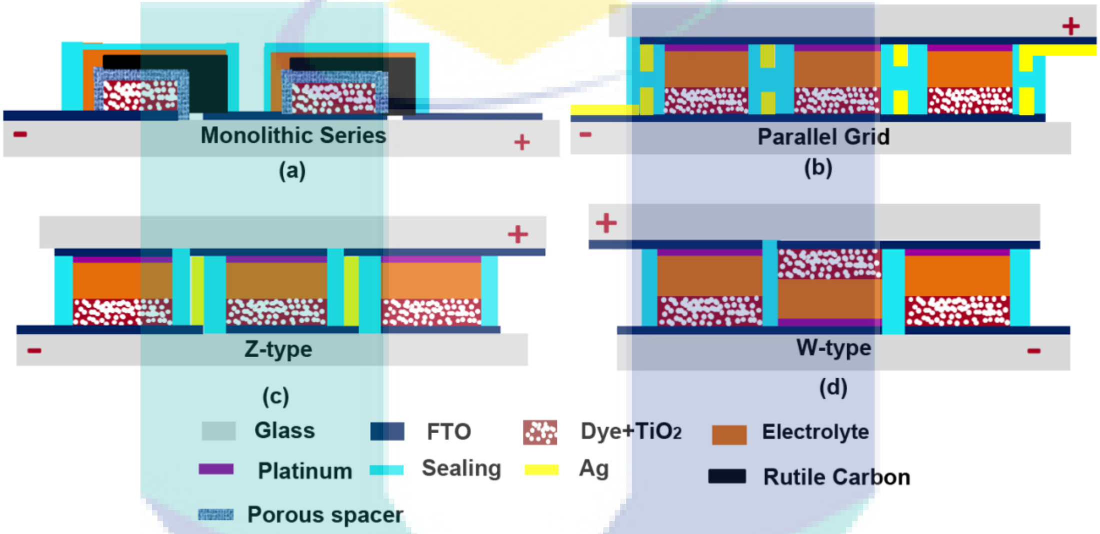

Figure 2.9: Schematic of series type of connections (a) monolithic, (b) Parallel grid (c) Z-type and (d) W-type.

Adopted from Fakharuddin et al., (2014d)

Since the first report on series interconnections, there has been no significant progress in these designs. Thirteen years after the work of Kay in 1996, improved transparency of the monolithic designs was reported by AISIN SEIKI (Takeda et al., 2009). They replaced (i) the opaque counter CE material (carbon black) by a highly transparent paste comprising In_2O_3:Sn and Pt nanoparticles and (ii) opaque rutile spacer by SiO_2 (refractive index 1.5, close to that of electrolyte used) thereby improving the transparency considerably. However, their devices utilized a glass substrate as CE which increased the cost of the device as the first monolithic DSM is built on a single subtrate (WE only) and therefore known as a cost effective design. Furthermore, the photovoltic performance of their module was rather inferior than the first report; the four times larger modules developed by AISIN SEIKI (95 mm × 95mm, area ~91 cm^2) resulted in 30% decreased J_{SC}(~1.7 mA/cm^2) compared to the Kay's first design (area ~21 cm^2). The lower J_{SC} limited the η to be <3% despite a higher output voltage (~8 V).

One of the major advantages of this design is the high active to total area ratio. In both reports on monolithic designs, this ratio was >90%. However, these connections result in lower J_{SC} due to high series resistance and low FF (≤ 0.6) thereby (Jun et al., 2008; Takeda, et al., 2009). As the individual strips are connected in series, immense attention is to be given to match the J_{SC} in all individual cells. Due to series type of connection, the final J_{SC} will be the lowest one in the serially conencted cells. Monolithic transparent DSMs on a single substrate with high transprency are yet to be seen.

Z-type and W-type interconnections

Both these types are series connected devices: one of them uses a metallic conductor to connect the neighbouring cells (Z – type) whereas the other (W – type) does not use it (Figure 2.9 c& d). The names 'Z-type' and 'W-type' stems from their resemblance to 'Z' and 'W' alphabets, respectively. The Z-type connection, also called Z-contact, is adopted from thin film solar cells (Wang L., et al., 2010). In this design the individual cells are serially interconnected via a conducting medium (usually silver) in a way that the CE of the first cell is connected to the WE of neghbouring cell and vice versa as shown in Figure 2.9c.

The first Z-type DSM was demonstrated in 2004 by Toyoda et al., (2004) who connected 64 DSMs (10×10 cm^2) in series to form a large panel. The researchers carried out the first long term stability testing of DSMs for six months and compared their performance with a crystalline silicon module of similar output power rating. Although photovoltaic parameters of DSMs are not exlusively reported the DSMs showed 10 – 20% larger power output for a period of six months. The major issue reported during fabrication is the hermetic sealing of the DSMs which resulted in performance degradation. This issue is resolved in a subsequent report by Sastrawan et al.,(2006) who introduced a highly stable glass frit as a sealent. As the frit is to processed at high temperature (>500 ^{o}C), at which temperatures the dye decomposes, a novel pumping method for dye anchoring was employed. The dye was pumped via two holes after the sealing of DSMs of total area upto 30 × 30 cm^2. The DSMs resulted in η ~3.5% (V_{OC}~20V, I_{SC} ~168 mA, & FF ~0.53) with an active area ~680 cm^2 (74% of total area). The major drawbacks of these reports are the low FF (<0.55) and low J_{SC} (<0.5 mA/cm^2) arising from the high series resistance of photoelectrodes. Jun *et al.*[135] reported a DSM (10 ×10 cm^2) resulted in sigificantly superior performance, i.e., η~6.6% (V_{OC} ~8V, J_{SC} ~1.23 mA/cm^2, & FF ~0.67). The significant enhancement in FF and J_{SC} is achieved by restriciting the width of each individual strip (<1 cm). A similar advancement is reported by Giordano et al., (2013) by optimizing the geometry of the photoelectrode and using a back reflector to achieve η up to ~7% in modules of ~45 cm^2 area.

Despite the high acheiveable voltage by Z-type DSMs, it suffers from low active area, lower η mainly arising from complexity of fabrication and high series resistance offered by added interconnections. Furthermore, the silver interconnects corrods easily in the presence of liquid electrolytes. In an innovative design by Dyesol, the silver is repalced by less corrosive material (titanium particle of size 45 µm and tungsten particles of size 5 µm in a polymer matrix) (Hopkins et al., 2006). Besides adding stability to the device, this innovative design also eliminated additional interconnection required by the Z-type.

The W-type design offers comparitivly higher active area than Z-type as it avoids additional metallic interconnections. Unlike the Z-type, the neighbouring cells of alternative bias are interconnected in W-type as shown in Figure 2.9 (d). Their simpler design and no additional serial interconnections result in higher FF in the devices. The working of W-type DSMs are different from Z-type as there are two types of configurations, i.e., front illuminated (TiO_2 side, also called F-side) and back illuminated (Pt side, also called R-side). The issue with W-type designs is the difficulty to match the J_{SC} in these two different types. The J_{SC} decreases in the R-side due to light absorption by iodide/triiodide and low transmittance of platinum (Han L., et al., 2009). Thus many optimization procedures to match the J_{SC} of both types add complexity to fabrication. Yet, SHARP Co. reported the highet confirmed η in W-type interconnected DSMs (8.2% and 9.3% with respect to active and total area, respectively) (Han L., et al., 2009). The active area (25.45 cm^2) was 85% of the total area.

One crucial requirement for both Z- and W-type designs is the seperation required between neighbouring cells to avoid mass transfer of electrolyte(Wang L., et al., 2010). As the redox potential of the electrolyte changes when illuminated, a possible ion exchange between adjacent cells would separate the redox couple. This process is called photophoresis and is responsible for performance deterioration over time in DSMs. Thus an individual cell has to be a complately isolated compartment.

Parallel interconnections

Despite high V_{OC} by series interconnected DSMs, the required precision to match the J_{SC} of individual cells and intensive care to interconnect the neighbouring cells to avoid lower FF make their fabrication very complex. On the other hand, parallel grid type DSMs offer ease of fabrication as they avoid interconnection of working and counter electrodes (Figure 2.9 b). An example of such connections is the ‘masterplate’ designed by a joint research of various European institutions under the programme Nanomax (Kroon J.M., 2005). In parallel connections, charge is collected not only from the bottom of the electrode in contact with the FTO but from the sides of the strips also by using a metal grids (Ag, Ni, Cu Al, and Au) (Dai et al., 2004; Kroon J. M. et al., 2007; Wei T.C. et al., 2012). These metals grids significantly enhance the photovoltaic performance of DSMs; 100% increments in J_{SC}, >200% increment in FF and 5 folds enhancement in η is reported when silver grids are coated alongside large strips (Ramasamy et al., 2007). Spath et al., (2003) reported a reproducible manufacturing of parallel connected DSMs (27 DSMs with total area ~100 cm^2) with η ~4.3±0.07%. This method is further developed to deliver η ~7.4% employing silver as current collecting grids (Takashima et al., 2008).

These designs routinely result in high FF but the major drawback is the low active area due to silver current collectors. This lowering is due to corrosion of silver grids by the iodide/triiodide electrolyte which has to be avoided using thick spacers (Surlyn or Bynel).

Ball grid connections

Ball grid connection (based on ball grid array connection in electronic circuits) was introduced by NGK Spark Plug Co., Ltd., Japan to overcome lower FF when the electrode width is increased beyond a critical size (Takashima, et al., 2008). This critical width is determined to be ~0. 5 – 1cm^2 such that the ohmic resistance of the film is reduced and offers higher FF (Zhang Y. D. et al., 2011). The ball grid design (Figure 2.10 b&c) resembles to monolithic designs as it employs only one substrate (FTO). These modules are connected in parallel and employ vertical metallic balls as current collectors; the major difference is that the electrons and holes are collected at the same side unlike all other designs where electrons are collected from the FTO (Figure 2.10c). The vertically oriented balls are then connected to a flexible hybrid copper polyimide substrate and are taken to the external circuit. Surprisingly, the DSMs of 8 × 8 cm^2 area resulted in similar performance to that of a single cell (area ~0.5 cm^2); the DSMs showed η ~7 – 8% (J_{SC}~16 mA/cm^2, V_{OC} ~760 mV, FF ~0.65) with V_{OC} higher than that of a single cell. The remarkable performance of ball grid place them at commercial upfront due to their ability to retain the performance of a single cell during scale up process and also due to their cost effectiveness as they eliminate the expensive and Pt coated CE. These designs do not require additional interconnectionsand external electrical connection; and therefore, result in very high active area (95%) as shown in Figure 2.10b.

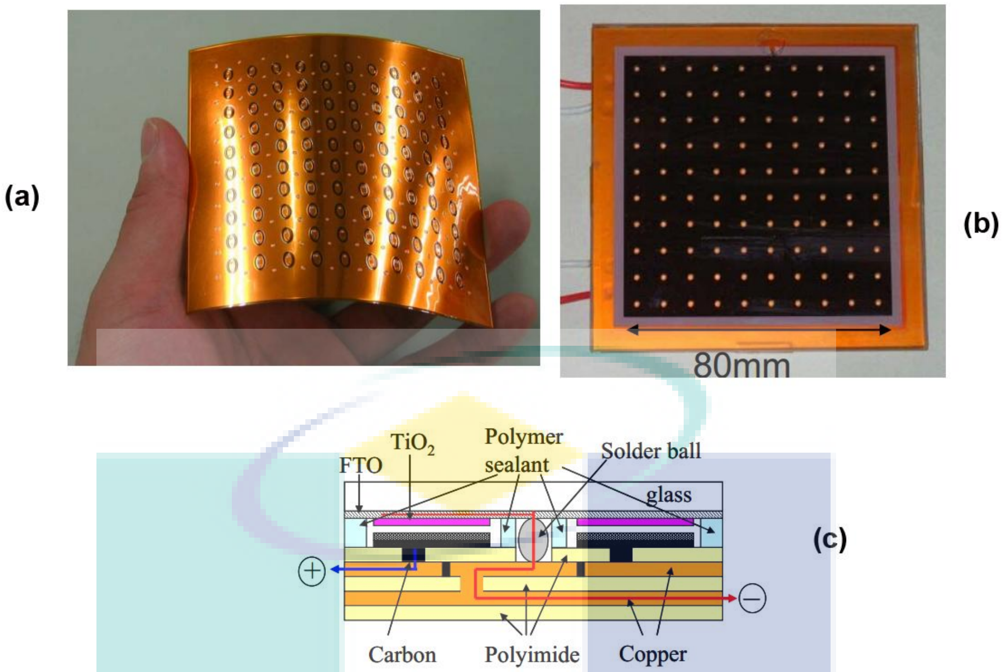

Figure 2.10: (a) Solder shape ball connects on flexible copper polymide substrate, (b) an 80 mm square sub-module with η 7-8%, and (c) cross-section of a ball grid DSM.

Figures are taken from an online report from NGK Spark Plug (2008).

Combined Series and Parallel connected DSMs

Until now we have discussed various series or parallel connected DSMs which provide either added photovoltage or photocurrent, respectively. In such designs, one of the two parameters is compromised; the DSMs with high V_{OC} result in very low J_{SC} and vice versa (Table 2.3: Appendix II). To increase both of these parameters in a single device, a combination of series and parallel connection is also attempted by researchers (Liu et al., 2010; Wei T. C. et al., 2012). Such dually interconnected best performing device so far resulted in η ~6% (V_{OC}~1.4 V, I_{SC} ~287 mA, FF ~0.56) in a device of area ~90 cm^2. The issue here is very low active area as ~50% of the total area is utilized for additional interconnections. Nevertheless, such designs are desired, especially, while designing large area panels as discussed in next section.

2.6.3 Dye solar panels (DSPs)

For realistic commercial applications DSMs, they have to be transformed into larger panelsfor installation. The primary difference in DSMs and DSPs is their size, even though there is no clear description of size limit. In our study, we define a panel when photoelectrode size ≥1000 cm^2.

Numerous industrial developments can be seen across the globe for the DSPs (Table 2.2: Appendix I); however, only few experimental results are published on their performance. The first panel was reported in 2008 with a total area >2m^2, the invidual modules were of area ~300 cm^2 each (Dai et al., 2008). The dually interconnected panel resulted in η ~6% (V_{OC} ~9V, I_{SC} ~2.1 A, FF ~0.62) at 0.87 sun. This η is the highest reported for DSPs so far. Subsequently a joint Euorpean project termed 'ColorSol' was established to develop DSPs for BIPV applications (Hinsch A. et al., 2009). DSPs of area upto ~14000 cm^2 (serially connected individual modules of area ~900 cm^2) resulted in η ~3.6% (V_{OC} ~4.55 V, I_{SC} ~945 mA, FF ~0.56) with respect to total area under 1 sun conditions (η = 4.6% with respect to its active area) was developed under this program. These panels employed glass frit as sealing material; and therefore, reported high stability (~500 h). Both these panels were manufactured by serially inerconnecting individual DSMs; and therefore, the main issue in upscaling the DSC technology, i.e., development of an automated process for large scale panel, still remains a challenge. A research by Hinch A. et al., (2012) reported a semi-automatic process for the fabrication of DSPs up to ~1 m^2, which is an industrially viable size. Although the performance of these panels were comparitivly low (η<3%) than previous reports this is the first report on development of a semi-automatic reproducible process.

2.6.4 Summary of DSMs research: Table 2.3: Appendix II

All these designs have relative merits and drawbacks. Monolithic series are good in terms of continuous industrial mass production and are cost effective however they compromise on performance because of pore filling issues. Similarly, parallel (Ag grid encapsulated) designs are being developed by companies such as 3G solar but they lead to problem of electrical mismatch inside the device as higher currents often results voltage drops. W-type connection type is the simplest to fabricate; however, difficulty in current matching between front and back side illuminated cells limits their efficiency. Z-type delivers good performance, although their manufacturing is more complex due to the vertical interconnections and their encapsulation.

2.7 LIMITATIONS OF PRESENT DSMs

2.7.1 DSMs with optimized photoelectrode dimensions and improved FF

As described in Table 2.3 (Appendix II), various designs of DSMs, solid state DSMs (*s*-DSMs), flexible DSMs (*f*-DSMs) and DSPs are fabricated to bring the device from laboratory scale to a level compatible with industrial mass production. These various types of connections resulted in devices with a voltage as high as ~20 V and a current as high as ~2.5 A in separate devices. However, since the first report on large area DSCs till date, lower J_{SC} is routinely observed in DSMs as compared to their single cells (Table 2.3: Appendix II). The highest confirmed J_{SC} in any DSM is ~18 mA/cm^2 reported by L. Han et al. (2009) in W-type designs but the routinely achieved J_{SC} is much lower than it. The highest J_{SC} in any other design is ~15 mA/cm^2 (in parallel designs), and it is further lowered in series type of connections, i.e., ~10 – 12 mA/cm^2. On contrary, the highest J_{SC} in a laboratory scale single cells is ~27 mA/cm^2 (Kinoshita et al., 2013) and J_{SC}> 20 mA/cm^2 is commonly obtained in high efficiency devices as shown in Table 2.3 (Appendix II).

This loss of 30 – 50% of generated photoelectrons in large area devices is crucial and seldom explained in the published reports. A few reports published on DSMs suggest that the comparatively lower performance in DSMs is due to increased series resistance (R_S) which also affect the FF of these devices. This increased R_S is originated from two sources (i) the width of the TiO_2 photoanode and (ii) the added metallic interconnections particularly in series type DSMs. The realization that TiO_2 width contributes to the R_S was first experimentally demonstrated in 2006 by Biancardo et al. (2006). The researchers varied the TiO_2 strip thickness from 2 – 0.5 cm and suggested that the lower thickness results in superior performance of DSMs; however, a clear trend between FF and R_S could not be drawn from their experimental results. In a subsequent report, Jun et al., (2007) demonstrated the effect of photoelectrode dimensions (length and width of TiO_2) and their effect on FF. They first optimized the TiO_2 strip width (W_S) to be 0.8 cm for optimum FF (~0.65 – 0.62) by varying it from ~0.25 to ~3 cm. The FF dropped drastically from 0.65 to 0.3 when W_S increased from 0.8 cm to 3 cm. On the other hand, when the length (L) is varied from 5 – 15 cm by keeping the W_S ~0.8 cm, the FF showed no dependence on L. Similar dimensions are recommended by Zhang et al. (2011) using simulation and by Giordano et al., (2013) through experiments aimed to design guidelines for DSMs geometric parameters. The latter suggested W_S to be kept between 0.5 – 0.7 cm for photoelectrode length up to 15 cm as it provides a best compromise between aperture area and resistive loss. In another report, Giordano et al. (2013) via modelling of geometric dimension showed a systematic decrease in FF is upon increasing the W_S from 0.5 – 2 cm. No effect is found on V_{OC} or J_{SC} of the devices upon varying the L. They correlated the R_{TCO} with photoelectrode dimensions (W_S, L, and electrode thickness, ‘d’) as

$$R_{TCO} = R_{SHEET} \times \left(\frac{W_S+d}{L}\right) \tag{2.1}$$

Nevertheless, the optimization suggested in all these reports merely involves minimizing the W_S to reduce the R_S offered by substrate. An increase in W_S is suggested as the primary source of elevation in R_S and thereby a drop in FF in all the above reports. It is also proposed that the R_S is not affected by the L, especially in parallel grid connections where the strip is encapsulated by a metallic grid for current collection. However, even after minimizing the width of the individual strips to <1 cm, the performance of DSMs is only < 50 – 60% of that of DSCs at 1 sun. The suggested optimization in these designs although improved FF of the DSMs, added number of interconnections reduced the active area of the modules. In some of these reports, the contribution of R_S to FF is poorly established; for example, in the work of Biancardo et al., (2006) no dependence of R_S to FF is found. In their experiments on DSMs up to 2.5

cm^2, a device with R_S ~3 times higher than the other still exhibited improved FF (device 1: R_S ~46 Ω & FF ~29%; device 2: R_S ~120 Ω & FF ~33%). In another set of devices of area ~625 cm^2, nearly 100% increase in R_S showed 26% increase in FF (device 1: R_S ~188 Ω & FF ~35%; device 2: R_S ~354 Ω & FF ~44%). Surprisingly, none of the reports suggesting optimization of device geometry discussed the reasons behind the low J_{SC} in DSMs. Another important shortfall of all these reports is that a comparative charge transport analysis of large area photoelectrodes with that of a single cell were never provided; and therefore, a detailed understanding of charge dynamic is missing in DSMs.

2.7.2 Ignored diffusive volume in DSMs

We note that all the adopted designs in DSMs are similar. In a common practice, these modules are made in the form of large rectangular strips (Figure 2.11 a–c) of an area ≥3 cm^2 interconnected in either series, parallel or both. Many of these designs are adopted from other PV technologies; the parallel or grid connections are adopted from amorphous silicon solar cells while the series interconnections are taken from thin film modules. These designs do not fit well for DSMs due to their diffusive charge transport which is largely different from the first two generation solar cells (Fakharuddin A. et al., 2013a; Fakharuddin A. et al., 2013b; Fakharuddin A. et al., 2014a; Fakharuddin A. et al., 2014b; Fakharuddin A. et al., 2014c). We noticed that due to negligence of charge transport parameters while up scaling the DSCs, current collection is only from a limited region of photoelectrode. For example, at similar experimental conditions, ECN researchers obtained η ~12 % in their single cells and η ~4-5% in modules of ~225 cm^2 in a master plate design (Kroon J.M., 2005). Such trends are routinely seen in DSMs(Table 2.3: Appendix II); their J_{SC} values are significantly smaller than that in high efficiency DSCs.

Important to note that the charge transport in DSCs is via hopping through n-MOS which is several orders slower than single crystalline semiconductors solar cells (Bisquert J. 2007a; Nelson, 1999). Due to diffusive charge transport and in a competitive situation where the generated electrons are fast intercepted by the ions in electrolyte, the photoelectrode thickness is limited below ~15 µm in single cells (are ≤ 0.2 cm^2). The only defined parameter in DSCs for a complete charge collection is diffusion length ($L_n = (D_n.\tau_n)^{1/2}$) (Jennings J. R. & Peter, 2007; Navas et al., 2011), where D_n is the electron diffusion coefficient and τ_n is the electron lifetime. i.e., the thickness above which electrons recombine with holes in the electrolyte. We noticed that the number of paths and path lengths of electron diffusion increases during scaling up; and therefore, the L_n as a device parameter has limitations in DSMs (Fakharuddin A. et al., 2014a; Fakharuddin, et al., 2014b). A similar idea is reported by Halme et al.,(2010) who suggested via device simulations that the possibility of electrons to be collected is higher if they are produced nearer to the working electrode substrate. However, an experimental validation it is not provided so far.

2.8 CONCLUSIONS

Immense research to elevate DSCs to a commercially deployable level has brought them to deliver η ~8.2% which is significantly lower than their laboratory scale analogues (13%, certified value of 11.9%). The routinely achieved J_{SC} in DSMs is 30 – 50% of that of high efficiency DSCs. Surprising is to note that the published reports on DSMs did not explain the origin of this significant loss of photogenerated electrons (Table 2.2, Appendix II). The inferior performance of DSMs is however attributed to their low FF which arises due to increase in series resistance while up-scaling DSCs: none of these studies explains the factors behind the drop in J_{SC}. We also note that there are no detailed charge transport investigations of the DSMs. Such fundamental studies are crucial to determine the factors behind the inferior performance of DSMs and to further improve the performance of these devices.

CHAPTER 3

EXPERIMENTAL METHODS

3.1 INTRODUCTION

This chapter highlights the research methodology as well as various materials and methods used in the present research to achieve the objectives. Various experimental designs for DSCs fabrication, the tools and techniques of characterizations, the possible errors, the precautions and correction made, and also the extraction mechanism of various charge transport parameters to identify the kinetics of the DSCs are described in this chapter.

3.2 RESEARCH METHODOLOGY

The methodology adopted to achieve the objectives of this research is summarized in flow chart 3.1. 3

The procedure starts by fabricating DSCs with varying areas while keeping other device physical parameters unchanged. The results are analyzed to develop novel device designs to offer improved charge collection efficiency.

Flow chart of research activities

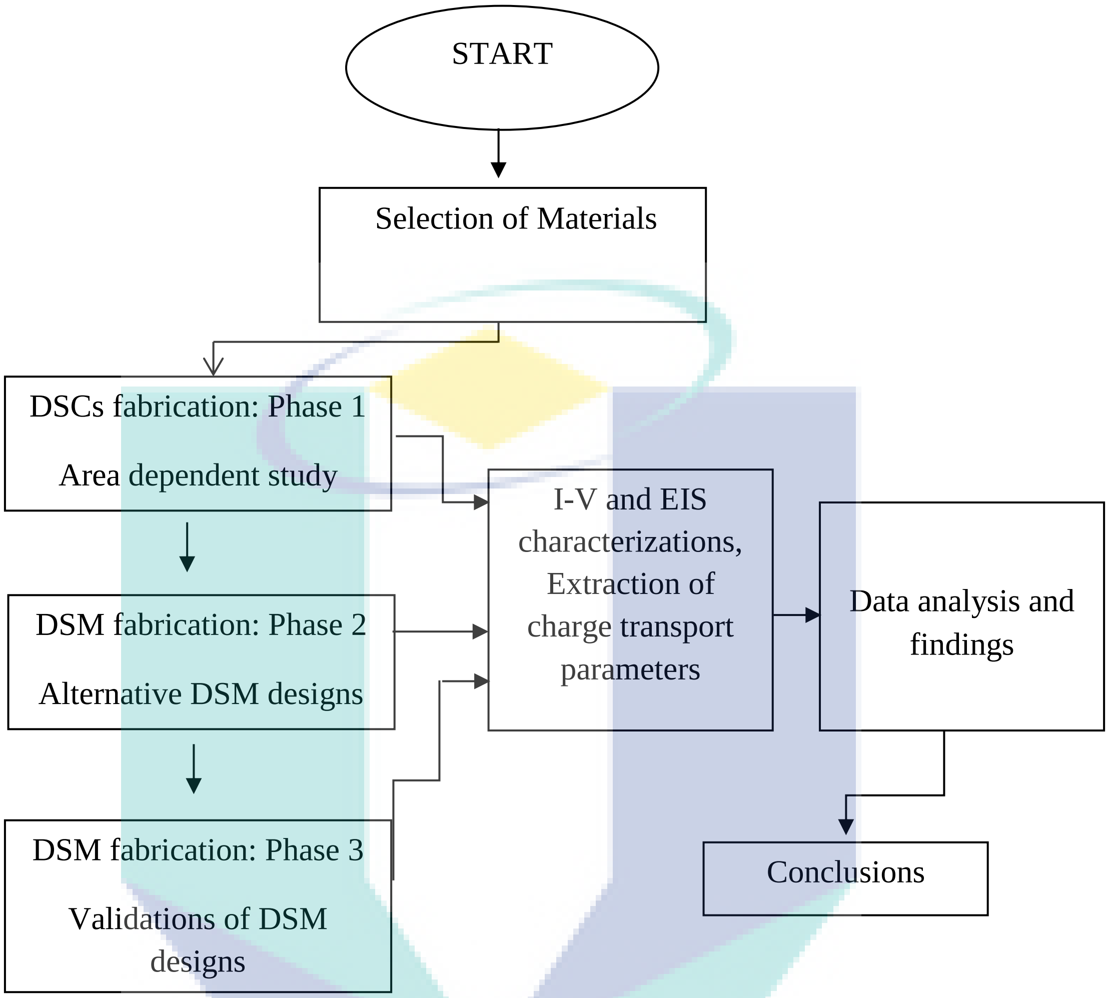

3.3 MATERIALS

Unless stated otherwise, the widely employed commercial DSC materials were used for fabrication of DSCs throughout this study. The solvents used in this study, viz., ethanol, acetone, hydrochloric acid (HCl), and titanium chloride ($TiCl_4$) were purchased from Sigma Alrdrich. Commercially available TiO_2 paste (Solaronix Ltd.) was employed as the mesoporous photoanode layer. The substrates (FTO), cis-bis(isothiocyanato)bis(2,2'-bipyridyl-4,4'-dicarboxylato)-ruthenium(II) (N3 dye), iodide/triiodide based redox electrolyte, platinum coated counter electrode , and surylin spacer (30 µm) were purchased from Solaronix Ltd.

3.4 PHOTOVOLTAIC FABRICATION

3.4.1 Phase 1: Area Dependent Photoanodes

The DSCs were fabricated on fluorine doped tin oxide coated glass substrates (FTO) using standard TiO_2 paste, cis-diisothiocyanato-bis(2,2'-bipyridyl-4,4'-dicarboxylic acid) ruthenium(II) (N3 dye), and the iodide/triiodide electrolyte. The FTO substrates were pre-cleaned by 15 min sonication in distilled water, ethanol and acetone. Pre-cleaning of substrates is crucial to remove any organic impurity on the surface of the FTOs which may lower the performance of the DSCs. The substrates were coated with a dense thin hole blocking layer via a 50 mM $TiCl_4$ solution treatment. The solution was made by adding $TiCl_4$ in distilled water at ~0 ^oC and then stirring vigoursly for 15 min. The pre-cleaned substrates were immersed in this solution and kept at 70 ^oC for 30 min to form a dense blocking layer. Eight areas were selected in the range 0.16 – 1.96 cm^2 for the present study. The TiO_2 paste was coated on the active areas by screen printing technique followed by drying at ~100 ^oC for ~2 – 3 h. Thus films were then sintered at an optimized ramping program at 450 ^oC for 30 min. The ramping program was as follows: 2 ^oC/min until 250 ^oC and stay of 10 min and 5 ^oC/min until 450 ^oC and stay of 30 min). We noticed that annealing of the TiO_2 films require intensive precision; crack in TiO_2 films are noticed otherwise. Translucent TiO_2 electrodes thus produced were anchored to the N3 dye by dissolving in a 1:1 volume mixture of acetonitrile and tert-butanol for 24 h at room temperature. The dye-sensitized samples were then washed in ethanol to remove unanchored dye and dried in air. Samples were sealed using a 50 μm spacer (Surilyn). Acetonitrile containing 0.1M lithium iodide, 0.03M iodine, 0.5M 4-*tert*-butylpyridine and 0.6M 1-propyl-2,3-dimethyl imidazolium iodide was used as the electrolyte. A great care is to be given while filling the electrolyte as an improper filling may cause air to be trapped inside the gap which affects the performance of DSCs. A platinum coated FTO glass was used as the counter electrode.

Screen printing of the working electrode

Various techniques are adopted to develop TiO_2 films on working electrodes such as doctor blading, spin coating, dip coating and also the screen printing. Among all these techniques, screen printing is preferred as it is commercially viable, offer precision when specific dimension are required for the TiO_2 strips, and the mesoporous layers formed by this technique do not experience any cracking unlike doctor blading. For TiO_2 coating we optimized various types of screen with different mesh size (70 T, 100 T and 140 T) and also various thread size and spacing. The films were coated via a squeegee method which is a commercially adopted method for printing in textile industry and can be applied to print on glass substrates.

3.4.2 Alternative Designs With to Improve Charge Collection

Based on the insight gained from first experimental phase, we attempted various designs for large area DSCs. The primary idea was to restrict electronic transport by appropriate photoanode dimensions for a complete charge collection. To do so, we undertook the individual cell/stack size as small as 1 – 100 mm^2. We also investigated the effect of the interspacing between neighbouring cells by varying it between 0.2 mm – 2 mm. These designs and their photovoltaic properties are elaborated in chapter 5.

3.4.3 Validation of Split Photoanodes

In order to validate the effect of split or stacked photoanode designs (section 3.4.2), we compared the performance for a split design DSC of an active area (0.28 cm^2) with its conventional analogues. Three sets of DSCs were fabricated in this study with differing photoelectrode geometry. The first set of devices (S1) has a photoelectrode area of ~0.28 cm^2 in the form of a rectangular strip. In the second set (S2), a similar area is created by splitting a single cell of area ~0.28 cm^2 into two strips of areas ~0.14 cm^2 each with a spacing of ~0.2 mm. The third set (S3) composed of four strips of area 0.07 cm^2 each with similar interspacing such that the total photoelectrode area is ~0.28 cm^2. The DSCs were fabricated using a standard procedure as described in section 3.4.1. In brief, standard TiO_2 paste (Solaronix) was screen printed on FTO coated glass substrates, dried at 80 ^oC in an electrical oven and subsequently sintered at 450 ^oC. The sintered films were immersed overnight in 0.3 mM solution of N3 dye in acetonitrile and tert-butanol (1:1 volume ratio). The electrodes were then washed in ethanol to remove unanchored dye and dried in air. Devices were sealed using a 50 µm spacer. A Platinum sputtered FTO glass was used as the counter electrode. The I_3/I^- electrolyte was injected to the spacer region through previously developed micro-holes.

3.5 INSTRUMENTAL AND CHARACTERIZATIONS

3.5.1 Surface and Morphology of Thin Films

Surface homogeneity of the films was evaluated by scanning electron microscopy (FE-SEM, JEOL, USA). Although there are other methods available to measure the surface of a thin film such as atomic force microscopy (AFM) and the thickness of a film such as surface profilometery but these methods yield limited information for DSC photoanodes. The AFM provides information about the surface homogeneity and not the thickness and the porosity of the film as AFM can only image a height of ~10 µm whereas the SEM can image up to few millimetres. Similarly, surface profilometer only provide information about the thickness of the film and yields no information about the surface morphology and surface composition of the thin films. Imaging of thin film via SEM provides more detailed information compared to the other two techniques.

An instrumental diagram of SEM is given in Figure 3.1. In general, a sample is placed in a vacuumed chamber on a sample mount. The electron beam generated thermionically from a field emission source is accelerated in a field gradient. The electron beam of energy ~0.5 – 40 kV is focused by condenser lenses to form a spot size up to ~5 nm. The electrons penetrate via a vertical column into the chamber and interact with the atoms in the sample under test. Consequently, various types of electrons are emitted from the sample under test such as back scattered and secondary electrons (SE), each of which can be detected via a specialized detector. A detector catches the secondary electrons and compares the intensity of these SEs with that of primary electron beam to form sample. The resulting image is therefore a distribution map of the intensity of the signal being emitted from the scanned area of the specimen.

To investigate the surface morphology and the thickness of our film, we cut our annealed thin film on FTO via a glass cutter to have a cross sectional analysis. Extreme care is required while breaking a coated FTO so as to avoid any physical contact with the exposed thin film area. The samples were the coated with platinum to make them conducting and to avoid any possible charging effect during measurement. The samples were then loaded into the measurement chamber of the FESEM. The analysis revealed the thickness of the photoanode film to be ~14±0.7 μm.

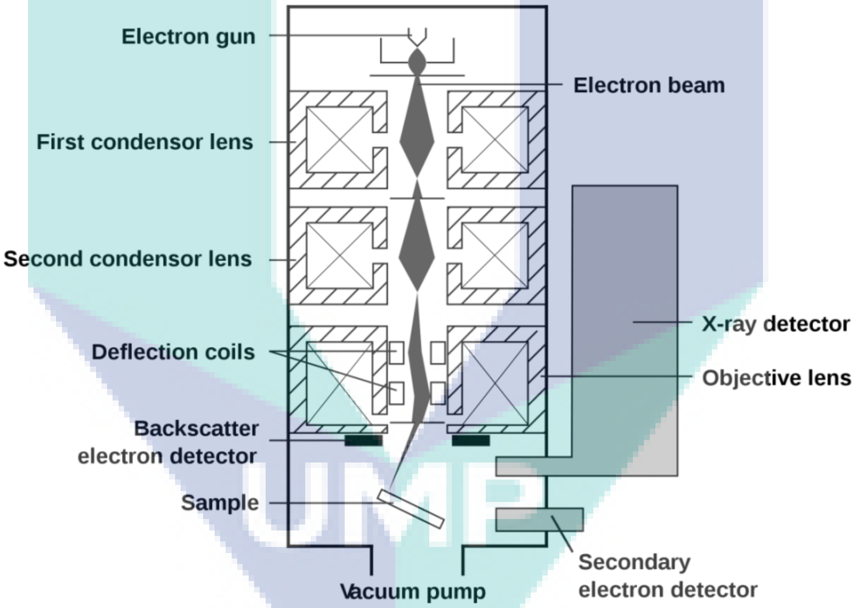

Figure 3.1: General block diagram of a scanning electron microscopy.

Adopted from Modern Techniques of Materials Characterisation page#128

3.5.2 UV-VIS Spectrophotometer

Absorption spectra of the dye-anchored electrodes and desorbed dye solution were recorded using UV-VIS-NIR spectrophotometer (UV-2600 of Shimadzu with integrated sphere 2600 plus). In general, a UV-VIS absorption spectrometer consists of a light source, a monochromater, a sample and a reference holder, and a detector (Figure 3.2). The monochromater employs optical dispersion to spatially separate individual wavelengths. Normally, the resolution, i.e., the monochrmomaticity, improves with narrow slit width but the power decreases as the square of the slit width (10-fold narrower slit gives 100× less radiant power).

In the absorption spectrometer, the incident light from the light source is split into two beams; one of the beams passes through the sample whereas the other passes through a reference. The absorption spectrum is the difference in intensity of the above two emergent beams as a function of wavelength, which contains the absorption property of the sample. In liquid samples the reference is usually a solvent. However, in the sample in this study was solid, therefore, we used a properly cleaned FTO as reference. The absorbance and transmittance are calculated from the intensity of incident light and the light detected by the detector after passing through the sample. Usually, $T = I_T/I_O$, where T is the transmittance, I_T is the transmitted light through the samples and detected by the detector, and I_O is the intensity of the incident light. The absorbance which is $\log_{10}(1/T)$ is given by the relation, $Abs = \varepsilon C l$. The relation is called “Lambert-Beer law” which expresses the relationship between the absorbance, Abs, the sample concentration, C, optical path length, l, and ε is the molar absorption coefficient (extinction coefficient)

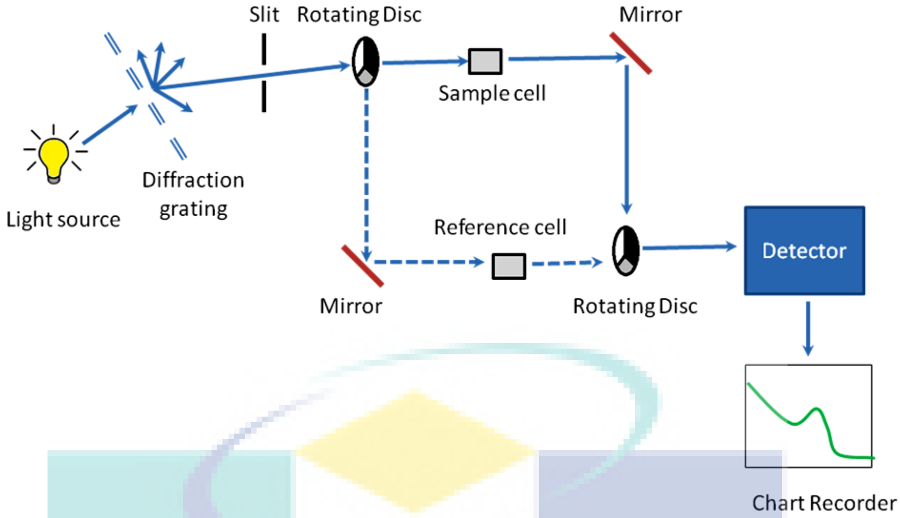

Figure 3.2: A simplified block diagram of UV-VIS spectrophotometer.

Absorbance and dye-loading of thin films

The dye loading of the photoanodes was measured by desorption test. The dye was desorbed by immersing them in 0.5 M NaOH and the absorption spectra of the solutions were recorded using a UV–VIS NIR spectrophotometer. The dye loading was calculated using Lambert-Beer law. The molar absorption coefficient (ε) of the N3 dye used in this work is 1.41×10^4 $\mathrm{Lmol^{-1}cm^{-1}}$

3.5.3 Current – Voltage Characteristics Measurements

Photocurrent measurements were performed using a solar simulator (SOLAR LIGHT, Model 16-S 150; Figure 3.3) employing single port simulator with power supply (XPS 400) at AM1.5G condition (1000 mW/cm^2 & 25 $^{\circ}$C). I-V curves were measured using a potentiostat (Autolab PGSTAT30, Eco Chemie B.V., The power of the solar simulator was calibrated to 1000 mW/m^2 via a reference Si cell in order to reduce the possible mismatch between the simulated light and AM 1.5 G in visible region to <5%. Linear sweep voltametery (LSV) was used as a measurement method. In LSV, a fixed potential range is employed at the working electrode from a lower limit to upper limit and the response (current) is measured as a function of voltage. The voltage step was 20 mV and the delay time was kept 50 ms for all the measurements.

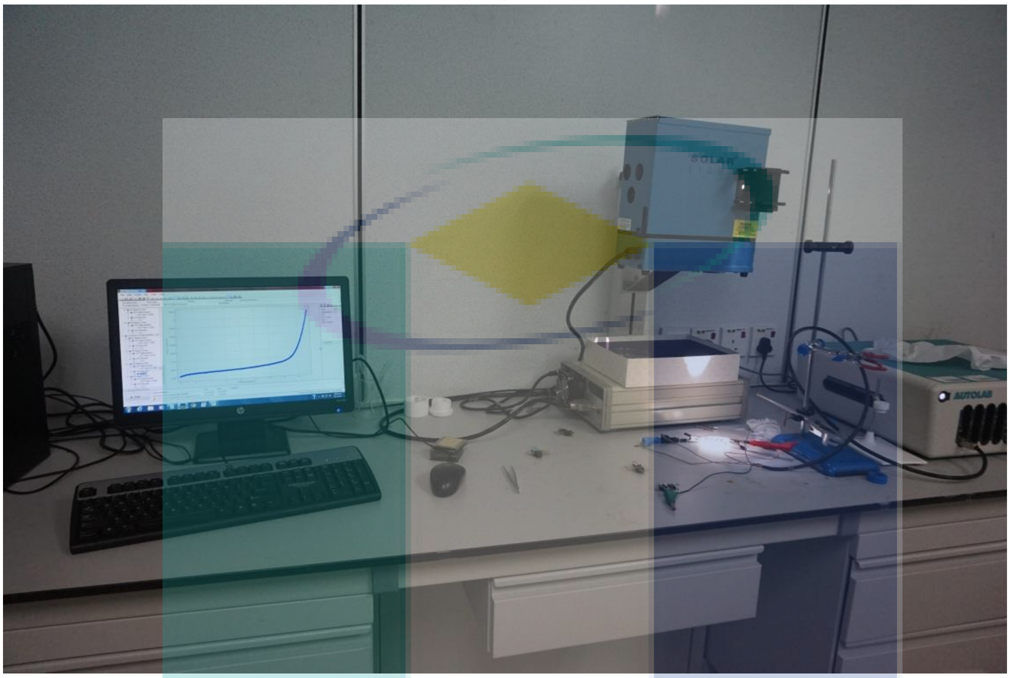

Figure 3.3: Solar simulator setup used to measure I-V characterization curves of DSCs.

The function of a solar simulator is to provide illumination similar to that of natural sunlight which is used as controllable indoor testing equipment at laboratory conditions. According to IEC standards (IEC 60904-9) the solar simulator used for photovoltaic testing should precisely meet the three key requirements which are (i) spectral contents, (ii) spatial uniformity, and (iii) temporal stability. The goodness of a solar simulator, called class, is determined by how precisely a solar simulator fulfil the above criteria. The solar simulators mostly employ a Xenon lamp (Figure 3.43) as light source however metal halides, halogen lamps and light emitting diodes based lamps are also seldom employed. Xenon lamps are mostly adopted as they offer high intensities and an unfiltered spectrum which matches closely to natural sunlight. However, their output spectrum demonstrates few undesirable sharp atomic transitional peaks as will be discussed in section 3.6.1.

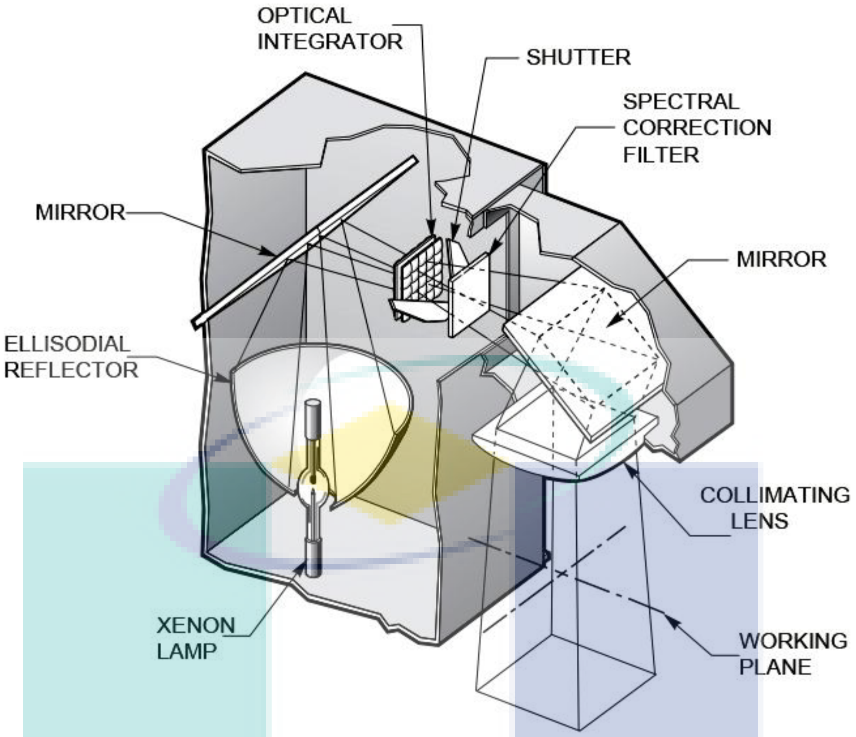

Figure 3.4: Cross-sectional view of the simulator.

Adopted from www.newport.com/oriel

3.5.4 Electrochemical Impedance Spectrophotometer

The charge transport properties of the DSCs were studied using the Autolab PGSTAT30 (Figure 3.5a) employing the NOVA® software. The devices were scanned in a frequency range of 100 kHz to 0.1 Hz for electrochemical impedance spectroscopy (EIS) analysis. The electrochemical impedance spectroscopy (EIS) is a method of characterizing many of the electrical properties of materials and their interfaces with electrically conducting electrodes. In general, impedance is the total opposition to the current flow in an alternating current circuit, ($Z=E/I$). It is also called the sum of the ohmic resistance and reactance and is represented as $Z = R + iX$. The impedance is a complex quantity with a magnitude and a phase shift which depends on the frequency of the input signal. Therefore by varying the frequency of the applied signal one can get the impedance of the system as a function of frequency.

For electrochemical measurements, the device is kept under dark and an input signal is applied to it. The applied signal is a superposition of a low amplitude sine wave of frequency ω is superimposed on a DC voltage E_0 thereby resulting in a current response that shifts with the applied potential. The applied AC signal was varied from 0.4 – 0.7V.

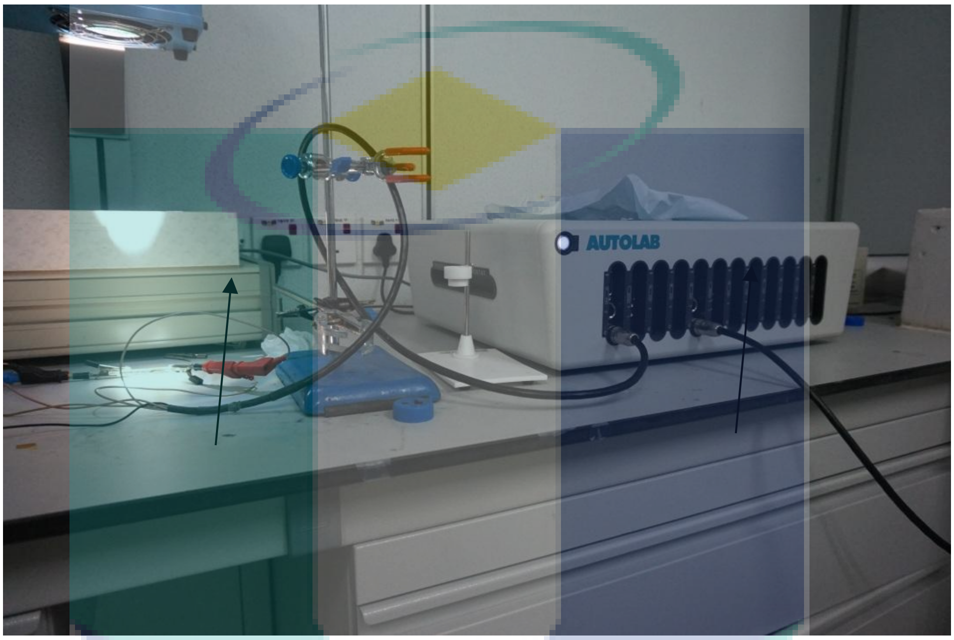

Figure 3.5 (a): Multi-channel potentiostat/galvanostat used for DSC measurements.

Figure 3.5b shows a general block diagram of an impedance spectrophotometer. It mainly consists of two units, a frequency response analyzer (FRA) and an analogue PGSTAT. In a typical electrochemical impedance measurement, the FRA module generates a sine wave with a user-defined frequency and small amplitude which is superimposed on the applied DC signal on the cell. The AC voltage and current components are analyzed by the two FRA channels and the transfer function, the total impedance Z, is calculated, together with the phase angle shift and the real and imaginary components of the total impedance.

The total impedance ‘Z’ is given by, $Z = Z' - jZ''$, and the phase angle by, $\theta = \tan^{-1}(Z''/Z')$. The output current is measured across working and counter electrodes and whereas the voltage is measured across the secondary and the reference electrode.

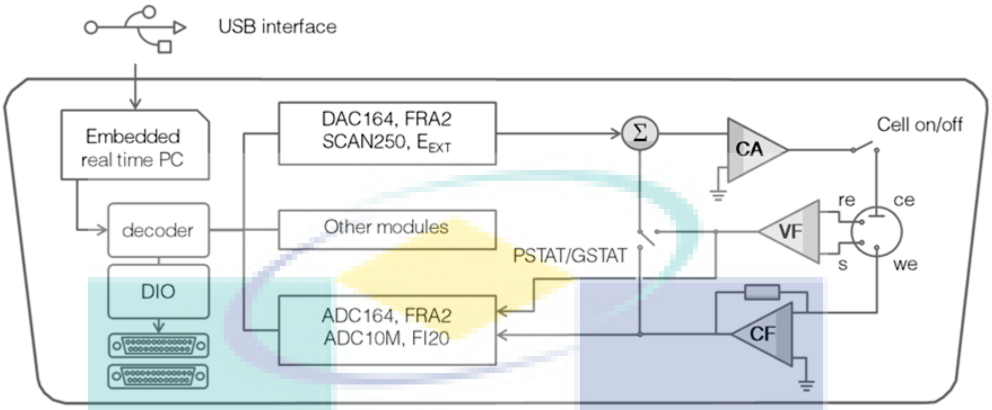

Figure 3.5 (b): General block diagram of an impedance spectrophotometer.

3.4.5 The Electrical Equivalent Circuit of DSCs

For a porous thin layer, an infinite transmission line model (Figure 3.6) is used for circuit modeling (Bisquert J., 2002) but for simplicity, the model is generalized for representative elements only. Figure 3.7 shows a generalized model used for fitting the impedance data. This model corresponds to four interfaces in a DSC and various processes at those interfaces, i.e. (i) electron transfer at FTO/semiconductor interface, (ii) electron transport and recombination at semiconductor/electrolyte interface, (iii) diffusion of iodide/triodide ions in electrolyte, and (iv) electron transfer at Pt/counter electrode interface (Wang Q et al., 2005a). The impedance response of such a system is represented as,

$$Z_{IF} = 2\left(\frac{R_T}{R_{CT}}\right)^{1/2} \frac{1}{C_\mu}\left(i\omega_{CT}\right)^{-\beta} \qquad (3.1)$$

where R_T ($=r_tL$) is the transport resistance, i.e., total resistance offered by the photoelectrode film; R_{CT} ($=r_{ct}/L$) is the resistance to the charge transfer from the photoelectrode to the electrolyte; C_μ ($=c_\mu L$) is the chemical capacitance; and ω_{CT} is the characteristic frequency at which the charge transfer occurs.

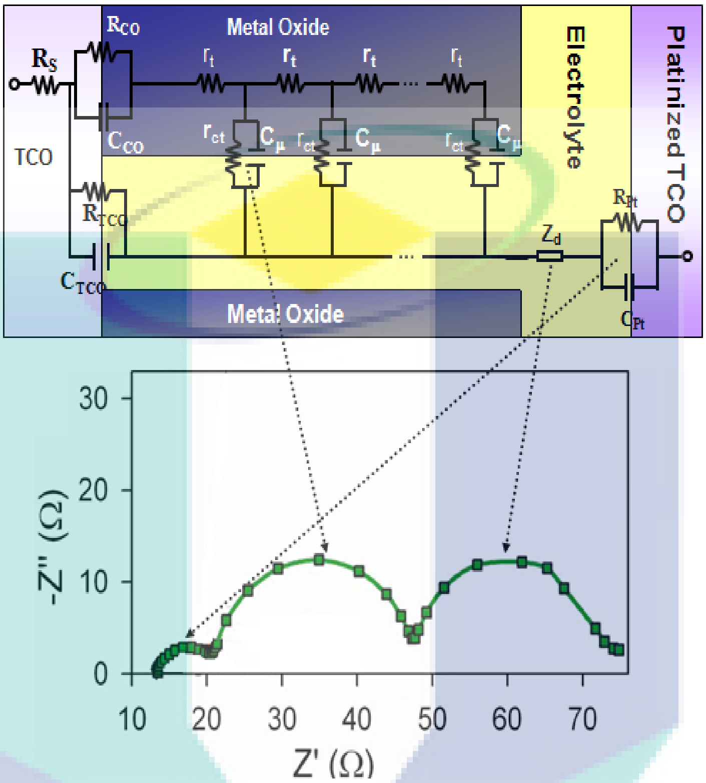

Figure 3.6: A transmission line model representing various interfaces in the DSCs in the form of electrical equivalent circuit.

The simplified electrical equivalent of devices used for curved fitting process is shown in Figure 3.7.

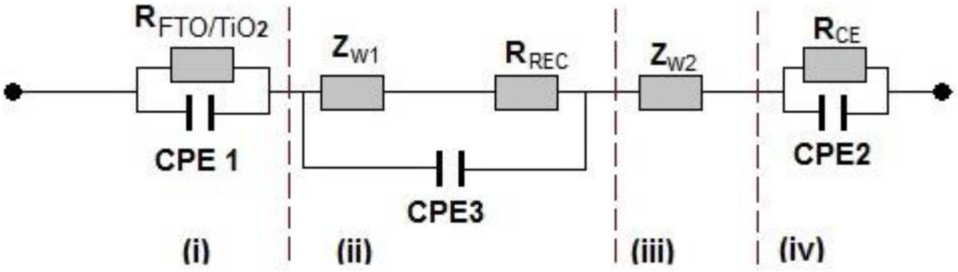

Figure 3.7: A simplified transmission line model used for fitting impedance data.
Source: (Fakharuddin A. et al., 2014b)

Here, RFTO/TiO_2 is the FTO/semiconductor interface resistance, Z_{W1} is the Warburg diffusion element related to diffusion of I_3^- inside TiO_2 and Z_{W2} is diffusion element related to I_3^- diffusion in the electrolyte.

3.4.6 Extraction of charge transport parameters

The charge transport parameters such as R_T, R_{CT} (also called recombination resistance, R_{REC}), C_μ are calculated from the impedance data (Nyquist and Bode plot) using curve fitting method (Z-view 3a) by applying a well-known electrical equivalent model by Bisquert et al., (2002) as shown in Figure 3.6. Both, the real and imaginary parts were fitted simultaneously using the “calc-modulus” as “data weighing option” at absolute temperature 293 K. The iterations were performed to receive an optimum fit (chi-square $\leq 10^{-5}$) to extract reliable values. These three transport parameters are related to individual components in the transmission line model as shown in following relations, ($r_t = R_T$.A/d, $r_{ct}=R_{CT}$.Ad, and $c_\mu=C_\mu$/(A.d)), where ‘A’ is the photoelectrode active area and ‘d’ is the film thickness (Wang Q. et al., 2005b; Bisquert J., 2008; Jennings J.R. et al., 2011). The units for the distributed parameters r_t, r_{ct}, and c_μ are then Ωcm, Ωcm^3, and F cm^{-3}, respectively (Jennings J.R, et al., 2011).

3.5 PHOTOVOLTAIC DEFINITIONS

In this section we explain various common terms used while analysing the performance of a solar cell.

Short circuit current (I_{SC}) is the current measured at short circuit or zero potential and is expressed in Ampere units (mA or A) whereas short circuit current density (J_{SC}) is the current per unit area (unit: mA/cm^2).

Open Circuit Voltage (V_{OC}) is the external bias at which the I_{SC} is zero.

Fill Factor (FF) is the ratio between of a solar cell's actual power output ($V_{PMAX} \times I_{PMAX}$) versus its 'dummy/theoretical' power output ($V_{OC} \times I_{SC}$). It is a key parameter in evaluating the performance of solar cells. A cell with higher FF has less parasitic losses, i.e., losses due to the series and parallel resistances within the device.

$$FF = I_{MP} \times V_{MP}/I_{SC} \times V_{OC} \tag{3.2}$$

Or

$$FF = \text{Area A}/\text{Area B}$$

Graphically, the FF is a measure of the "squareness" of a solar cell. It is also the area of the largest rectangle which will fit in the J-V curve as shown in Figure 3.8.

Photoconversion efficiency (η) is the ratio of power output (P_{MAX}) from a solar cell to the incident solar intensity (P_{IN}) and is expressed in percentage.

$$\eta = P_{MAX}/P_{IN} = J_{SC}.V_{OC}.FF/P_{IN} \tag{3.3}$$

Solar Irradiance is the flux or radiative power density on a surface. It is usually measured in W m^{-2} or W cm^{-2}.

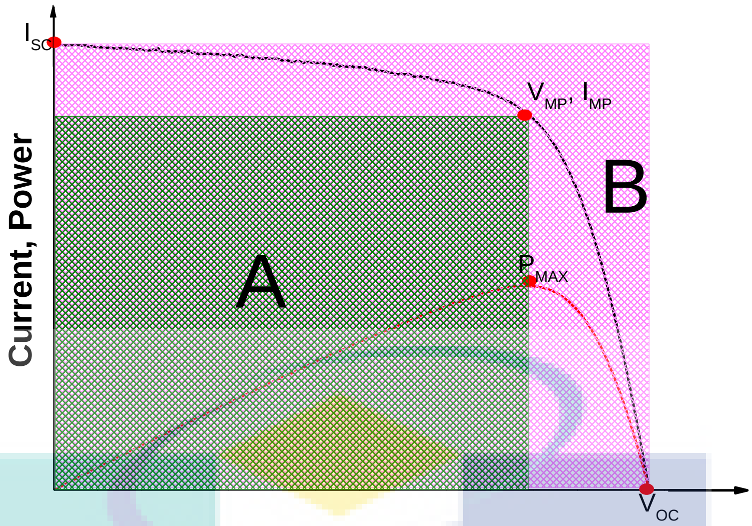

Figure 3.8: Current-voltage curve of a DSC showing the calculation of FF.

AM 1.5 G is a standard protocol for solar cells measurements and is abbreviation of air mass 1.5. It corresponds to the spectrum of the sunlight at sea level after traversing the atmosphere 1.5 times. Generally, the AM 1.5 conditions represents an incident solar irradiation of 1000 mW/m^2 or 100 mW/cm^2 at 25 ^{o}C. Such a standard is necessary to compare the performance of solar cells developed in different laboratories around the world.

Spectral Mismatch and Calibration

Solar simulator always has a different spectrum from AM 1.5 conditions, even when corrected with appropriate 'sunlight filters'. Such a spectral mismatch difference is quantified as: (Clay H., 1982)

$$M = M_{RC}.M_{TC}^{-1} = \frac{\int E_{AM1.5}(\lambda)S^{RC}(\lambda)d\lambda}{\int E_{sim}(\lambda)S^{RC}(\lambda)d\lambda}.\frac{\int E_{sim}(\lambda)S^{TC}(\lambda)d\lambda}{\int E_{AM1.5}(\lambda)S^{TC}(\lambda)d\lambda} \tag{3.4}$$

$E_{AM1.5}(\lambda).E_{sim}(\lambda)$ = relative spectral irradiation intensity of AM1.5 and the light from solar simulator

$S_{RC}(\lambda)$ = spectral intensity of reference cell

$S_{TC}(\lambda)$ = spectral intensity of test cell

A reference cell (RC) is calibrated at standard test conditions (AM 1.5; 1000W/m^2, T 25 ^{o}C) and the value of the short circuit current ($I_{AM1.5}^{RC}$) under these conditions is specified. The calibrated reference cell is used to calibrate the output of a solar simulator whose overall radiation output is not known to measure the photovoltaic output of a cell under test. The photoresponse of the cell under test is then measured.

We calibrated our photovoltaic setup using a silicon solar cell as a reference cell and using and UV pass filter (transmit in visible region and absorb in UV and IR region). The spectral response of the cell under test is matched with the reference cell in visible region as DSCs are not sensitive in IR region. A xenon lamp was used as a light source exhibiting spectral responses similar to AM1.5 sunlight.

Forward/Reverse Bias. The forward bias is the potential applied to a solar cell (in general to any electronic device) when the n-type material is negatively charged and the p-type material positively charged. In reverse bias, the n and p – type are connected to opposite polarization.

Front/Back Illumination. When the FTO is exposed to face the incident solar light, it is called a front side illumination while back side illumination is defined as the illumination through the counter electrode.

3.6 POSSIBLE ERRORS DURING PHOTOVOLTAIC MEASUREMENTS

The performance of DSCs are often over or underestimated due to various possible errors during characterization such as calibration of solar simulator, the measurement time for I-V measurements and incident photon to current conversion efficiency, and the active area determination (Yang et al., 2013). A reliable measurement of the device is crucial to evaluate its performance in order to compare the progress from various groups around the world. Here we highlight few such common errors that can mislead the performance of a solar cell.

3.6.1 Solar Simulator (Light Source)

The performance of a solar cells is determined using a solar simulator under AM 1.5G. The solar simulator usually employs a Xenon lamp that can provide solar light of various intensities. The spectrum of such simulated light is matched with the visible light spectrum by employing filters to avoid over estimation of the photovoltaic parameters. However, as suggested by Yang et al., (2013) such solar simulators are often characterized by few unwanted sharp atomic peaks at ~450 nm and 650 – 850 nm as shown in Figure 3.9. The high intensity of these peaks results in over estimation of J_{SC} in devices. To avoid such over intensity, the solar simulator is to be calibrated using a standard cell and employing various filters such that the reference cell generate the same photocurrent as recorded in the first calibration (given in data sheet). As the dye employed in our study (N3) mainly covers 300 nm – 700 nm, a KG-5 filter is employed to minimize any possibility of over estimation of photocurrent. For dyes with broader spectral light harvesting such as N 749 (black dye, the spectral response extends to ~850 nm) solar simulator need to be calibrated with KG-3 filter.

Another common issue with the solar simulator is the aging effect. The spectrum and the solar irradiation intensity vary with its age (Yang et al., 2013). The light intensity in our study is calibrated using a Lux meter to 100±2 mW/cm^2.

3.6.2 Equilibrium Conditions During Steady State Measurements

The steady state measurements of solar cells such as current-voltage and IPCE measurements should be performed when the device under test is in equilibrium. A possible non-equilibrium in the cells which is caused by a variation in experimental conditions such as temperature, step voltage or the incident light intensity requires a delay time so that the system could reach to equilibrium state. This is crucial as significant dependence of delay time is found on the photovoltaic parameters. Yang et al., (2013) observed 11% over estimation of J_{SC} when the delay time was changed from 5000 ms to 5 ms under the same experimental conditions. The electrolyte plays an important role for a system to reach equilibrium; in electrolytes of high viscosity the slower ion diffusion may induce a large equilibrium time constant which require a longer delay time. The time constant for a device can be measured by transient photocurrent measurements under the action of a stepwise voltage change. For the DSCs containing 30 – 50 mM iodide/triiodide based electrolyte in acetonitrile, a delay time of 50 ms is considered reliable for measurements (yang et al., 2013). In our experiments, we used the same delay time (~50 ms) and a voltage step size of 20 mV.

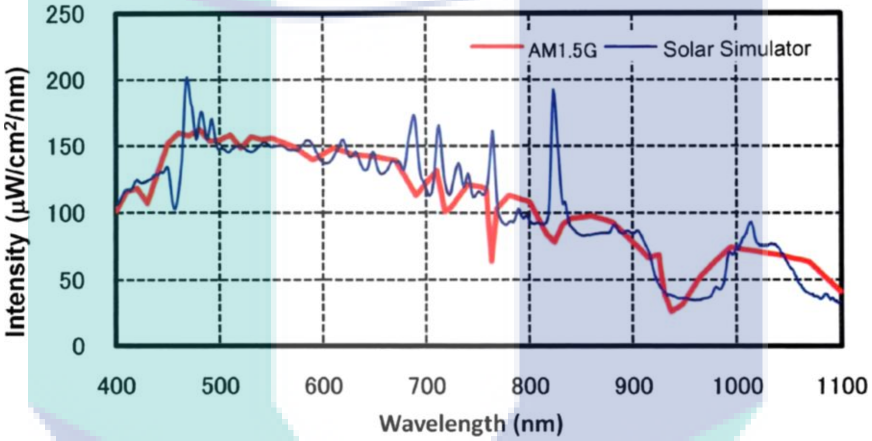

Figure 3.9: Comparative spectra of AM 1.5 G solar light (red) and AM 1.5G solar light from a solar simulator (blue).

Adopted with permission from The Royal Society of Chemistry (yang et al., 2013).

3.6.3 Masking and Determination of Active Area

The determination of correct active area is most important factor while reporting the performance of solar cell. Reporting the DSCs performance without a mask is a common practice in global research community which often leads to ≥10% over estimation of photocurrent (Snaith H.J., 2012). In a report by Yang et al., (2013) ~30% over estimation in J_{SC} is observed when a DSC is tested without a mask compared with a masked device. In the un-masked DSCs, the incident light is reflected from the FTO substrate back into the TiO_2 film and the absorption of light at the edges of the DSCs will also induce extra solar irradiations as shown in Figure 3.10. As the irradiated area by a solar simulator (~2–5 cm^2) is much larger than the active area of the DSC (~0.25 cm^2), the incident light may penetrate from the edges and will cause an over estimation in photovoltaic parameters. Covering a DSC with shaded mask will eliminate such possible error and the photovoltaic parameters will be calculated by considering the aperture area of the mask only.

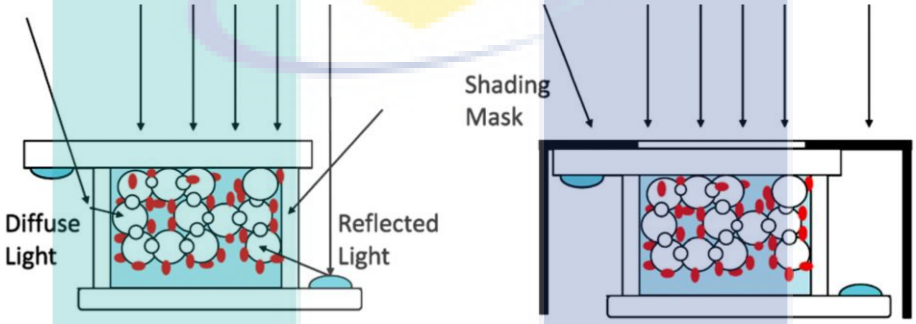

Figure 3.10: The incident solar irradiation on a masked and un-masked DSC.

Adopted with permission from The Royal Society of Chemistry (yang et al., 2013).

The shaded mask however need to completely opaque to block complete light transmission (0%) and minimum light reflection (<5%) in UV to NIR region. A steel mask (~0.3 mm thick) with black surface is recommended to fulfil such criteria. In our studies (chapter 4 & 6), we employ a thick mask with ~0% transmittance and reflectance as low as 3-4%. In our experiments we kept the aperture area of the mask smaller than the active area due to the fact that a larger aperture area than the active area may induce the measurement errors arising from light diffusion, reflection and absorption from the surrounding area.

3.7 CONCLUSIONS

In conclusion, the various materials and methods used in the present study are discussed in detail. A detailed description is provided on the fabrication and characterization (electrical, optical and electrochemical impedance spectroscopy; EIS) of DSCs for three different phases. A detailed section on EIS characterization and the extraction of charge transport parameters is given. Lastly, the various possible errors during fabrication and measurement of DSCs are highlighted and the solutions adopted in our experiments are also elaborated.

CHAPTER 4

AREA DEPENDENT PHOTOVOLTAIC PERFORMANCE IN DSCs

4.1 INTRODUCTION

One of the primary issues to be addressed to scale up the DSCs is to deeply understand the variation of photovoltaic properties of the device as a function of device area. The effect of the photoelectrode area (0.16 – 2 cm^2) on its photovoltaic performance is addressed in this chapter. The DSCs under investigation were fabricated using commercial TiO_2 paste, cis-diisothiocyanato-bis(2,2’-bipyridyl-4,4’-dicarboxylic acid) ruthenium(II) (N3) dye, and iodide/triiodide electrolyte. The cells were characterized by current–voltage and electrochemical impedance spectroscopy (EIS) studies.

4.2 PHOTOANODE CHARACTERIZATION

4.2.1 TiO_2 Film Morphology and Porosity

Morphology and thickness of the electrodes were characterized by FESEM. Figure 4.1a is a typical SEM image of an electrode cross-section on FTO substrate showing the thickness and porosity of a sintered TiO_2. Thickness of the photoelectrode films was 14±0.2 µm, which is a value within the diffusion length (L_n) of the TiO_2 nanoparticulate photoelectrodes for efficient charge collection (Gonzalez-V. et al, 2010 and Fisher et al., 2000). No particle coarsening was observed during sintering; the film consists of nanoparticles of ~30 nm (Figure 4.1b). Figure 4.1b further reveals porous structure of the sintered photoelectrode required for proper electrolyte penetration. One of the primary characteristics of a photoelectrode film in DSCs is the porous electrode with strong bonding with the substrate. A good adhesion of the films with the substrate was confirmed using a peel-off test (Appendix III). All the electrodes developed in this study were porous and adhered very well with the substrate.

The chemical structure of the nanoparticles is verified by XRD analysis and is shown in Figure 4.1c. The XRD pattern shows that the films are made of TiO_2 nanoparticles of Anatase phase. The chemical structure of TiO_2 film did not change upon dye anchoring as shown in Appendix IV.

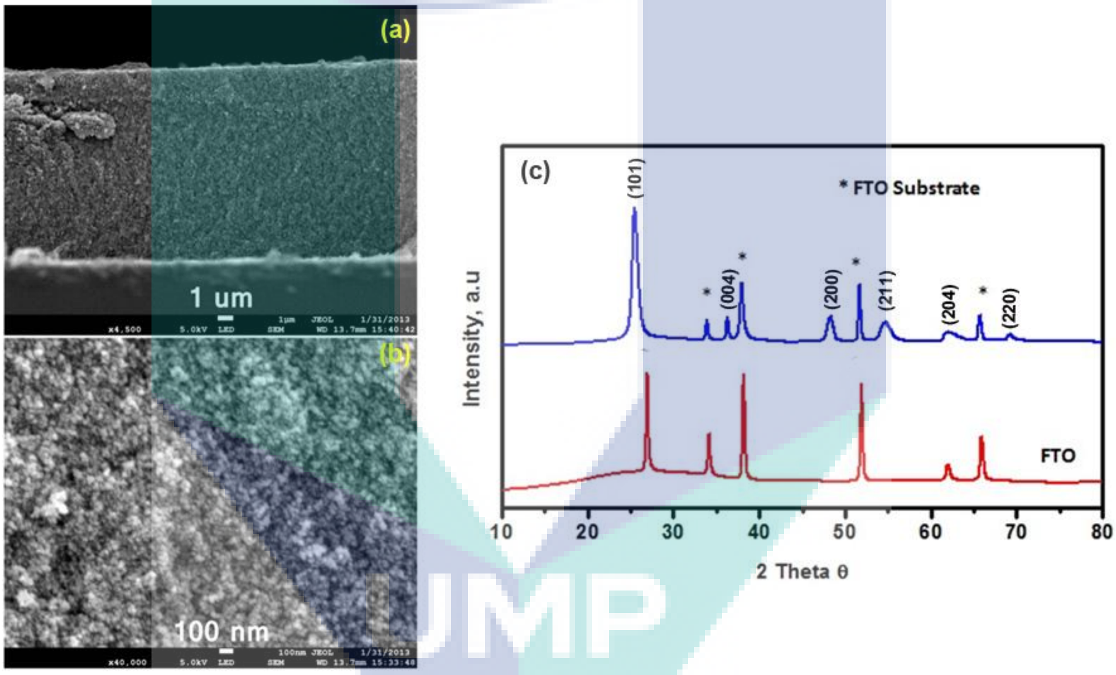

Figure 4.1: SEM images showing (a) cross-section of a typical photoelectrode of ~14 µm thickness, (b) a closer view of photoelectrode shows porous photoelectrode surface for appropriate electrolyte filling, and (c) XRD pattern of sintered TiO_2 film.

4.2.2 Calculation of Dye Loading in Photoanodes

As dyes are the primary absorbers in DSCs, knowledge on the dye loading is essential to determine whether or not any difference in the photovoltaic properties arise from a difference in dye-loading. The dye-loading on the electrodes were studied by UV-VIS absorption spectroscopy. Figure 4.2 shows the absorbance and reflectance spectra of the dye-anchored electrodes. FTO plate with no additional coating was used as the reference during measurements. The ~14 μm thick electrodes showed two characteristics peaks at ~335 nm and 521 nm attributed to peak absorption of TiO_2 and N3 dye respectively. The normalized dye-loading with respect the area of the electrode, measured from the desorption test, is similar ($\sim 1.4 - 1.5\times10^{-6}$ molcm^{-2}) for all the electrodes (Calculations are given in Appendix V) following the method of Xiaxou et. al (2013). The low transmittance in Figure 4.2 (<20%) in the range 300–600 nm is due to strong absorption of the N3 dye; which is further evident from the remarkably increased absorbance in this region (>80%). The SEM and the absorption features conclude the similarity of the sintered photoelectrode films; therefore, variation in their photovoltaic characteristics does not arise from a difference in their bonding with the substrate or absorption characteristics of the electrodes.

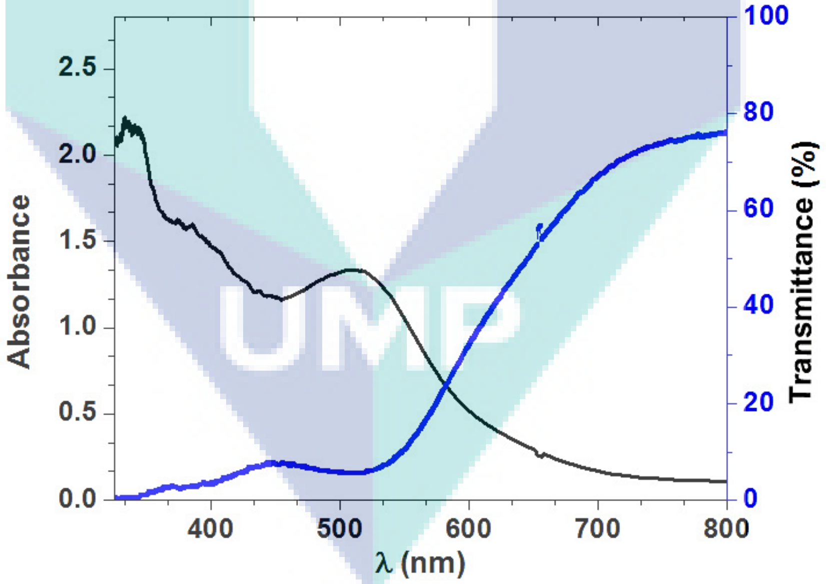

Figure 4.2: UV-VIS spectra of prepared electrodes employing mesoporous TiO_2. A bare FTO is used as reference for absorbance and transmittance measurements.

4.3 CURRENT – VOLTAGE CHARACTERIZATION OF THE DSCs

Figures 4.3 (a&b) show current density (J)–voltage (V) characteristics of DSCs as a function of device area normalized for a thickness of 14 μm and power output of a typical cell, respectively. The DSCs of area ~0.16 cm^2 showed the highest η ~6.74% with V_{OC} ~0.78 V; J_{SC} ~13 mA/cm^2; FF ~0.66. Requirement of high efficiencies in DSCs are (i) compact but porous electrode, (ii) highly purified dyes, (iii) presence of scattering layers to enhance light sensitivity (Ito S. et al., 2008). No scattering layers were used in the present experiments as well as the dyes were as-received and without any further purification; and therefore, the efficiency achieved in these cells are of acceptable quality. Quality of the cells can also be determined from the shunt (R_{SH}) and series (R_S) resistances, which could be calculated from the inverse of slops at J_{SC} and V_{OC} of the J-V curves, respectively(Priyanka et. al., 2007 & Pysch D. et. al., 2007).

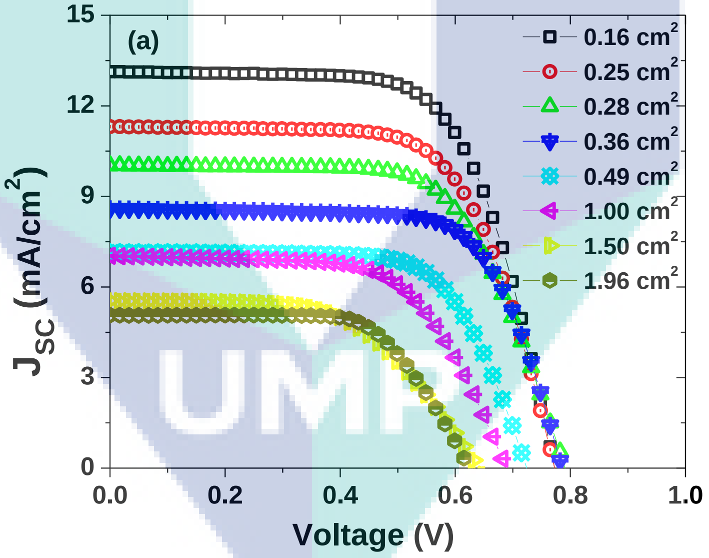

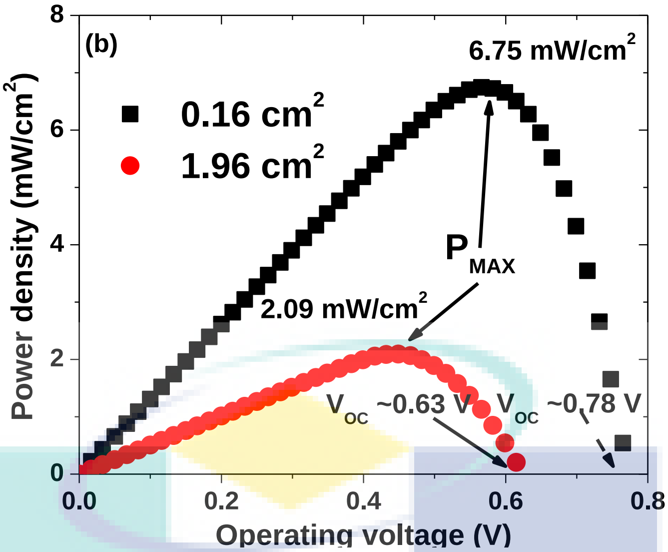

Figure 4.3: (a) Current – voltage characteristics of devices measured at AM 1.5 conditions. (B) Representative power output curves showing the relative shifts in V_{OC} and maximum power output.

The R_{SH} is an estimation of internal currents in the cell and is a measure of back electron transfer and other charge recombination processes in DSCs whereas R_S denotes the series resistance of the substrate. A high R_{SH} (>1000 Ω) and low R_S (<0.01 Ω) are preferred for high FF and η of the solar cells (Fakharuddin, et al., 2013a). All the cells developed here have high R_{SH} (~4000 – 5000 Ω) and low R_S indicating that area of the cells does not have any detrimental effects on R_S and R_{SH}. Figure 4.3(b), which shows the power output of the DSCs as a function of operating voltage, further confirm the quality of the devices, the relative changes in the maximum power point (M_{PP}), V_{OC}, and J_{SC} were such that FF remained nearly the same. Equally important is to note that the DSC with the smallest photoanode area (~0.16 cm^2) yielded ~3 times higher power output/cm^2 compared to the largest area photoanode (~1.96 cm^2).

On increasing the area of the cell to ~1.96 cm^2, the η decreased by a factor of ~ 4 and the J_{SC} by ~3. Figure 4.4 shows the variation in η as a function of device area, which is fitted to biexponential decay. The constants of fitting are in the inset of the Figure 4.4. The first decay constant (t_1 ~0.06) corresponding to smaller areas (≤ 0.5

cm^2) was an order of magnitude lower compared to the second one (t_2 ~0.5) indicating the crucial dependence of the device area on η. The η achieved in devices of areas ≤ 0.5 cm^2 strongly vary; the η dropped off ~50% in the 0.16 – 0.5 cm^2 range.

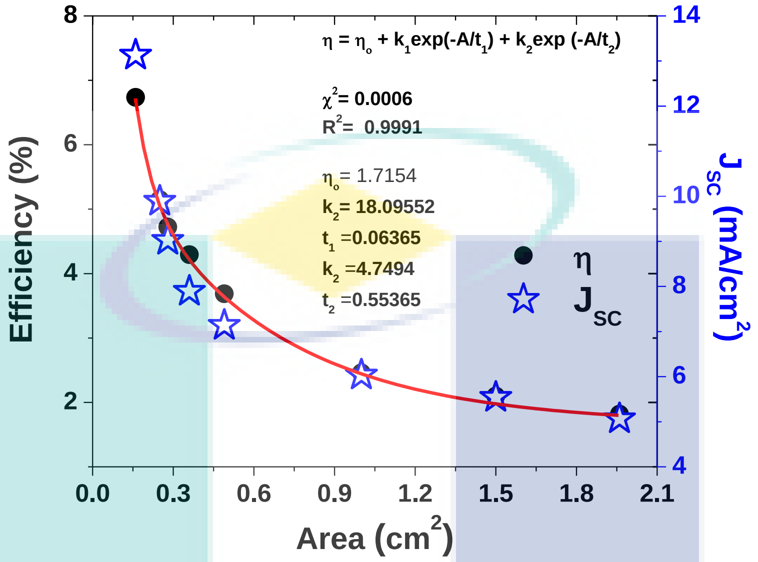

Figure 4.4: Efficiency of cells as a function of electrode area fitted to biexponential decay.

Figure 4.5 shows the variation of J_{SC}, FF, and V_{OC} as a function of device area. The J_{SC} followed similar trend as that of η and contributed the major share to its drop. Given the J_{SC} of DSCs to be $n\mu(x)\nabla F_n$ (Gregg & Hanna, 2003), where n is the electron density, μ(x) is the electron mobility, and ∇F_n is the gradient in the Fermi levels of the materials interface, a decrease in J_{SC} for devices fabricated using similar materials would imply loss of electrons for constant ∇F_n and μ. In other words, increasing the area would lead to longer path length of the electrons which are eventually lost via recombination with the hole-conducting species in the electrolyte as shown schematically in Figure 4.6. The V_{OC} remained at similar values in the area range 0.16 – 0.36 cm^2 after which it gradually decreased. Under steady state of operation, $V_{OC} = \frac{kT}{e} \ln \frac{J_{in}}{n_{cb} k_{rec} [I_3^-]}$, where J_{in} the injected electron density, $k_{rec}[I_3^-]$ is the rate constant of iodide reduction and n_{cb} is the conduction band electron density in the dark. The dye-loading measured in the present experiment from desorption test was constant at ~1.5 × 10^{-7} moles/cm^2; and therefore, a constant J_{in} implies that decrease in V_{OC} with an increase in area result from the change in the rate constant of iodide reduction. Because the R_{SH} and R_S remained at similar values, the FF did not vary appreciably with increase in the area.

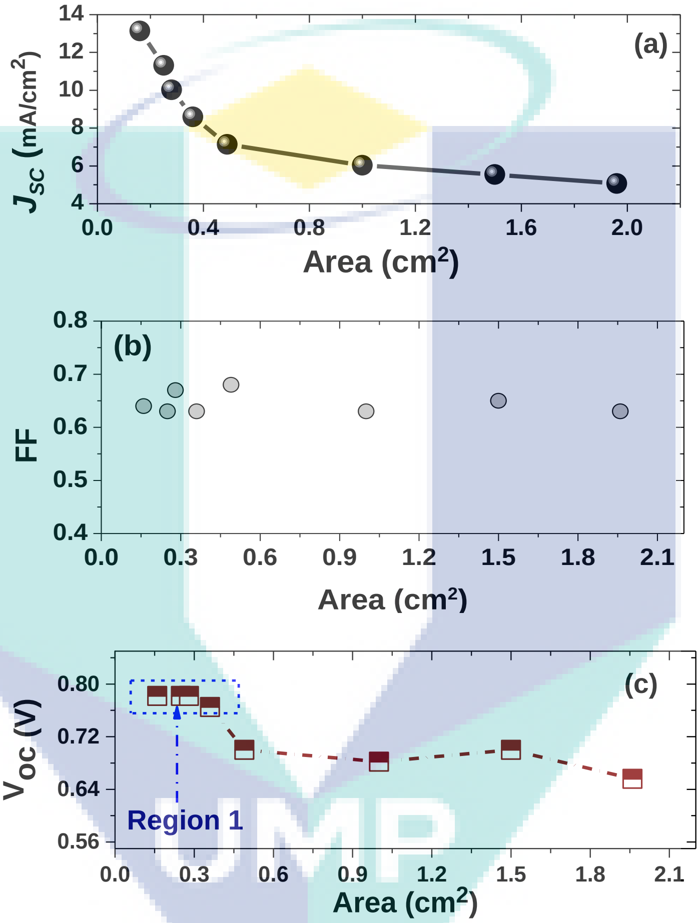

Figure 4.5: (A) J_{SC}, (B) Fill Factor, and (C) V_{OC} as a function of device area; region 1 shows that the value remained constant for area up to ~0.5 cm^2.

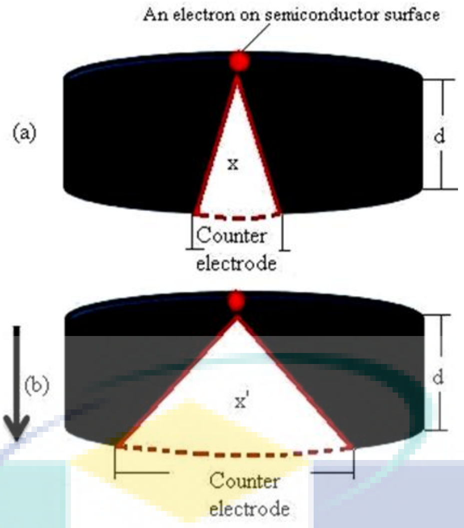

Figure 4.6: Cartoon showing the enhanced diffusion paths as a result of larger electrode areas. The area inside red dashed is the active area for working electrode where the electrons to be collected, while the red dot shows an electron at the surface of semiconductor to be moved by a distance of **x** and **x'**; and "**d**" is the film thickness.

4.4 INVESTIGATIONS OF CHARGE TRANSPORT PARAMETERS

4.4.1 The Variation in Interfacial Resistances

The variation in charge transport with respect to the device area is studied by EIS employing the widely accepted transmission line model (Bisquert et al., 2008). The electrical equivalent of DSCs comprises of resistors and capacitors representing various interfacial and transport processes in the device (Figure 3.6). The EIS spectra is compared with the electrical equivalent to extract the parameters corresponding to the diffusion and recombination processes(Juan Bisquert et al., 2000; Wang Q. et al., 2006). The total impedance of such electrical equivalent is expressed as:

$$Z_{IF} = 2\left(\frac{R_T}{R_{CT}}\right)^{1/2} \frac{1}{C_\mu}\left(i\omega_{CT}\right)^{-\beta} \tag{4.1}$$

where R_T (=r_tL) is the transport resistance, i.e., total resistance offered by the photoelectrode film; R_{CT} (=r_{ct}/L) is the resistance to the charge transfer from the photoelectrode to the electrolyte; C_μ (=$c_\mu L$) is the chemical capacitance; and ω_{CT} is the characteristic frequency at which the charge transfer occurs. The EIS spectrum of DSCs displays three semi circles which are assigned to three processes, viz., (i) resistance to the electron transport (R_T) that occurs at high frequency (> 0.1 kHz); (ii) resistance to the charge recombination(R_{CT}) occurs at intermediate frequencies (0.1kHz <f< 1 Hz); and resistance to ion diffusion occurs at lower frequencies (< 1 Hz) (Figure 4.7a).

Figure 4.7a shows typical EIS spectra of DSCs as a function of device areas for a typical bias voltage ~0.7 V. Both real (Z') and imaginary (Z'') parts of the total impedance marked a surprising decrease in magnitude with increase in area (Figure 4.7b). In addition, the frequencies corresponding to the recombination shifted to higher values with increase in device area showing its crucial dependence on charge transport. The 45^o behavior in the EIS curve, from where the R_T is calculated using the transmission line model (Juan Bisquert, et al., 2000) shifted to lower Z' (Figure 4.7b) showing that the R_T decreased with increase in device area.

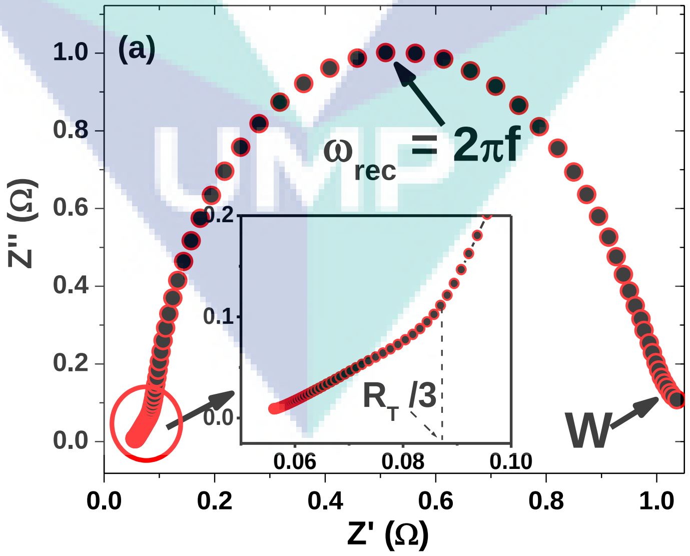

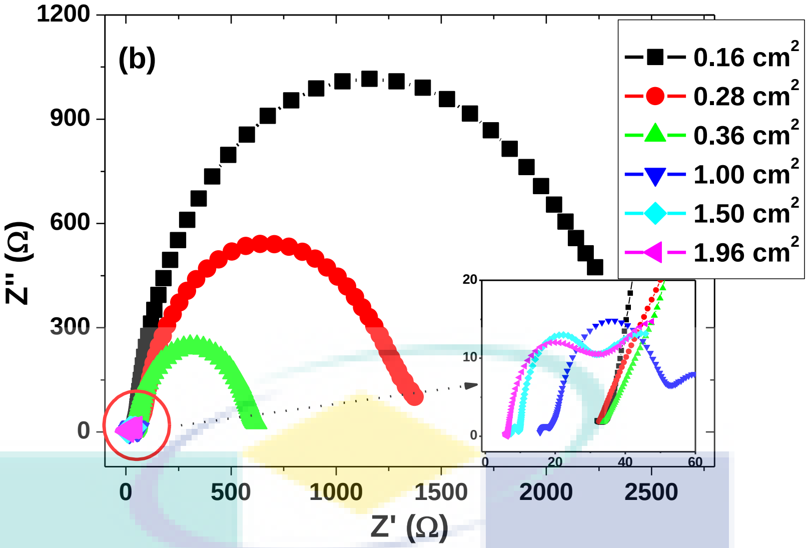

Figure 4.7:(a) EIS spectrum showing the three processes as explained in the text. The "W" stands for resistance to ion diffusion. Refer to the text for details, and (b) Representative EIS spectra as a function of device areas.

Figures 4.8 (a &b) shows the AC resistance calculated directly from the Nyquist plots and the variation of R_T determined by employing the transmission line model, respectively. The high frequency region of the AC resistance, that corresponds to the first semicircle in the Nyquist plots, showed a weak dependence on frequency thereby confirming the electron transport process. i.e., as expected the cells showed decreased R_T as area of the electrode increased (Figure 4.8b). Jennings et al., (2012) recently showed that the R_T nominally increase with increase in thickness of the electrode. In other words, in general R_T increase with increase in the electrode thickness and decrease with increase in its area. Although lower R_T is preferred for fabricating high efficiency DSCs, shifting of frequencies corresponding to R_{CT} have adverse effects as discussed below.The radius of the second semicircle corresponding to the charge transfer process continuously decreased with increasing electrode area thereby shifting the characteristic frequency corresponding to the R_{CT} to higher values.

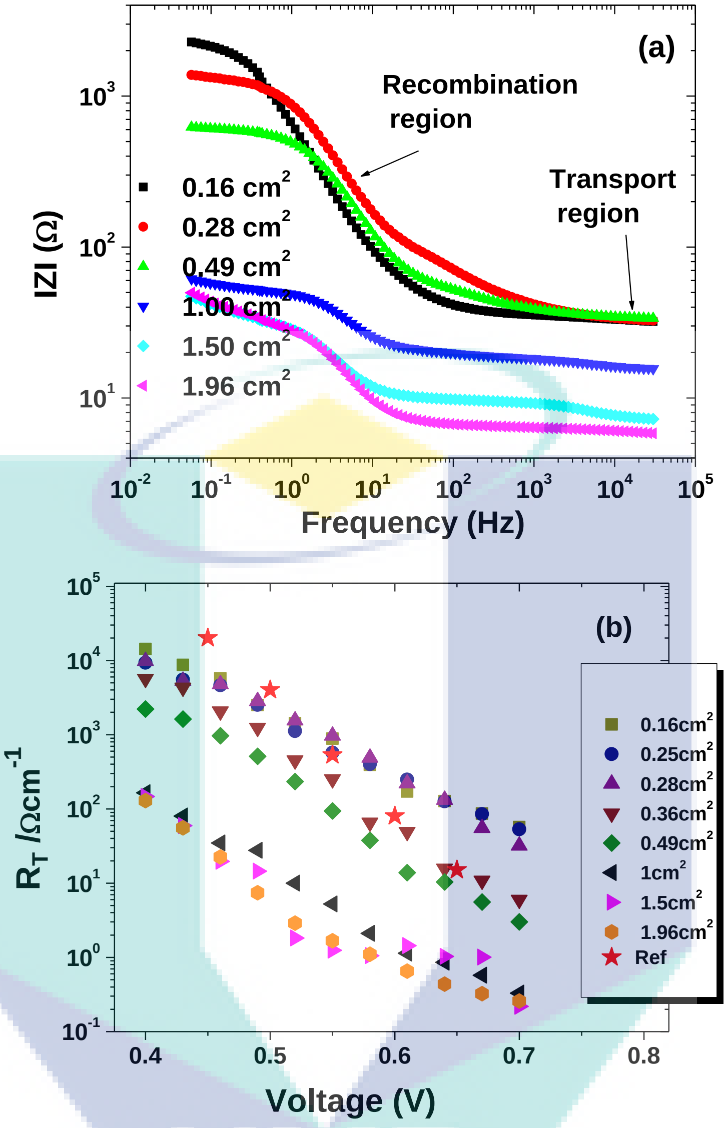

Figure 4.8: (a) AC impedance of the devices as a function of frequency for representative areas, and (b) Electrical transport resistance calculated using the diffusion-recombination model.

4.4.2 The Dependence of Electron Lifetime and Transit Time on Photoanode Area

Figure 4.9 shows the Bode plots calculated from the Nyquist curves, which mark the variation in phase angle of the complex impedance as a function of frequency. The phase angle peak corresponding to the electron diffusion time constant in the TiO_2 film usually appears in the 100 – 1 Hz frequency range, from which the electron lifetime can be calculated using the equation $\tau_n = 1/\omega_{CT}$. Two regions were found in the Bode plots: (i) for areas <0.5 cm^2, the peak frequency (f_C) shifted systematically from 2.01 Hz to 7.54 Hz; and (ii) for areas >0.5 cm^2, the f_C ~5.5 Hz with no systematic shift observed. For areas <0.5 cm^2, the characteristic charge transfer frequency, ω_{CT}, varied from from ~12.01 Hz to ~47.35 Hz. The electron lifetime for the areas in the range 0.16 – 0.49 cm^2 were ~83.3 ms – 21.1 ms. i.e., electrons are short lived as a result of enhanced diffusion path as the electrode area increases. For areas >0.5 cm^2, the lifetime was ~27.9 ms. Thus, if we assume that electrons live above ~21 ms are collected, devices with areas >0.5 cm^2 is expected to show similar η. However, the η continuously decreased with electrode area.

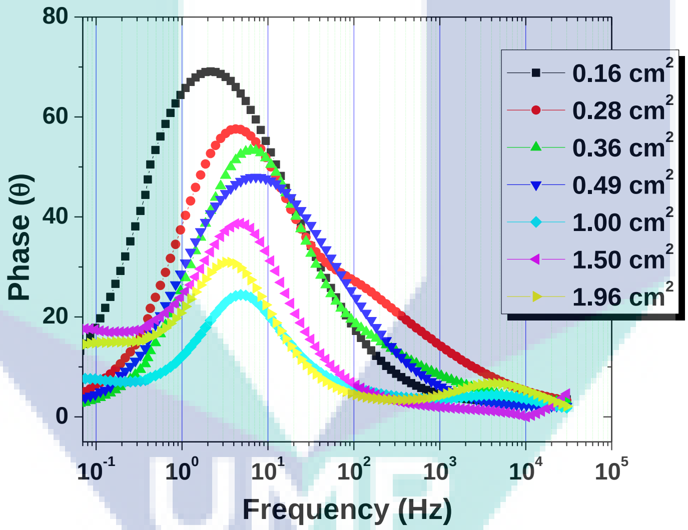

Figure 4.9: Bode plots of the fabricated DSCs as a function of device area.

Electron lifetime (τ_n) and electron transit time (τ_d) are widely employed to estimate collection efficiency of DSCs (Bisquert J., 2008; Martinson et al., 2009). The τ_d is the time required for photogenerated electrons to be collected at working electrode and calculated by the relation $\tau_d = R_T \cdot C_\mu$, where C_μ is the chemical capacitance and obtained through transmission line model as described earlier. This relation is reliable when C_μ is conceived as purely chemical and denotes density of states. A multiple trapping model is often employed in such cases to calculate τ_n and τ_d. Figure 4.10a and b shows τ_d and τ_n of the DSCs and 4.10c depicts a competition between their τ_d and τ_n by correlating them. The smaller area DSCs showed remarkably shorter τ_d compared to the single cell: for example, at 0.7 V, the τ_d is ~4×10^{-5} s in 0.16 cm^2, which systematically increased to ~0.7×10^{-1} s in the largest photoanode (1.96 cm^2). The ~5 times shorter τ_d in the smallest DSC is therefore obvious from shortest diffusion pathways for electron transport; whereas in the largest active area DSCs, the longer path length is evident from their much higher τ_d. In the large area photoanodes, the longer τ_d is a source of their relatively poorer photovoltaic parameters. Equally important is the nominal difference in the electron lifetime (τ_n) of the DSCs as shown in Figure 4.10b.

For a device to show high collection efficiency, the ratio of τ_n / τ_d should be high, i.e., the electrons should be collected much before their lifetime in order to minimize recombination in the device (Fakharuddin A. et al., 2014a). This ratio calculated in the DSCs (Figure 4.10c) is noteworthy. It is several orders of magnitude higher in smallest photoanode DSCs when compared to that of the largest photoactive area DSC. In the DSCs (0.16 – 0.5 cm^2) electrons need much lesser time than their lifetime for collection compared to the devices of larger area (> 0.5 cm^2) which is due to the shorter path length of electrons in the former, eventually reducing possibility of their recombination with holes in electrolyte. This explains why the smaller photoanodes areas have an improved recombination resistance.

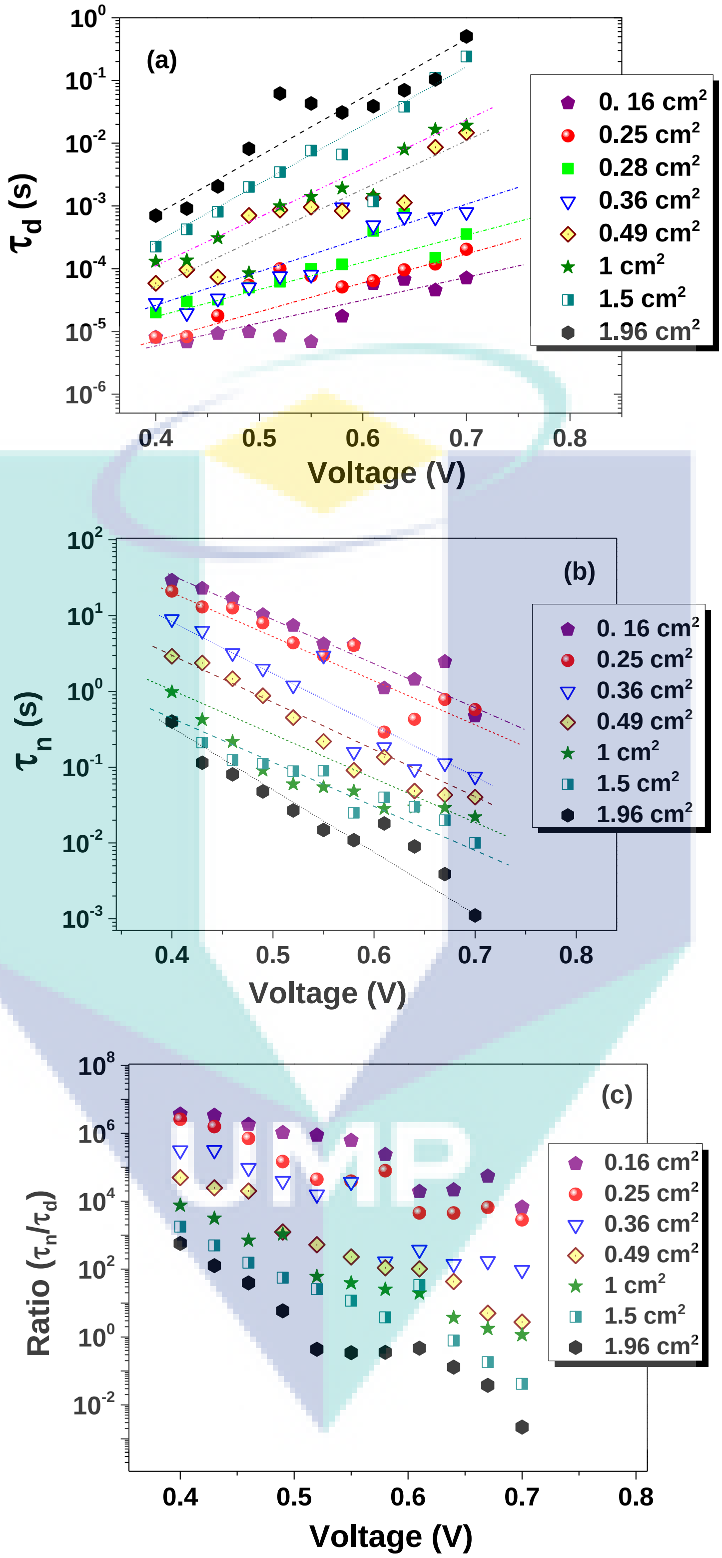

Figure 4.10: (a) Electron transit time, (b) electron lifetime, and (c) a ratio of lifetime to transit time of all the DSCs.

To answer the inconsistency of the electron lifetime time in the above two area ranges, the R_{CT} was extracted from the Nyquist plot using the transmission line model. Figure 4.11a shows the variation of R_{CT} against bias voltage for the entire range of electrode areas developed in this study. Higher R_{CT} was observed for DSCs of lower areas and lowered nominally as the area was increased, thereby explaining the area-dependent efficiency of the cells. i.e., the η of the devices follow the same trend as that of R_{CT}. A step-fall in R_{CT} was observed for areas >0.5 cm^2, which further decreased systematically similar to those of areas <0.5 cm^2. Note that V_{OC} also showed a sharp decrease below this area indicating that a large fraction of electrons are not collected in devices of areas >0.5 cm^2, above which both J_{SC} and η vary drastically.

To study the effect of chemical potential as a function of device area and its relationship on the charge recombination of the DSCs, the chemical capacitance (C_μ) of the electrodes were calculated using the transmission line model and plotted against R_{CT} (J. Bisquert, 2003; Bisquert, 2007b). The C_μ is a measure of change in electron density on a small variation of chemical potential of the cell and has a Fermi level dependence (J. Bisquert, 2003; Bisquert, 2007b).

$$C_\mu = \frac{Ne^2}{k_B T_0} \exp[(E_F - E_o)/k_B T_0] \tag{4.2}$$

Where N is the density of electronic states, e is the elementary charge, E_o is the bottom of the conduction band energy and T_0 is the parameter with temperature units that determine the depth of the distribution of electronic states arise from surface states. The normalized C_μ with respect to device area showed no drastic variation as expected; but a nominal decrease was observed with respect to the device area. The observed lowering in C_μ most likely is of statistical origin; i.e., from the redistribution of localized energy states in the band gap (J. Bisquert, 2003) as a result of increase in the area.

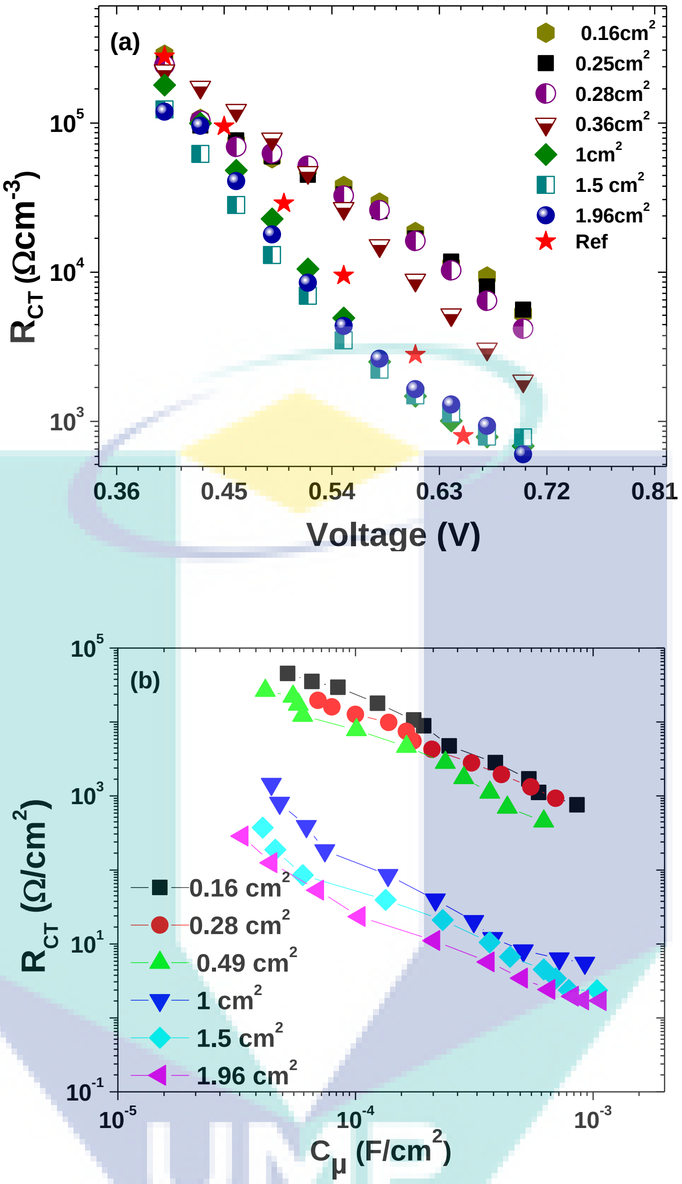

Figure 4.11: (a) Charge recombination resistance calculated from the diffusion – recombination model, and (b) plot of charge recombination resistance as a function of chemical capacitance.

Because E_o and T_0 in the equation (2) are expected to be same for all devices made from same materials and independent of device area, a plot of R_{CT} vs. C_μ should indicate the electron recombination rate constant for constant N and E_F. Figure 4.11b shows the variation of R_{CT} as a function of C_μ normalized with respect to the electrode area, which clearly shows that the R_{CT} decrease with increase in device area. i.e., films of higher area are characterized by an increased rate of electron recombination and eventually result in inferior performance. The increased rate of recombination results from varied electron paths as the electrode area increases. Therefore, diffusion length, defined as the electron path length in electron lifetime, to be redefined taking the area of the electrodes also into account so far. The thickness of the electrode is the only parameter considered so far for defining diffusion length in DSCs.

Therefore, simultaneous lowering of R_{CT} and improved lifetime in devices of area >0.5 cm^2 suggest that electrons survived from recombination only are collected. The collected electrons from areas >0.5 cm^2 having increased lifetime are only a fraction of the total and the remaining were lost due to enhanced diffusion pathways. The collected minor fraction of electrons, which is only ~35% in device of ~ 2 cm^2 area compared to that in the 0.16 cm^2 device, most likely result from the first few monolayers in contact with the working electrode (Figure 4.12). Therefore, the mechanism of area-dependent electron loss is fairly obvious due to enhanced transit length; and thereby lowering of the R_{CT}.

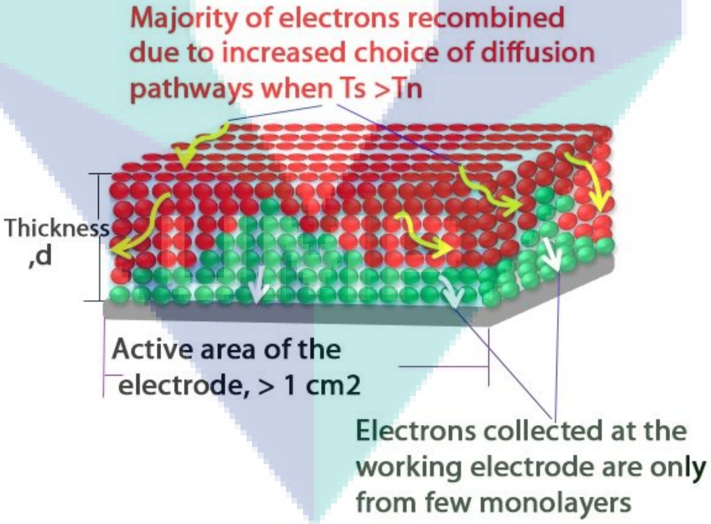

Figure 4.12: Schematic shows three – dimensional view of a large area photoanode. The green coloured monolayers contribute to electrons collection while in the red ones, the electrons are lost via recombination owing to their longer transit time than the lifetime.

Thus, collection efficiency would be compromised in large area DSCs on account of high rate of electron recombination. Besides, thickness of the film does not have much role to play in larger DSCs modules and panels. The generalized equation of state for a dye-sensitized solar cell is be written as, $\eta = f(\alpha, \phi_a, \phi_{INJ}, \eta_C)$, (Kumar et al., 2012) where α is the absorption efficiency, Φ_{in} is the injection efficiency, and η_c is the collection efficiency. For a given dye – photoelectrode materials combination α and Φ_{in} taken constant values; therefore, optimizing η_c is the key to develop highly efficient commercial modules. We note that the present study is limited to conventional P25 particles. Although many materials and morphologies have been developed recently that favours enhanced electron mobility and diffusivity, (Archana, Jose, Yusoff, & Ramakrishna, 2011; Naveen Kumar et al., 2012) choice of highly efficient DSCs has always been the P25 particles owing to its ready availability and high specific surface area.

4.5 CONCLUSIONS

The photovoltaic performance of dye-sensitized solar cells strongly depends on the photoanode area; it showed a biexponential drop when the photoelectrode area was increased from 0.16 – 1.96 cm^2. The current-voltage and electrochemical impedance spectroscopy revealed the source of this drops, i.e., the increased transit length in larger photoanodes offers greater diffusion pathways to electrons transport resulting in their increased recombination with hole species. The electron transit time increased several folds in 1.96 cm^2 showing that for a given electron lifetime, the photogenerated electrons are only collected from a film volume nearer to the working electrode. Thus photoanode area is to be considered along with the thickness when high efficiency devices with larger area are targeted using the commercially available TiO_2 nanoparticles.

CHAPTER 5

DEVICE DESIGNS WITH ENHANCED CHARGE COLLECTION

5.1 Introduction

The previous chapter unambiguously established the crucial dependence of photoelectrode area on charge collection in DSCs. Based on those insights, this chapter propose and validate alternate designs for efficient charge collection in large area devices (1 cm^2 – 100 cm^2). The difference in their designs and current-voltage characteristics are studied and reported.

5.2 Current-Voltage Investigation of DSCs (~1 cm^2)

While we have noticed the area dependant photovoltaic performance of DSCs, improved photovoltaic performance is possible by geometrically reducing the size of individual cells and then stacking them on a single substrate to fabricate a dye-sensitized solar module (DSM). We have systematically upscaled smaller area DSCs based on the insights gained in chapter 4. The first set of devices fabricated towards this end consisted of active area ~ 1 cm^2 where we impose constraints in electron diffusion by applying geometrical restriction to the photoelectrode active area of 1 cm^2 (Figure 5.1). The active area is systematically split into one, two, four, and eight individual cells of similar size and area labelled as DSC$_1$, DSC$_2$, DSC$_4$, and DSC$_8$ respectively. The interspacing between neighbouring cells is kept constant (~0.3 mm). As there is no sealing between individual cells, such low interspacing can minimize the inactive area losses.

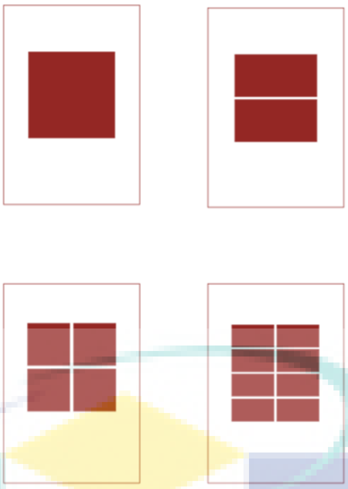

Figure 5.1: Patterns of various DSC designs of area ~1 cm^2.

The current voltage performance of the devices fabricated based on the new design is shown in Figure 5.2 and the photovoltaic parameters are listed in the Table 5.1. The DSC$_1$ showed the lowest photovoltaic parameters (η ~3.1%, V_{OC} ~0.68 V, J_{SC} ~7.33 mA/cm^2, and FF ~0.62). The performance increased systematically in the DSCs with increasing number of split cells on a single substrate and the highest performance the DSC$_8$ showed the highest η~6.33% (V_{OC} ~0.78 V, J_{SC} ~12.33 mA/cm^2, and FF ~0.66). Although the FF is slightly lower than that of DSC$_4$ (0.69), an overall increment in FF is observed with increasing number of split photoanode patches. The active area efficiency in DSC$_8$ is ~100% higher than that DSC$_1$. Similarly, the η of the former calculated with respect to aperture area is also 80% higher than of the latter. As shown in Table 5.1 major contribution to this increase arises from the greater current collection; the J_{SC} increase ~70% from DSC$_1$ to DSC$_8$. A 100 mV enhanced V_{OC} and a notable improvement in FF is also observed in split photoanode designs.

The increment in photovoltaic parameters in split cells directly reflects the improved electronic properties of those devices. FF is a measure of the recombination in the devices as it depends upon the shunt (R_{SH}) and series (R_S) resistances in the devices. The increased FF in split photoanodes (~0.62 in DSC$_1$ to ~0.69 in split DSCs) demonstrated the beneficial effects of confining the electron movement by appropriate device designs. Similarly, increment in R_{SH} (506 Ω for DSC_1 and 1126 for DSC_8) upon splitting the cells further affirms a reduction in internal recombination.

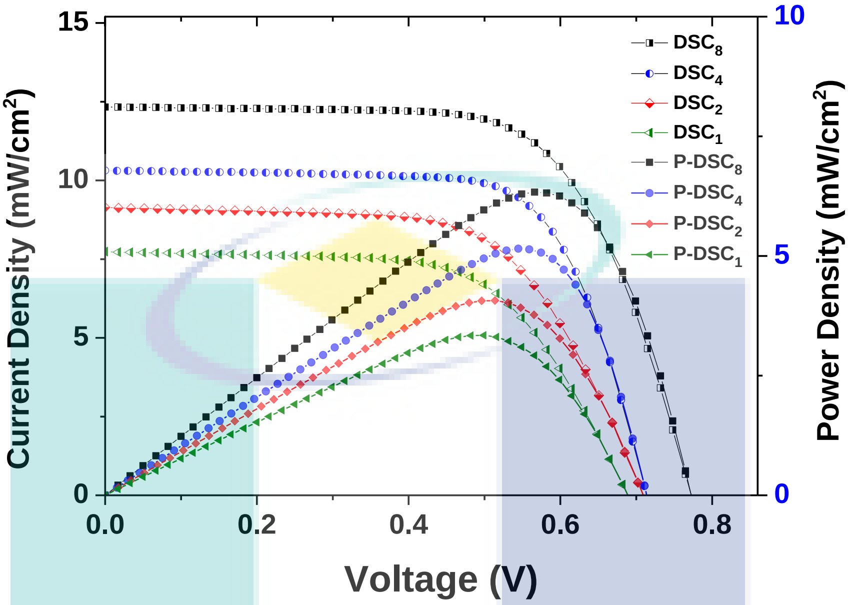

Figure 5.2: Current –voltage characteristic curves of various DSCs of active area ~1 cm^2 at 1 sun conditions. The subscripts in DSC_1, DSC_2, DSC_4, and DSC_8 represent the number of photoanode patches, respectively.

On splitting the area of the single cell from ~1 cm^2 in DSC_1 to ~0.12 cm^2 in DSC_8, the η increased by a factor of ~2 and the J_{SC} by ~70%. The increase in J_{SC} followed nearly similar trend as that of η and contributed the major share to its rise. Given the J_{SC} of DSCs to be $n\mu(x)\nabla F_n$,(Gregg & Hanna, 2003), where n is the electron density, μ(x) is the electron mobility, and ∇F_n is the gradient in the Fermi levels of the materials interface, a decrease in J_{SC} for devices fabricated using similar materials would involve loss of electrons for constant ∇F_n and μ. This is due to the fact that in larger photoanode areas the photogenerated electrons experiences longer path length and are eventually lost via recombination with the hole-conducting species in the electrolyte. This can also be further explained by relatively smaller V_{OC} in DSCs of larger photoanode area.

Table 5.1: The detailed photovoltaic performance of the various DSCs (Figure 5.1). The η and η′ are the efficiencies based on their active and aperture areas, respectively.

DSM	Active area (cm^2)	Aperture area (cm^2)	J_{SC} (mA/cm^2)	V_{OC} (V)	FF	η (%)	η′ (%)
DSC_1	1	1	7.33	0.682	0.62	3.11	3.34
DSC_2	1	1.03	9.14	0.705	0.63	4.06	3.94
DSC_4	1	1.06	10.31	0.712	0.69	5.13	4.84
DSC_8	1	1.13	12.33	0.782	0.66	6.33	5.60

The V_{OC} increased systematically upon splitting the photoanode area. Under steady state of operation, $V_{OC} = \frac{kT}{e} \ln \frac{J_{in}}{n_{cb} k_{rec} [I_3^-]}$, (Bisquert J. 2002) where J_{in} the injected electron density, $k_{rec}[I_3^-]$ is the rate constant of iodide reduction and n_{cb} is the conduction band electron density in the dark. The DSCs are made under similar experimental conditions employing similar materials and therefore any contribution arising from the material properties can be ruled out. The dye-loading measured in the present experiment from desorption test was constant at ~2 × 10^{-7} moles/cm^2; and therefore, a constant J_{in} implies that decrease in V_{OC} with an increase in area result from the change in the rate constant of iodide reduction. This can be further verified by the increased FF in split photoelectrodes (Qi & Wang, 2013). It is important to note that there is no intermediate sealing between neighboring cells; and therefore, the need of a blocking layer is crucial in such designs to prevent the electrolyte contact with FTO.

5.3 Photovoltaic performance of DSMs of area ~25 cm^2

Up-scaling of DSMs up to 25cm^2 is attempted after the encouraging results of devices of 1cm^2. In this experimental phase, we also varied the interspacing to realize any possible effects on photovoltaic performance. The various attempted designs are shown in Figure 5.3. The size of the individual cell is reduced systematically from 0.25 cm^2 to 0.015 cm^2. The labels assigned to each device represent its size and also the interspacing, i.e., in DSC_{5-1}, the first number (5 in this typical example) represents the dimensions (length and width) of the individual cell and the second number after the punctuation mark (-) corresponds to the interspacing. The active and aperture areas of these devices are listed in Table 5.2. It is evident that upon reducing the individual cell size, the active area of the DSM reduces due to increased number of interspacing. In such conditions the overall performance of the DSM with respect to its aperture area will be significantly lower due to the increased ratio of inactive area. For an efficient module, a balance between areas loses upon reducing the individual cell size and the performance loss due to increasing cell size has to be considered.

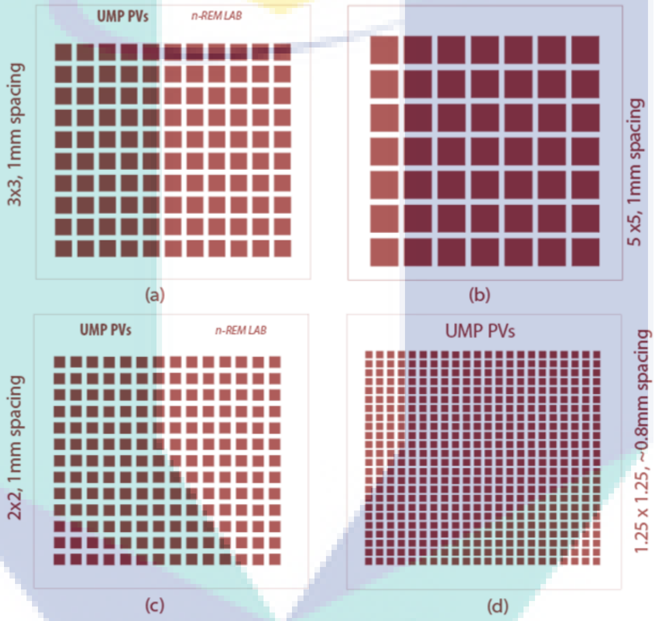

Figure 5.3: Patterns of various DSC designs on a substrate area ~25 cm^2.

Figure 5.4 shows the photocurrent density– photovoltage characteristics of the best performing devices; the details of their PV parameters are listed in Table 5.2. The η with respect to the active areas of the DSM$_{5\text{-}1}$, DSM$_{3\text{-}1}$, DSM$_{2\text{-}1}$, DSM$_{1.25\text{-}0.8}$ fabricated using commercial materials (TiO$_2$, dye and electrolytes) was 1.03%, 1.47%, 2.47%, and 1.73%, respectively. The variation of η of the devices mainly arises from their significantly different J_{SC} which follows the same trend as that of η. As the devices are made of similar materials and of similar photoanode thickness, the enhancement in PV parameters is attributed due to improved charge transport properties in DSM$_{3\text{-}1}$, DSM$_{2\text{-}1}$, and DSM$_{1.25-0.8}$ compared to that of DSM$_{5-1}$. As the active area of the DSM$_{5-1}$ is the highest, one may expect the highest photocurrent in it; however, the I$_{SC}$ in DSM$_{5-1}$ 17%, 45%, and 51% lower than those of DSM3$_{-1}$, DSM$_{2-1}$, and DSM$_{1.25-0.8}$, respectively. The comparison of photocurrent for a unit area (J$_{SC}$, Table 5.2) further confirms enhanced charge collection in DSMs when the photoanode stacks are made smaller. A notable drop in J$_{SC}$ is however observed in DSM$_{1.25-0.8}$. Despite the smallest active area, the DSM$_{2-1}$ resulted in the highest output power (17.9 mW, Figure 5.4b).

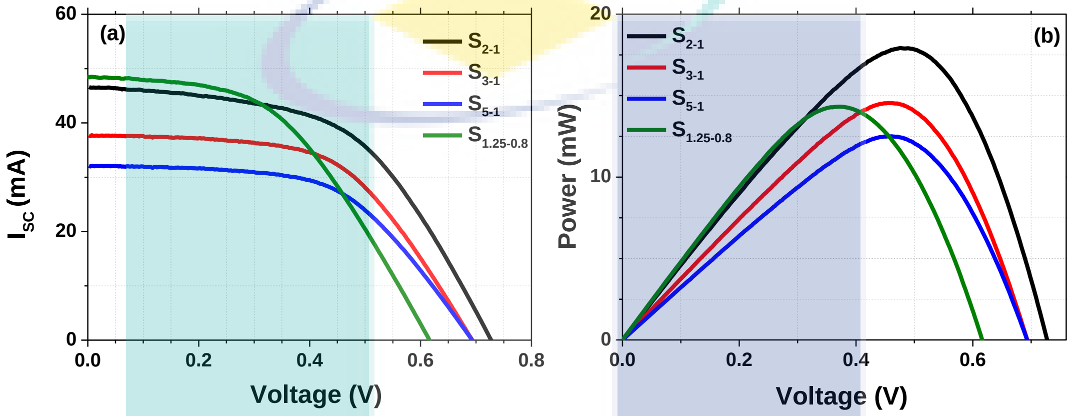

Figure 5.4: Current –voltage characteristic curves of various DSMs built on a substrate area ~25 cm^2 and measured at 1 sun conditions, and (b) power output of the same modules.

The V$_{OC}$ showed an overall increment from DSM$_{5-1}$ to DSM$_{2-1}$and then decreased in DSM$_{1.25-0.8}$. Recall the drop in J$_{SC}$ in the same device. The FF in DSM$_{1.25-0.8}$ is also the lowest. Such trends suggest that an optimization is required for reducing the individual cell size beyond which the betterment in PV parameters is limited. This is also important as the ratio of inactive area will increase upon reducing the individual cell size. Among the first three DSMs (DSM$_{5-1}$, DSM$_{3-1}$, DSM$_{2-1}$) where the interspacing is similar (~0.1 cm), the highest inactive area loss (~70%) is observed in DSM$_{2-1}$ which was ~60% and 51% in DSM$_{5-1}$ and DSM$_{3-1}$, respectively. The performance can be further increased by optimizing the interspacing and thereby increasing the active area.

Table 5.2: The PV parameters of various DSMs shown in Figure 5.3. The η and η' are the efficiencies based on their active and aperture areas, respectively.

DSM	Active area (cm^2)	Aperture area (cm^2)	I_{SC} (cm^2)	J_{SC} (mA/cm^2)	V_{OC} (V)	FF	η (%)	η' (%)	Power output (mW)
$DSC_{5\text{-}1}$	12.25	16.80	32.11	2.62	0.693	0.57	1.03	0.75	12.5
$DSC_{3\text{-}1}$	9.9	16.77	37.74	3.81	0.693	0.56	1.47	0.87	14.5
$DSC_{2\text{-}1}$	7.28	15.58	46.61	6.4	0.727	0.53	2.47	1.15	17.9
$DSC_{1.25\text{-}0.8}$	8.25	16.45	48.47	5.87	0.616	0.48	1.73	0.87	14.4

To validate the contributions from charge transport on the PV parameters of the new type of electrodes, we have conducted EIS measurements of the best performing device with minimum active area of the individual cell stack ($DSM_{2\text{-}1}$) and the DSM with highest active area of unit cell ($DSM_{5\text{-}1}$). Figure 5.5 (a – c) show the Nyquist and Bode plots of the two devices. The radius of the semicircle at mid frequencies which is a measure of R_{CT} showed higher values for $DSM_{2\text{-}1}$ which may be attributed due to the shorter transition path for photogenerated electron in it compared to the $DSM_{5\text{-}1}$. Higher series resitance (R_S) is observed in $DSM_{2\text{-}1}$ which may be originated from the increased number of contacts of TiO_2 with FTO.

As the frequency dependence of complex impedance and the phase angle is not explicitly displayed in the Nyquist plot, their Bode plots are shown in Figure 5.4 (b&c). The characteristic frequency at which the recombination occurs (ω_{RT}) shifts to lower values in $DSM_{2\text{-}1}$ due improved charge transport properties. The phase angle peak corresponding to the electron diffusion time constant in the TiO_2 film usually appears in the 100 – 1 Hz frequency range, from which the electron lifetime (τ_n) can be calculated using the equation $\tau_n = 1/\omega_{CT}$. i.e., the peak frequency shifts to lower values for higher τ_n. We observed ~8 times higher electron lifetime in $DSM_{2\text{-}1}$ which confirms the improved charge transport as a source of enhancement in PV paramters in $DSM_{2\text{-}1}$. One would observe that electrons lived much longer in $DSM_{2\text{-}1}$ than the $DSM_{5\text{-}1}$.

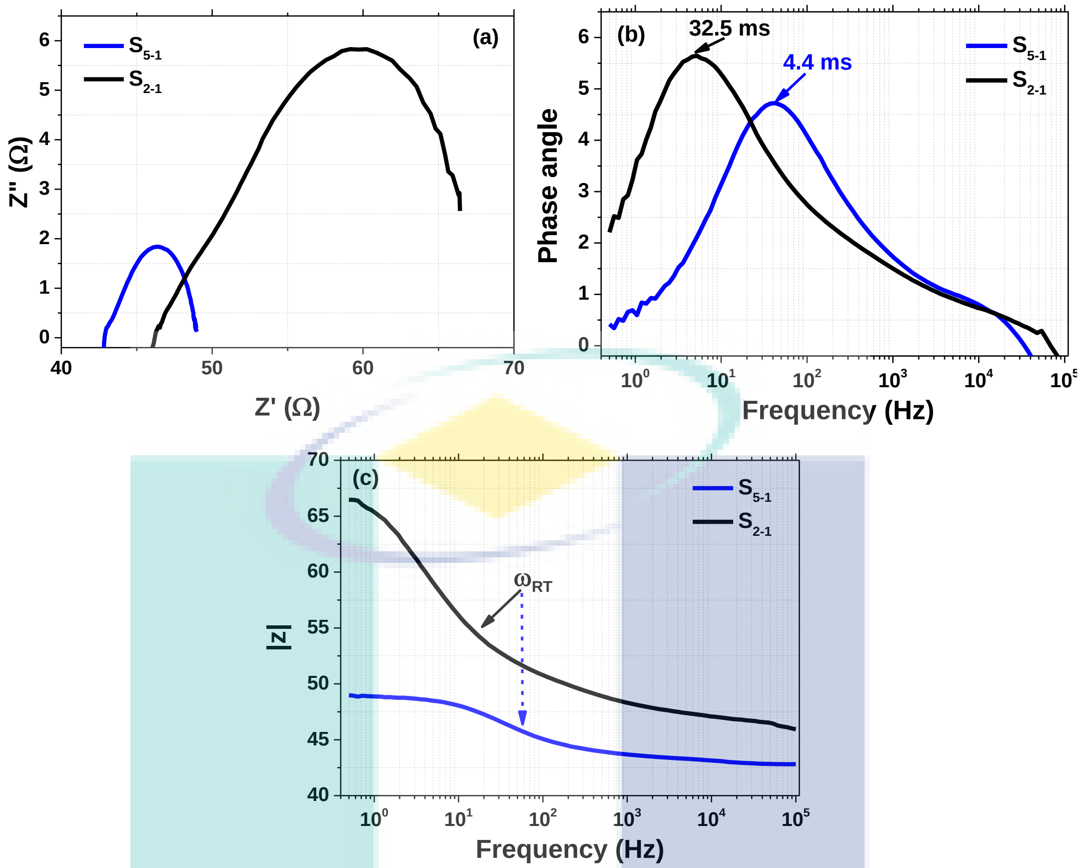

Figure 5.5: EIS spectra of the DSM$_{2\text{-}1}$ and DSM5$_{\text{-}1}$ showing (a) Nyquist, (b) Bode phase and (c) Bode modulus plots. The impedance spectra are recorded in dark and at 0.7 V.

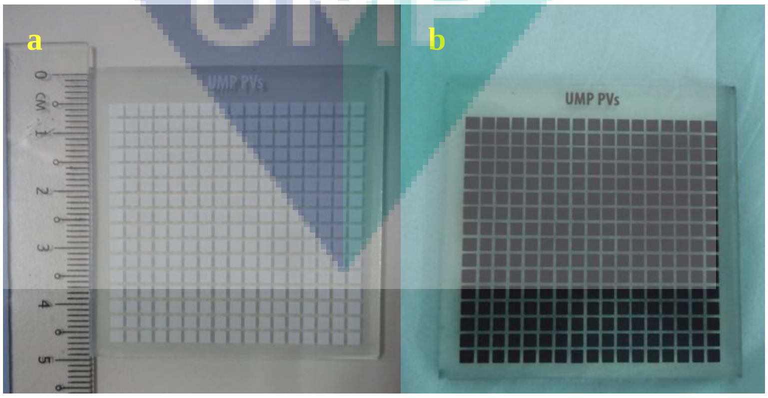

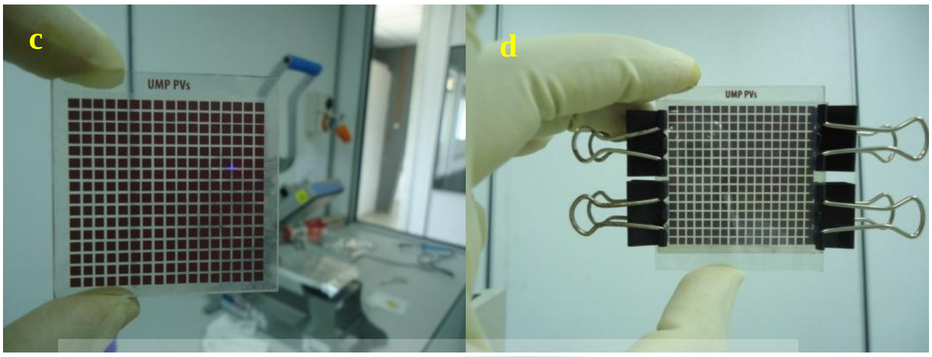

Figure 5.6: Photographs of DSM_{3-1} (area ~25 cm^2) during various fabrication steps; (a) is a screen printed working electrode (WE) annealed at 450 ^oC, (b) & (c) are the same WE after dye anchoring, and (d) is partially completed device where WE is assembled with CE prior to the electrolyte filling.

Important is to note that there is no separation between neighbouring cells and therefore the mass transfer of the electrolyte from one cell to another is anticipated. Such process is called electrophoresis and it degrades the performance of the device over time due to imbalance caused between redox species of the electrolyte. The devices made without a complete separation of neighbouring cells render very low performance. No such device design is attempted so far for *l*-DSC; however, Biancardo et al., tested *s*-DSMs with no isolation of the neghbouring cells. They employed poly-methyl-meta-acrylate (PMMA) and propylene carbonate to make a gel of the conventional iodide/triiodide electrolyte. Their series connected DSMs of 100 cm^2 resulted in η ~0.8% (V_{OC} ~ 5.16 V, I_{SC} ~37 mA, FF ~0.47). However, the performance of such DSMs dropped 60% in ~1000 h. Our DSM_{2-1} yielded 3 time higher photocurrent then their DSMs. An improved performance is also expected in *s*-DSMs employing split photoanode architectures as mass transfer of redox species is not an issue in solid-state hole conducting media.

5.4 Photovoltaic performance of DSMs of area ~100 cm^2

Finally, we attempted up-scaling of DSCs to an area ~100 cm^2. DSMs consisted of multiple arrays of active area 0.5 × 0.5 cm^2 with an interspacing of 0.2 cm (Figure

5.7). Although such high interspacing will increase the inactive area of the device, it was initially created to isolate the neighbouring cells with a sealant. Our attempts revealed that sealing of such design architectures is extremely complex and it also the fabrication such DSMs as it requires intensive drilling at counter electrode for electrolyte filling in each cell. The DSMs were tested in outdoor conditions as the module size is larger than the maximum spot size of our solar simulator (a circle with diameter ~6 cm).

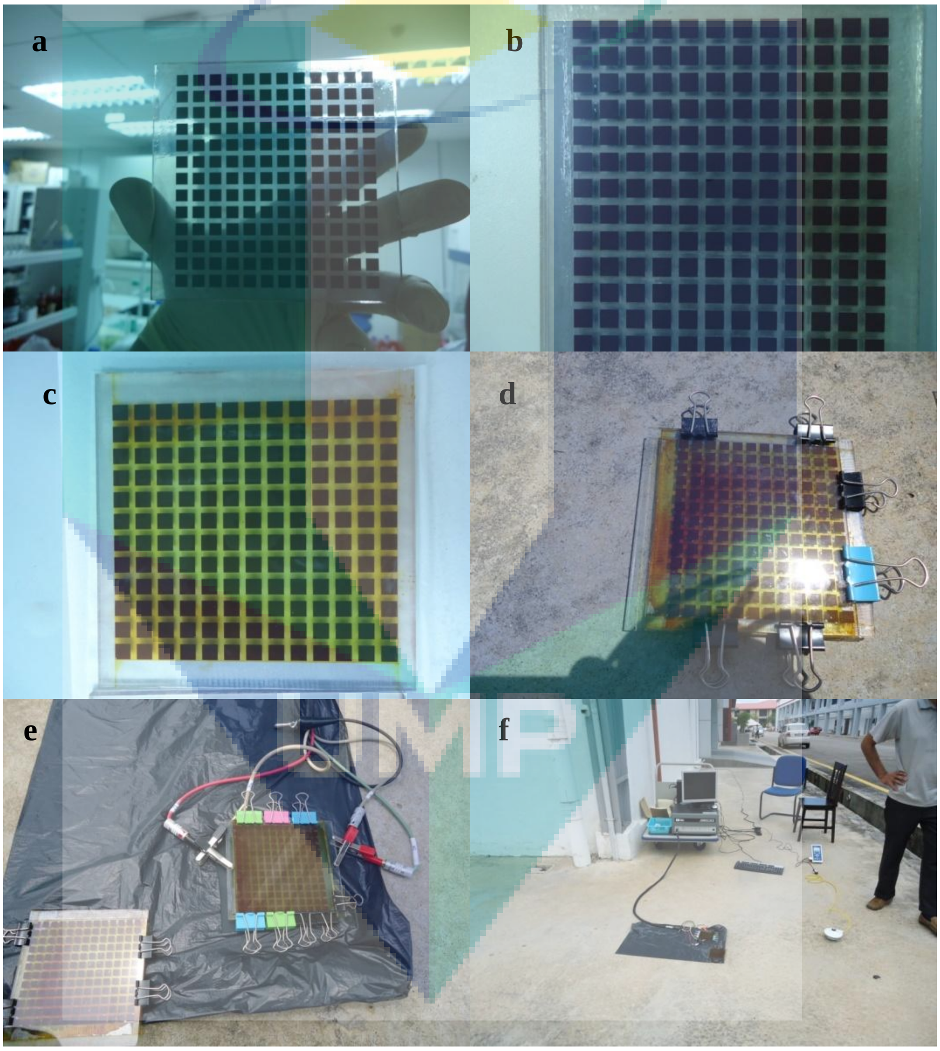

Figure 5.7: Photographs of DSM made on a substrate area ~100 cm^2. The various photographs show the gradual assembling and testing process of DSM. Figure (e & f) shows the outdoor testing setup of such modules.

Table 5.3: The photovoltaic performance of DSM$_{10\times10}$ at ~0.35sun. The η and η′ are the efficiencies based on their active and aperture areas, respectively.

DSM	Active area (cm^2)	Aperture area (cm^2)	I$_{SC}$ (cm^2)	J$_{SC}$ (mA/cm^2)	V$_{OC}$ (V)	FF	η (%)	η ′ (%)	Power output (mW)
DSM$_{10\times10}$	39	73	89.7*	2.31	0.616	0.47	1.91	1.02	26.3*

*measured at ~0.35 sun.

The current voltage performance of DSM$_{10\times10}$ is shown in Figure 5.8. It demonstrated ~2%η (V$_{OC}$ ~0.616 V, I$_{SC}$ ~90 mA, and FF ~0.47). The output power of our module was 26.3 mW at ~0.35 sun. Although the η with respect to its aperture area (1.02%) is almost half of its active area, it can be further improved by reducing the interspacing. The low PV performance of our modules is due to the high R$_S$ (50 – 60 Ω/□) which also affected its FF (0.47). This is due to the fact that the modules do not employ a silver finger for current collection which normally yields a high FF in DSMs (Table 2.2, Appendix II).

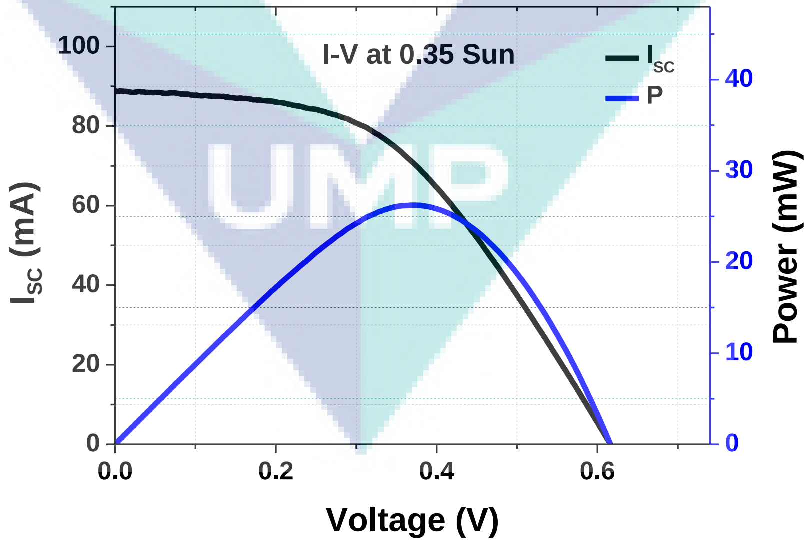

Figure 5.8: I-V characteristic and power output curve of DSM$_{10\times10}$ and measured at ~0.35 sun.

5.5 CONCLUSIONS

In conclusion, we have up-scaled dye-sensitized solar cell to larger areas (~1, ~25, and ~100 cm^2) with novel designs for improved charge collection. Splitting of photoanode area to restrict electron diffusion pathways successfully resulted in improved charge transport parameters and consequently reflected in their PV parameters. Although, the DSMs showed lower performance than the state-of-the-art DSMs, further improvement is possible by optimizing the device geometry and the interspacing and also by transferring them into a solid-state device.

CHAPTER 6

CHARGE TRANSPORT IN SPLIT PHOTOANODE DESIGN

6.1 INTRODUCTION

This chapter aims to deeply investigate charge transport properties in split photoanode designs. At first, it explains the split photoanode designs and their geometry and subsequently compares the electrical performance of the split photoanodes with conventional ones. Finally, detailed EIS investigations are carried out to understand the relationship between the PV performance in such designs and the charge transport parameters such as electron transit time, charge recombination, diffusion length, and electron collection efficiency.

6.2 THE SPLIT PHOTOANODES IN DSCs

The split photoanodes were fabricated by dividing a given photoelectrode film volume into tinier multiple patches with an inter-patch spacing ~200 – 300 μm such that the electron movement is limited within the tiny patches by the frequent gaps within the electrode film (Figure 6.1). The various photovoltaic parameters were calculated as follows. The η was calculated for two typical device dimensions, viz. active and active areas. The active area is defined as the area covered by TiO_2 strip only, whereas the aperture area includes active area and the area of the inter-electrode spacing (Figure 6.2). The active area of the electrodes were ~28 mm^2; the total areas of the three DSCs were 28, 33.44 and 34.96 mm^2 and the aperture areas were 28, 28.8 and 30.28 mm^2 is for the S1, S2 and S3,respectively.

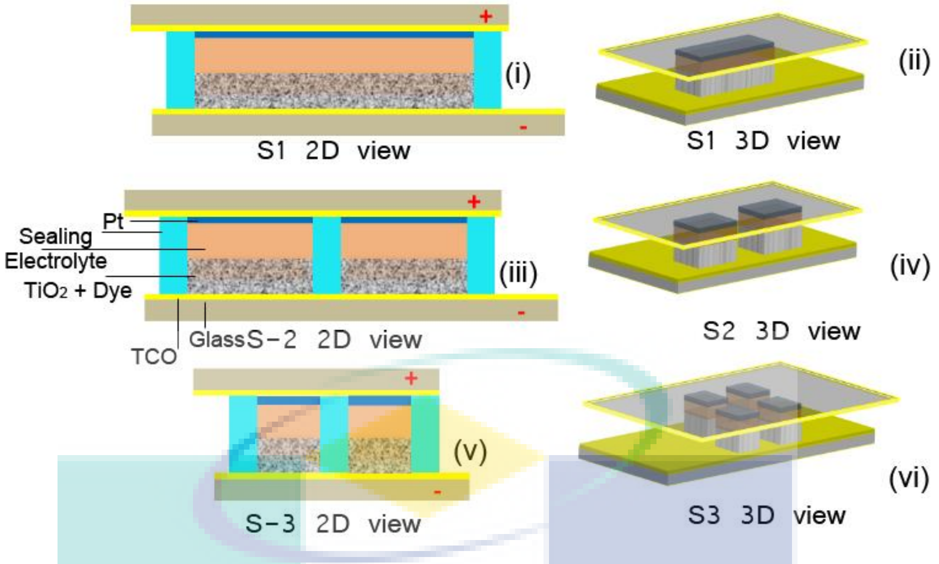

Figure 6.1: Schematics showing the split dye-sensitized solar cell designs. The individual stacks are drawn free of scale. The sealing is not shown in 3D views for clarity purpose.

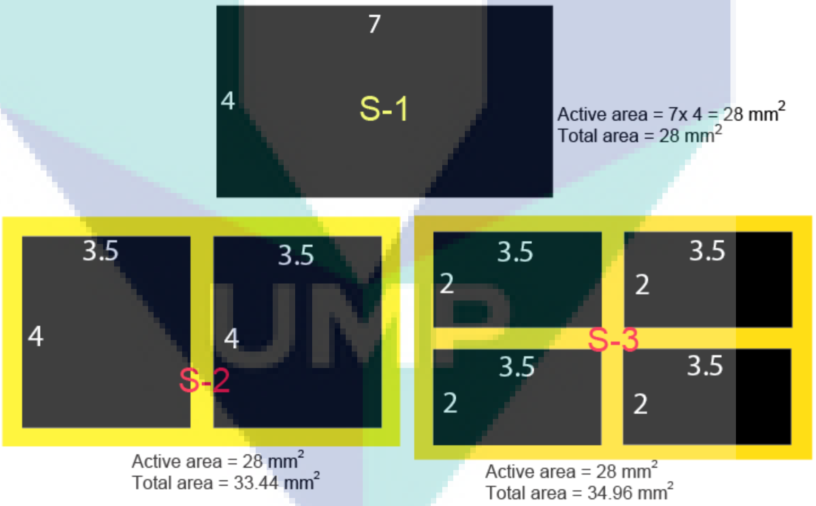

Figure 6.2: Schematics to elaborate active, aperture area, and total area used to calculate the respective η. The yellow shade for S-2 and S-3 is drawn free of scale for elaboration purpose only.

6.3 CURRENT – VOLTAGE CHARACTERIZATIONS

Photocurrent measurements of the three sets of devices were carried out at AM 1.5G conditions. Figure 6.3 shows representative *I—V* curves of the devices (detail is given in Table 6.1); the photovoltaic parameters of the devices are summarized in Figure 6.4 (a—d). Obviously, the η increased from devices S1 to S3. Major contribution to the increase in η resulted from J_{SC} which increased from 11 mA/cm^2 to 17 mA/cm^2 when the area of the individual stacks is reduced from 28 mm^2 to 7 mm^2. i.e., the devices fabricated with a combination of a multiple electrode arrays (S2&S3, which have no additional connection than the already present connection via FTO) showed higher photocurrent than that is achieved by a single electrode film of similar area (S1). A wiring scheme of the individual stacks is given in Figure 6.1.

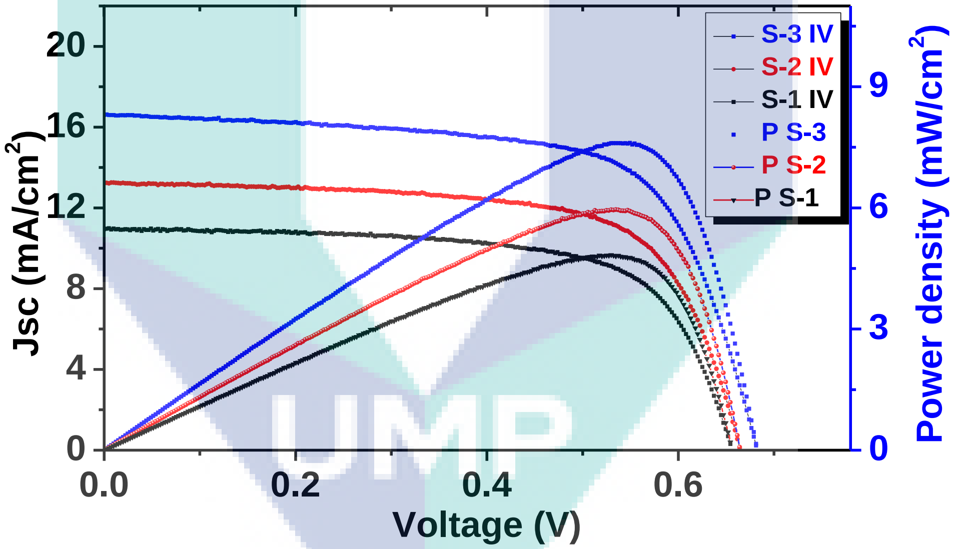

Figure 6.3: I-V curves of the three types of DSCs under AM 1.5, 1 sun illumination conditions.

The photocurrent increased 21% in S2 and 52% in S3 compared to S1 thereby clearly establishing the beneficial effects when the diffusive path is restricted by appropriate device designs. Choice of the electron diffusion paths in smaller area electrode films (S2 & S3) are considerably lower than that in the larger area film of same active area (S1). As more electrons are collected by restricting the diffusion paths, V_{OC} showed nominal enhancements. The *FF* (calculated via relation FF = $(I_{MP}.V_{MP})/(I_{SC}.V_{OC})$) for all the devices remained practically same. The R_S and the shunt resistance R_{SH} of the devices are calculated using slope method and are 0.61 Ω, 0.47 Ω, and 0.4 Ω and 610 Ω , 775Ω and 980 Ω for S1, S2 and S3, respectively, which shows that the devices are of good quality (Fabregat-Santiago, et al, 2005).

Table 6.1: A comparison of photovoltaic parameters of the three DSCs. The parameters are calculated by considering the active area, and aperture area respectively.

Device design	Dimensions & active area (cm^2)	I_{SC} (mA)	J_{SC} (mA/cm^2)	V_{OC} (V)	FF	η_1 % (active area)	η_2 % (aperture area)
Single (S1)	~0.28	3.11	10.67	0.66	0.701	5.01	5.01
Split (S2)	~0.14 × 2 = 0.28	3.70	13.21	0.67	0.678	6.06	5.87
Split (S3)	~0.07 × 4 = 0.28	4.65	16.21	0.67	0.644	7.32	6.88

The PCE for DSCs can be expressed as a general expression, i.e. PCE=$f(\alpha,\phi_{in},\eta_c)$ where α is the absorption coefficient, ϕ_{in} is the injection efficiency, and η_c is the charge collection efficiency at working electrode.(Michael Grätzel, 2009; Kumar, et al., 2012) In all three fabricated DSCs, the α and ϕ_{in} are similar, therefore, the source of this increase in J_{SC} is fairly obvious as the enhancement in η_c resulted as a consequence of reducing the choice of diffusive paths.

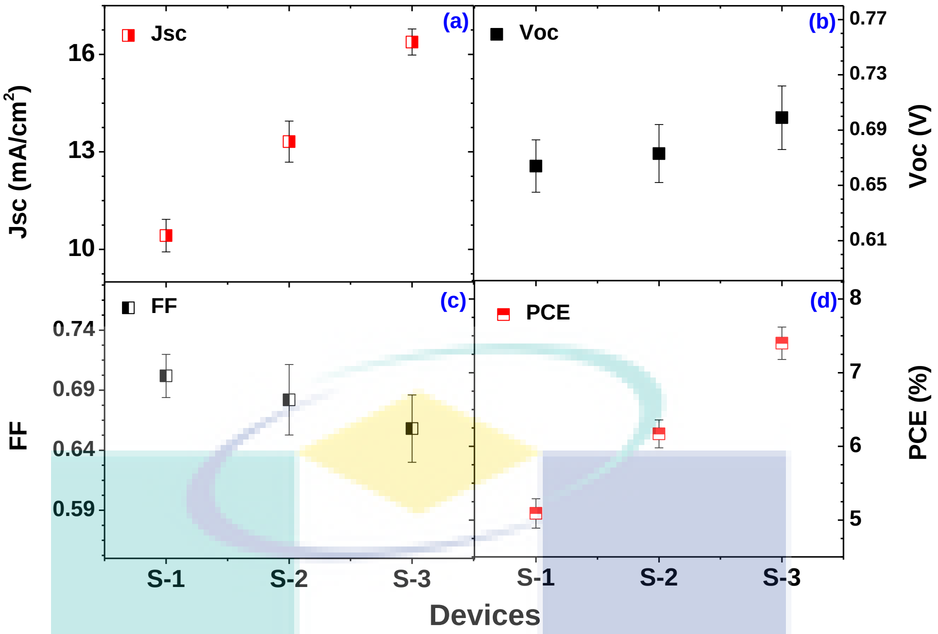

Figure 6.4: A comparison of photovoltaic parameters of the DSCs. The figures (a), (b), (c) and (d) show the J_{SC}, V_{OC}, FF, and η for at least four cells of each type, respectively.

6.4 EIS ANALYSIS OF THE SPLIT PHOTOANODES

6.4.1 Charge Transport in Split Photoanodes

The EIS spectra of the three-sets of devices were analyzed employing a well-accepted transmission line (TL) model to understand the origin of observed variation in their PV parameters (Bisquert, 2002; Kern, Sastrawan, Ferber, Stangl, & Luther, 2002).The charge transport parameters affecting the efficiency of DSCs are (i) electron transport resistance (R_T), electron transfer resistance (R_{CT}), electron transport time (τ_d), and electron lifetime (τ_n) (J. Bisquert, 2008). The variation in charge transport in each design is studied by electrochemical impedance spectroscopy (EIS) employing the TL model (J. Bisquert et al., 2000). The electrical equivalent of DSCs considers the interfacial impedance (Z_{IF}) at a semiconductor – electrolyte interface that comprises of resistors and capacitors representing various interfacial and transport processes in the device.

The total impedance of electrical equivalent of DSCs is given by:

$$Z_{IF} = 2\left(\frac{R_T}{R_{CT}}\right)^{1/2} \frac{1}{C_\mu}(i\omega_{CT})^{-\beta} \tag{6.1}$$

where R_T ($=r_tL$) is the transport resistance, i.e., total resistance offered by the photoelectrode film; R_{CT} ($=r_{ct}/L$) is the resistance to the charge transfer from the photoelectrode to the electrolyte; C_μ ($=c_\mu L$) is the chemical capacitance; and ω_{CT} is the characteristic frequency at which the charge transfer occurs (Jennings J.R. et al., 2011). The r_t, r_{ct}, and c_μ are the component of the electrical equivalent model and the units for the distributed parameters r_t, r_{ct}, and c_μ are then Ωcm, Ωcm^3, and F cm^{-3}, respectively (Jennings J.R., et al., 2011 and Wang Q. et al., 2006). The parameter β is the exponent of the constant phase element representing the deviation from capacitance at the planer semiconductor – electrolyte interface (Wang Q. et al., 2006). A lower R_S (< 20 Ω) and high R_{REC} ($>10^3\Omega/cm^2$) is preferred for high η_C. The R_S is determined from the high frequency region ($>10^4$ Hz) of the EIS spectrum and R_{REC} from mid frequencies ($\sim10^3 - 10^2$ Hz) (Bisquert J., et al., 2000).

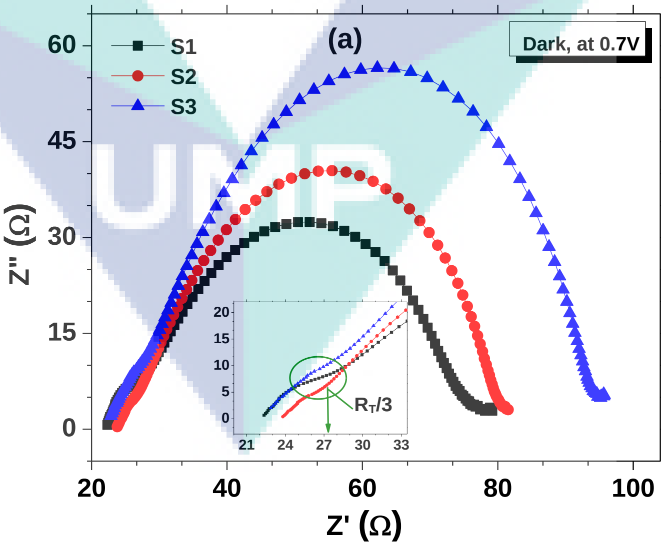

Figure 6.5: Impedance spectra of DSCs at a potential close to V_{OC} (0.7 V) measured in dark.

Figure 6.5 shows the Nyquist plots of the three sets of devices. The Nyquist plot of DSCs ideally consists of three semi-circles; the first of which in the high frequency region (1 MHz —0.1 kHz) corresponds to electron transport at TiO_2/FTO interface, the second one at the intermediate frequency range (0.1 kHz – 1 Hz) represents the electron capture and transfer by I_3^- at TiO_2/electrolyte interface, and the third semicircle in the low frequency region (<1 Hz) relates to ion diffusion and the charge transfer at Pt/electrolyte interface (Wang Q. et al., 2005b). The real part of the complex impedance at the point where the first and second semicircles merge is a measure of the R_T; it shows a decrement upon splitting the photoelectrode volume. The width of the second semicircle is a measure of R_{CT} (Fabregat-Santiago et al., 2007), which systematically increased from S1 to S3 thereby indicating that S1 is characterized by an increased recombination than S3.

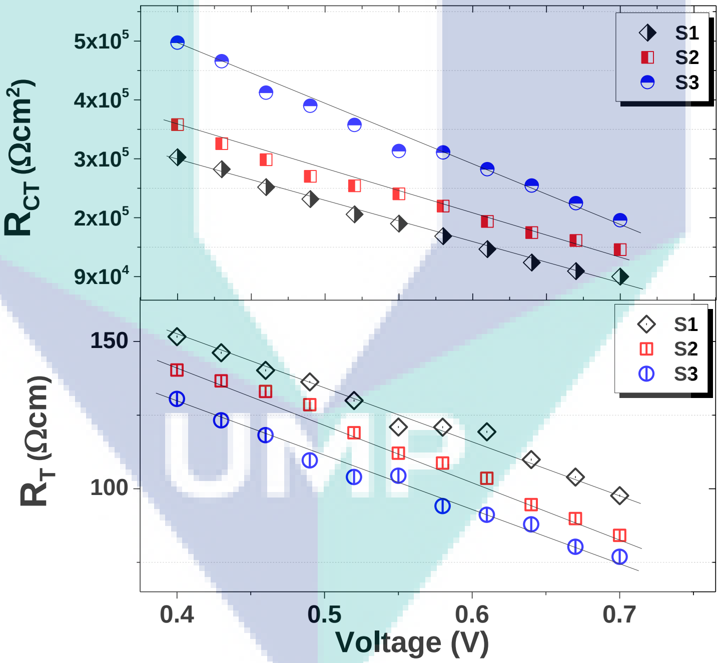

Figure 6.6: Recombination resistance also called charge transfer resistance of all the devices (top panel) and Charge transport resistance of all the devices over a range of applied voltage (lower panel).

Figure 6.6 summarizes the charge transport parameters obtained using the transmission line model. The R_T calculated using the transmission line model decreased systematically in split cells (S2 and S3) as shown in Figure 6.6(lower panel). The R_T decreased ~7% between S1 and S2 and 13-15% between S1 and S3. The variation in the value of R_T is rather small in all batches of DSCs and it does not have a significant contribution to the overall charge collection. The little variation in R_S is also evident from the I-V curve (a resistance offered to the electron transport) which is calculated at a point near V_{OC}; it showed a marginal decrement in split cell (0.21 Ω in S3 compared to S1). The major contribution to the improved transport parameters is observed to be from the R_{CT}, which increased upon splitting the cell area thereby favouring high collection efficiency. The R_{CT} increased ~40% from S1 to S2 and ~100% from S1 to S3. These increments in the R_{CT} are consistent with the shunt resistance calculated from I-V curve for the three samples, i.e. ~ 30% increment from S1 to S2 and ~1 fold increment from S1 to S3. The variations in R_{CT} suggest that a major number of electrons in split cells survived recombination which may be due to shorter diffusion pathways available in split designs. In such a situation, the electron in split cell must be collected much faster than those in single cells. To find the source of the variation in R_{CT} we calculated electron lifetime and transit time of the three devices.

6.4.2 Carrier Lifetime Investigations in Split Photoanodes

Figure 6.7 shows the Bode plots of the three DSCs. The electron lifetime is calculated using the equation $\tau_n = 1/\omega_{CT}$. The lowest τ_n is observed in conventional photoelectrode designs which systematically increased in split designs: for S-1, the peak frequency (f_C) was 122 Hz which was shifted systematically to 107.5 Hz in S-2 and f_C ~ 96 Hz in S-3. The corresponding τ_n for S-1, S-2 and S-3 were 12, 15.4 and 17.5 ms respectively. It can be observed that electrons are short lived in S-1 and are characterized by the highest τ_n in S-3.

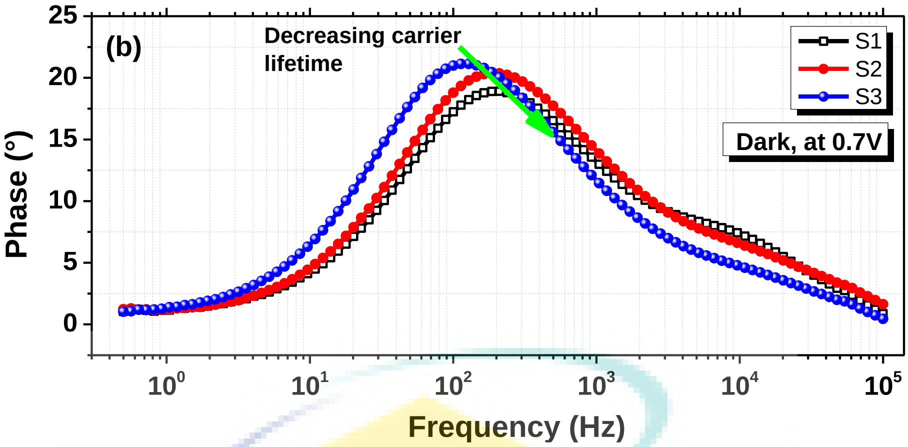

Figure 6.7: Corresponding Bode Plots of the three DSCs (S-1, S-2, & S-3).

Electron lifetime (τ_n) and electron transit time (τ_d) are widely employed to estimate charge collection efficiency of DSCs (Bisquert J., 2008; Martinson, et al., 2009). The τ_d is the time required for photogenerated electrons to be collected at working electrode and calculated by the relation $\tau_d = R_T \cdot C_\mu$, where C_μ is the chemical capacitance and obtained through transmission line model as described earlier. This relation is reliable when C_μ is conceived as purely chemical and denotes density of states.

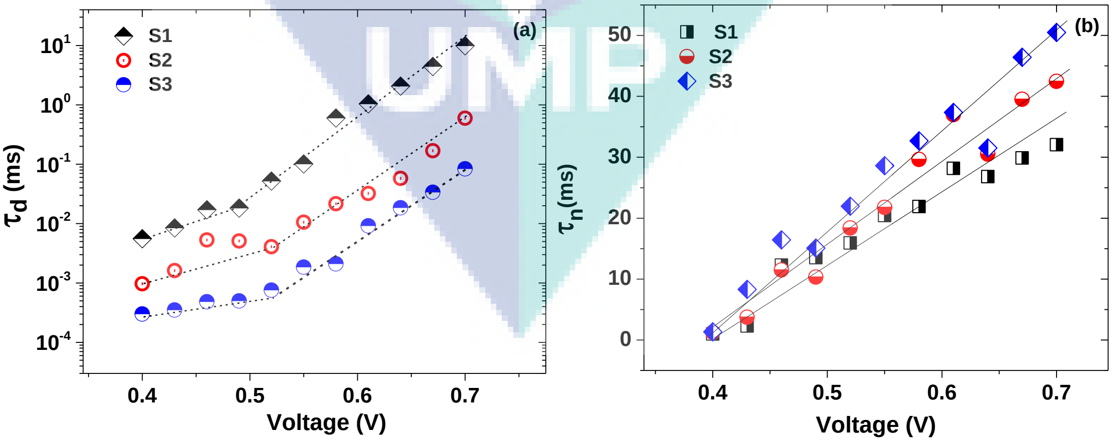

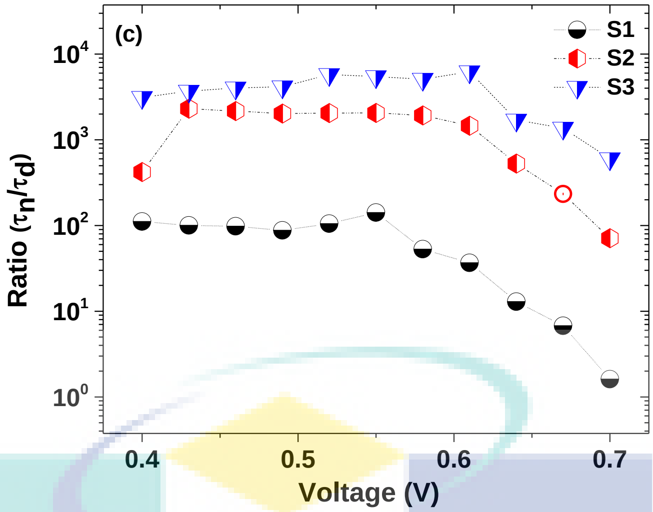

Figure 6.8: The electron transit time of the three devices calculated over a range of applied voltage, (b) electron lifetime of the devices, and (c) the ratio of electron lifetime and transit time.

Figure 6.8 a&b show the τ_d and τ_n of the three devices and 6.8c depicts a competition between their τ_n and τ_n by correlating them. The split designs showed remarkably shorter τ_d compared to the single cell; the τ_d is one fold shorter in S2 and ~2 times shorter in S3 compared to S1. The faster electron collection in the split cells S2 and S3 is therefore obvious from shorter diffusion pathways for electron transport; whereas in design S1, the longer path length is evident from their much higher τ_d. This higher τ_d significantly contributes to high recombination in the design S1, where the movement of the electrons is not confined by appropriate device designs and reckoned as a source of relatively poorer photovoltaic parameters in this design. Equally important is the nominal difference in τ_n of the three devices as shown in Figure 4.8b.

For a device to show high collection efficiency, the ratio of τ_n/τ_d should be high, i.e., the electrons should be collected much before their lifetime in order to minimize recombination in the device.(Fakharuddin, et al., 2014a) This ratio calculated in devices S1–S3 is noteworthy (Figure 4.8b). It is two orders of magnitude higher in split cells (S2 and S3) compared to that of a single cell stack (S1) which confirms that the split design of devices have an improved recombination resistance. One may expect the collection efficiency of S3 and S2 to be higher than that of S1 based on their nominally dissimilar τ_n and considerably different τ_d. In split designs the electrons need much lesser than their lifetime for collection compared to conventional design. The splitting of photoelectrode volume in large area devices may lead to shorter path length of electrons, eventually reducing their recombination with the holes in electrolyte. The concept is previously disregarded in all the larger area DSCs designs. Even though a higher current is routinely achieved in large area DSCs but the value of J_{SC} drops 30-50% compared to highly efficient single cells. This diminution in J_{SC} values originates from considerable loss in photoinduced electrons or in other words, enhanced recombination as a result of increased diffusion pathways.

6.4.3 Chemical Capacitance and Diffusion Coefficient in Split Photoanodes

Another important photovoltaic parameter is chemical capacitance in the DSCs which shows the electron density under illumination or at a biased voltage. Figure 6.9a represents chemical capacitance (C_μ) calculated via electrical impedance model. The C_μ which represents a change in electron density over a small variation of chemical potential is expressed as (Juan Bisquert, 2008):

$$C_\mu = \frac{N_e^2}{k_B T_o} \exp\left[{(E_F - E_o)} \middle/ {k_B T_o} \right] \tag{6.2}$$

Where N is the density of electronic states, E_o is the bottom of the conduction band energy, e is the elementary charge, and T_0 is the parameter with temperature units that determine the depth of the distribution of electronic states arise from surface states. The normalized C_μ, extracted using transmission line model ($c_\mu = C_\mu / Ad$) did not show a notable dependence of photoelectrode volume and the observed little variation is of statistical origin, i.e. an increase in volume led to the redistribution of localized energy states in the TiO_2 bandgap (Bisquert J., 2003). In equation 6.2, both T_o and E_o are constant due to alike employed material throughout the devices and do not depend on device dimensions, therefore, a comparison of R_{CT} and C_μ should provide details of recombination rate constant for a given value of E_F and N. Figure 6.9b shows that for a given E_F and N, R_{CT} decreased upon increasing film volume which eventually lowers the numbers of electrons collected at working electrode.

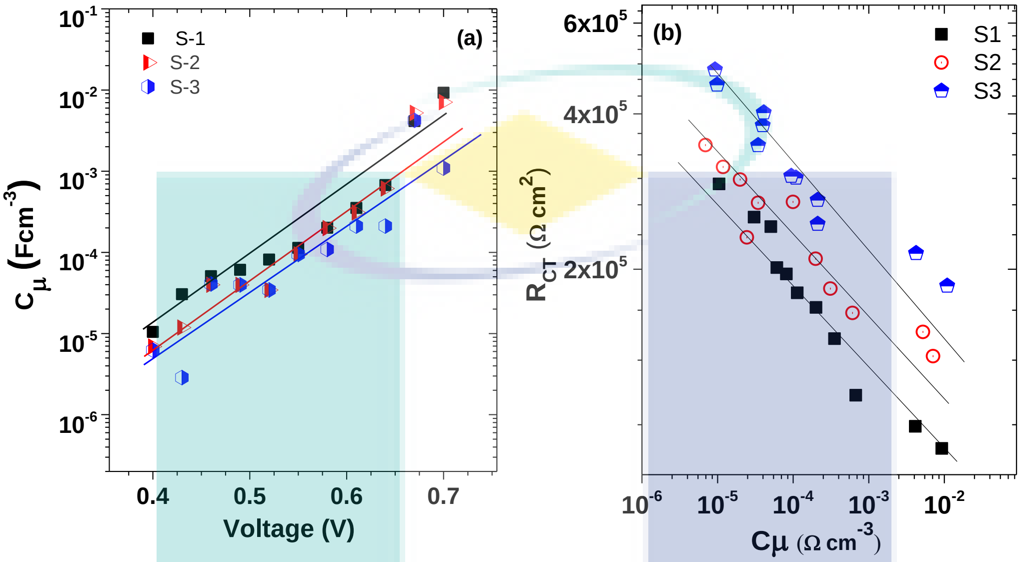

Figure 6.9: C_μ measured as a function of applied voltage of the three devices, (b) C_μ versus R_{CT} of the devices extracted using widely accepted transmission line model.

We also observed that the lower τ_d and improved η_c in the new design successfully overcome inferior chemical diffusion coefficient (D_n~10^{-5} cm^2/s) (Bisquert J., 2004) in mesoporous TiO_2 arising from the trap – limited diffusion mechanism. The D_n calculated for the devices vary considerably: S1~1.44×10^{-5}, S2~2.44×10^{-5} and S3~1.8×10^{-4} cm^2/s at 0.7 V thereby establishing that the geometrical restriction of electron movement in the new designs surpassed limitations of the trap – limited diffusion process.

6.4.4 Improved Charge Collection Efficiency in Split Photoanodes

The competition between collection and recombination of electrons in DSCs is characterized by its L_n (Q. Wang, et al., 2006). The L_n is determined from the diffusion coefficient (D_n) through $L_n = (D_n \tau_d)^{1/2}$ from EIS data. Figure 6.10 (a) shows normalized

L_n with respect to film thickness. It is evident that the device S3 showed four-times higher L_n (~50 µm) compared to that of S1 at all bias potentials. i.e. S3 is characterized by excellent transport properties. The L_n of S2 is twice that of the d (however, lower than S3) and still characterized by improved transport properties than S1 in which L_n is nearly similar to the film thickness.

As we have clearly seen the dependence of R_{CT} and τ_d on photoelectrode volume, an investigation of collection efficiency (η_c) will corroborate the origin of enhanced photovoltaic parameters in split designs of photoelectrodes. We calculated η_c of the three devices using the equation for steady state electron collection and the values are shown in Figure 6.10b. The η_c is usually determined by correlating the distance between the point of electron generation to FTO (contact substrate) and diffusion length (Sodergren, et al., 1994).

$$\eta_{c,WE} = \frac{\left(-L_n\alpha\cosh\left(d/Ln\right)+\sinh\left(d/Ln\right)+L_n\alpha e^{-\alpha d}\right)}{\left(1-e^{-\alpha d}\right).\left(1-L_n^2\alpha^2\right)\cosh\left(d/Ln\right)} \qquad (6.3)$$

Here, α is the absorption co-efficient, 'd' is the film thickness and 'L_n' is the diffusion length which is given as $L_n = \left(D_n\tau_n\right)^{1/2}$ .L_n is experimentally calculated from impedance measurements and its relation with film thickness is shown in Figure 6.10a. As the absorbance at 550 nm is ~90%, the values of α.d=1 (Halme J. et a,. 2008 and Chen et al., 2013) The values of η_c for S1, S2, and S3 are 84%, 92.7%, and 98.3% respectively, which clearly explains the source of improved J_{SC}. i.e., lower τ_d and lower recombination improved the photocurrent as $J_{SC} = f\left(\eta_\alpha.\eta_{inj}.\eta_c\right)$, where η_α and η_{inj} are the absorption and injection efficiencies (Grätzel M., 2009). Though the equation does not justify for all values of "*d*", yet this is one of the most reliable methods available to calculate collection efficiency (Chen, et al., 2013; Halme, et al., 2008). A generalized equation considering diffusion volume is yet to be drawn.

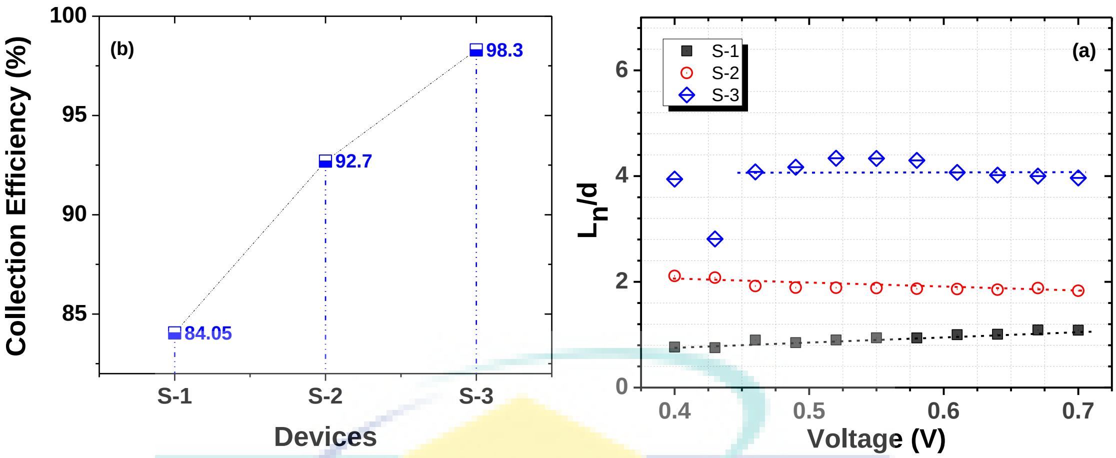

Figure 6.10: (a) L_n/d calculated from impedance spectroscopy measurements **(b)** collection efficiency of the three devices calculated using equation 6.3.

Table 6.2: Calculated collection efficiency of devices equation 6.3.

Device	J_{SC} (mA/cm^2)	Thickness(µm)	L_n/L	η_c (%)
S1	10.93	14.1	1.08	84.05
S2	13.24	14.2	1.83	92.7
S3	16.6	14.1	3.96	98.3

It is important to note that the photoelectrodes thickness of the three devices (±14.2µm) was similar; and therefore, employing diffusion length (L_n) alone as a device parameter should result in similar photovoltaic parameters. However, a notable difference in J_{SC} and η_C is observed in S2 and S3. The L_n with its present realization (with respect to photoelectrode thickness alone) fails to explain the origin of this enhancement. An improved realization is photoelectrode volume (V_D) which covers all three dimensions of photoelectrode viz area and thickness. By employing V_D as a device parameter, the origin of photovoltaic parameters in devices of similar volume could be well explained.

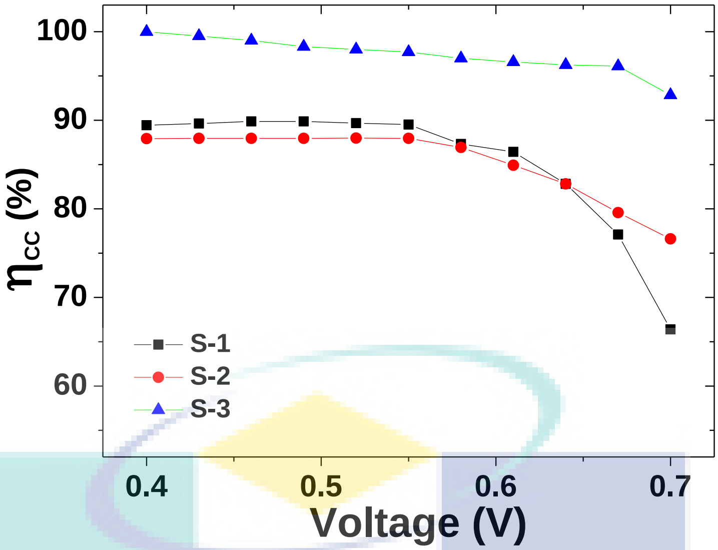

Figure 6.11: Electron collection efficiency of the three DSCs calculated from impedance spectroscopy measurements.

The further verfiy the improved charge transport in split photoelectrodes, the collection efficiency of the devices were calculated from τ_n and electron trasit time τ_d by using the expression $\eta_{cc} = 1 \Big/ \left(1 + \left({\tau_d}/{\tau_n} \right)\right)$. As shown in Figure 6.11, the split photanode DSCs (S-3 & S-2) showed ~17%and 9.5% increased charge collection than that of conventional design (S-1) respectiely in photoanodes of similar thickness (14±0.5 μm). This increment is due to the fact that the diffusion length ($L_n = L\sqrt{R_{CT}/R_T}$), i.e., the distance travelled by electrons before recombination in split photoanodes is 2 – 4 times higher than that of S-1 (Table 6.2). An enhanced τ_n and significantly higher L_n demonstrates the benifical effects when split photoanode designs are employed in DSCs.

6.5 CONCLUSIONS

The charge transport parameters in dye-sensitized solar cells improved when a photoanode is split into multiple arrays on the same substrate. We proved that by altering the geometric size of the photoelectrode and their distribution, the photocurrent in mesoporous TiO_2 based DSCs could be significantly improved owning to the betterment in their electrical transport. Our analysis revealed that the charge transport strongly depends on the varied choice of diffusion pathways and that the charge recombination resistance and electron lifetime could be increased in materials of similar chemical capacitance and Fermi energy by restricting the diffusion pathways. In our experiments, the charge recombination resistance in split designs increased up to ~70% in multiple stacked cells compared to a conventional DSC design. An overall increase in the photovoltaic efficiency and photocurrent was obtained when tinier cells are stacked on the same substrate compared to a single patch of electrode of similar area. Results from this study provide new directions to build high efficiency modules using the current choice of material.

CHAPTER 7

CONCLUSIONS AND OUTLOOK

7.1 CONCLUSIONS

The objective of this study was to investigate the factors behind the lowering of photovoltaic parameters while increasing the electrode size and to propose and validate the device designs with improved charge collection efficiency. Although the drop in photovoltaic performance in large area dye-sensitized solar cells (DSCs) in previous reports is observed no systematic efforts are undertaken to quantify the lowering of photovoltaic parameters with device area. We chose commercially available materials to investigate such missing links. The highlights and the key findings of the study are as follows:

i. DSCs with varying photoelectrode area (~0.16 – ~1.96 cm^2) were fabricated via screen printing and tested at 1 sun conditions (100 mW/cm^2). The current-voltage studies revealed that the photovoltaic performance (η) of the DSC with smallest active area is 3 times higher than that of the highest active area: the DSC with active area ~0.16 cm^2 showed η ~6.7% (J_{SC} = ~13 mA/cm^2) significantly higher than the DSCs with active area ~1.96 cm^2 (η = 2%, J_{SC} = ~5 mA/cm^2). The power output of the former is also 3 time higher than the latter (6.75 mW for $DSC_{0.16}$ and 2.09 mW for $DSC_{1.96}$).

ii. The η drop off bi-exponentially with increasing photoelectrode area; a loss of ~65% in the η of DSCs is observed when the area of the electrode is increased in the range ~0.15 – 1.96 cm^2. The J_{SC} is found to be the main contributor to this drop and it followed the same bi-exponential drop as that of η. The V_{OC} remained at similar values in the area range 0.16 – 0.36 cm^2 after which it gradually decreased. The FF however remained practically the same.

iii. Electrochemical impedance spectroscopy (EIS) studies were conducted to investigate the factors behind the area dependent photovoltaic performance drop. Higher charge transfer resistance (R_{CT}) was observed for DSCs of lower areas which lowered nominally as the area was increased, i.e., the η of the devices follow the same trend as that of R_{CT}. A step-fall in R_{CT} was observed for areas >0.5 cm^2, which further decreased systematically similar to those of areas <0.5 cm^2. Note that V_{OC} also showed a sharp decrease below this area indicating that a large fraction of photogenerated electrons are not collected in devices of areas >0.5 cm^2, above which both J_{SC} and η vary drastically.

iv. The ratio of electron lifetime (τ_n) to transit time (τ_d) was significantly higher in smaller area photoandes than those of larger area DSCs: it reduced 4 orders of magnitude between $DSC_{0.16}$ and $DSC_{1.96}$. The key contributor here was the τ_d which increased 3 orders of magnitude from lowest active area to highest active area. We observed that upon increasing the photoanode area, the photogenerated electrons experience longer diffusion paths (longer τ_d) and are never collected when $\tau_n > \tau_d$.

v. The simultaneous lowering of R_{CT} and improved τ_n in devices of area >0.5 cm^2 suggest that electrons survived from recombination only are collected. The collected electrons from areas >0.5 cm^2 having increased lifetime are only a fraction of the total and the remaining were lost due to enhanced diffusion pathways. The collected minor fraction of electrons, which is only ~35% in device of active area ~1.96 cm^2 compared to that of a DSC of area

~0.16 cm^2, likely result from the first few monolayers in contact with the working electrode. Therefore, the mechanism of area-dependent electron loss is fairly obvious due to enhanced transit length; thereby lowering the R_{CT}.

vi. Based on the above findings, split photoanode designs were proposed to fabricate high efficiency dye-sensitized solar modules (DSMs). These designs were fabricated by dividing a given photoelectrode film volume into tinier multiple patches with an inter-patch spacing ~200 – 1000 μm such that the electron movement was limited within the tiny patches by the frequent gaps within the electrode film. The photovoltaic performance of such designs was compared to that of the conventional DSC designs.

vii. In a comparative study, conventional (S1) and split photoelectrode (S2 & S3) designs were investigated for a given active area (0.28 cm^2). In S2 the active area was split into two strips of areas ~0.14 cm^2 each with a spacing of ~0.2 mm whereas the S3 was composed of four strips of area 0.07 cm^2 each with similar interspacing.

viii. The η increased systematically from devices S1 to S3. Major contribution to the increase in η resulted from J_{SC} which increased from 11 mA/cm^2 to 17 mA/cm^2 when the area of the individual stacks is reduced from 0.28 cm^2 to 0.07 cm^2. i.e., the devices fabricated with a combination of a multiple electrode arrays (S2&S3, which have no additional connection than the already present connection via FTO) showed higher photocurrent than that is achieved by a single electrode film of similar area (S1). The 21% and 52% increase in J_{SC} in S2 and S3 compared with S1 clearly established the beneficial effects when the diffusive path is restricted by appropriate device designs.

ix. The EIS study of the three devices revealed improved τ_n, lowered τ_d, improved R_{CT}, longer diffusion length (L_n) and improved charge collection efficiency (ηc) to be the source of improved photovoltaic performance in split photoanode designs.

x. It is important to note that the photoelectrodes thickness of the three devices (14±0.2µm) was similar; and therefore, employing diffusion length (L_n) alone as a device parameter should result in similar photovoltaic parameters. However, a notable difference in J_{SC} and η_C is observed in S2 and S3. The L_n with its present realization (with respect to photoelectrode thickness alone) has limitation to explain the origin of this enhancement. An improved realization is photoelectrode volume (V_D) which covers all three dimensions of photoelectrode viz area and thickness. By employing V_D as a device parameter, the origin of photovoltaic parameters in devices of similar volume could be well explained.

7.2 OUTLOOKS

The questions that need to be answered at the end of the study are: *"how efficient will a dye-sensitized solar module be, what are the various reasons of the comparatively lower η of DSMs well below their laboratory scale analogues, and what are various strategies leading to a high efficiency DSM?"*

Firstly, there are no theoretical limits that would impede the performance of a DSM from being as efficient as their laboratory scale analogues (13% at 1 sun). The DSMs suffers from charge recombination, added series resistance in large electrode areas and lack of suitable device designs to meet such recombination and inferior chemical diffusion coefficient (D_n ~10^{-5} cm^2/s). Different strategies might be adopted for efficient DSMs. For example, as the R_{CT}, ratio of τ_{n}/τ_{d} and η_c strongly depends on the active area; the photoanode area has to be restricted for complete charge collection. Conventionally, DSMs are made using long strips of active area ≥3 cm^2.

Although the split designs resulted in enhanced performance in smaller photoanodes (0.28 & 1 cm^2) up-scaling of such designs is found to be challenging in liquid based DSMs as the mass transport of electrolyte from one cell to another caused difference in concentration of the redox species. We note that such split designs are likely to add difficulty in fabrication process as sealing and interconnection of individual cell is a major issue. However, such designs have greater success possibility in *s*-DSMs because difference in concentration of the redox species between the neighbouring cells does not arise in solid electrolytes. Furthermore, the splitting of the photoanode in tinier cell results in significantly higher inactive area which penalizes the overall performance of the DSMs. A best compromise has to be made between the inactive area and the efficiency for final devices.

In view of future commercial applications, *s*-DSMs based on split photoanode designs are anticipated to be promising. Based on the connection types, these cells are likely to provide very high photocurrent or photovoltage in DSMs. As an example, a peak power of 1W could be achieved in 12 cm^2 by arranging sixty state-of-the-art DSCs (η~12.3%) of area ~0.2 cm^2 and thickness ~15 μm in series.

Another research area that can be developed from this study is one-dimensional (1D) nanomaterials such as nanowires, nanorods, and nanotubes etc. based DSMs. Owning to their 1D nature and faster electronic transport, such materials are likely to provide improve charge transport, even in the conventional photoanode designs, where the fabrication and sealing is significantly easier compared to our proposed designs.

REFERENCES

Agarkar, S. A., Dhas, V. V., Muduli, S., & Ogale, S. B. 2012. Dye sensitized solar cell (DSSC) by a novel fully room temperature process: A solar paint for smart windows and flexible substrates. *RSC Advances*, ***2***(31), 11645-11649.

Archana, P. S., Jose, R., Yusoff, M. M., & Ramakrishna, S. 2011. Near Band Edge electron diffusion in electrospun Nb-doped anatase nanofibers probed by electrochemical impedance spectroscopy. *App. Phys. Lett.*, **98**, 152106.

British Petroleum. 2013. solar generation PV capacity, http://www.bp.com/en/global/corporate/about-bp/statistical-review-of-world-energy-2013/review-by-energy-type/renewable-energy/solar-energy.html. Retrieved on 12-12-2013.

Bach, U., Lupo, D., Comte, P., Moser, J. E., Weissörtel, F., Salbeck, J., Grätzel, M. 1998. Solid-state dye-sensitized mesoporous TiO 2 solar cells with high photon-to-electron conversion efficiencies. *Nature*, **395**(6702), 583-585.

Baxter, J. B., & Aydil, E. S. 2005. Nanowire-based dye-sensitized solar cells. *App. Phys. Lett.*, **86**(5), 053114. doi: doi:http://dx.doi.org/10.1063/1.1861510

Biancardo, M., West, K., & Krebs, F. C. 2006. Optimizations of large area quasi-solid-state dye-sensitized solar cells. *Solar Energy Materials and Solar Cells*, **90**(16), 2575-2588.

Bisquert, J., Garcia-Belmonte, G., Fabregat-Santiago, F., Ferriols, N. S., Bogdanoff, P., & Pereira, E. C. 2000. Doubling Exponent Models for the Analysis of Porous Film Electrodes by Impedance. Relaxation of TiO2 Nanoporous in Aqueous Solution. *J. Phys. Chem. B*, **104**(10), 2287-2298.

Bisquert, J. 2002. Theory of the impedance of electron diffusion and recombination in a thin layer. *J. Phys. Chem. B*, **106**(2), 325-333.

Bisquert, J. 2003a. Chemical capacitance of nanostructured semiconductors: its origin and significance for nanocomposite solar cells. *PCCP*, **5**(24), 5360-5364

Bisquert, J. 2003b. Chemical capacitance of nanostructured semiconductors: its origin and significance for nanocomposite solar cells. *Phys. Chem. Chem. Phys.*, **5**, 5360-5364.

Bisquert, J. 2004. Chemical Diffusion Coefficient of Electrons in Nanostructured Semiconductor Electrodes and Dye-Sensitized Solar Cells. *J. Phys. Chem. B*, **108**(7), 2323-2332.

Bisquert, J. 2007a. Hopping transport of electrons in dye-sensitized solar cells. *Journal of Physical Chemistry C,* **111**(46), 17163-17168.

Bisquert, J. 2007b. Hopping transport of electrons in dye-sensitized solar cells. *J. Phys. Chem. C,* **111**, 17163-17168.

Bisquert, J. 2008a. Beyond the quasistatic approximation: Impedance and capacitance of an exponential distribution of traps. *Phys. Rev. B,* **77**(23), 235203.

Bisquert, J. 2008b. Physical electrochemistry of nanostructured devices. *PCCP,* **10**(1), 49-72.

Bisquert, J., Fabregat-Santiago, F., Mora-Seró, I., Garcia-Belmonte, G., Barea, E. M., & Palomares, E. 2008c. A review of recent results on electrochemical determination of the density of electronic states of nanostructured metal-oxide semiconductors and organic hole conductors. *Inorganica Chimica Acta,* **361**(3), 684-698.

Chen, P. Y., Dang, X., Klug, M. T., Qi, J., Dorval Courchesne, N. M., Burpo, F. J., Belcher, A. M. 2013. Versatile three-dimensional virus-based template for dye-sensitized solar cells with improved electron transport and light harvesting. *ACS Nano*, **7**(8), 6563-6574.

Chiba, Y., Islam, A., Watanabe, Y., Komiya, R., Koide, N., & Han, L. 2006. Dye-sensitized solar cells with conversion efficiency of 11.1%. *Japanese Journal of Applied Physics, Part 2: Letters*, **45**(24-28), L638-L640.

Chung, I., Lee, B., He, J., Chang, R. P. H., & Kanatzidis, M. G. 2012. All-solid-state dye-sensitized solar cells with high efficiency. *Nature*, **485**(7399), 486-489.

Clay H. Seaman. 1982. Calibration of solar cells by the reference cell method—The spectral mismatch problem. *Solar Energy*, **29** (4), 291-298.

Crossland, E. J. W., Noel, N., Sivaram, V., Leijtens, T., Alexander-Webber, J. A., & Snaith, H. J. 2013. Mesoporous TiO 2 single crystals delivering enhanced mobility and optoelectronic device performance. *Nature*, **495**(7440), 215-219.

Daeneke, T., Kwon, T. H., Holmes, A. B., Duffy, N. W., Bach, U., & Spiccia, L. 2011. High-efficiency dye-sensitized solar cells with ferrocene-based electrolytes. *Nature Chemistry*, **3**(3), 211-215.

Dai, S., Weng, J., Sui, Y., Chen, S., Xiao, S., Huang, Y., . . . Wang, K. 2008. The design and outdoor application of dye-sensitized solar cells. *Inorg. Chim. Acta,* **361**(3), 786-791.

Dai, S., Weng, J., Sui, Y., Shi, C., Huang, Y., Chen, S., . . . Wang, K. 2004. Dye-sensitized solar cells, from cell to module. *Solar Energy Materials and Solar Cells,* **84**(1-4), 125-133.

Docampo, P., Guldin, S., Leijtens, T., Noel, N. K., Steiner, U., & Snaith, H. J. 2014. Lessons Learned: From Dye-Sensitized Solar Cells to All-Solid-State Hybrid Devices. *Advanced Materials*, n/a-n/a.

Dyesol. 2011. Advantage of solar cell technology. Retrieved 13 December 2013.

Dyesol. 2013a. Current Commercialisation Projects & Collaborations, *Dyesol Media*. Retrieved 13 December 2013.

Dyesol. 2013b. Dyesol Achieves Technical Breakthrough In Solid State DSC, Retrieved on November 2013.

Fabregat-Santiago, F., Bisquert, J., Garcia-Belmonte, G., Boschloo, G., & Hagfeldt, A. 2005. Influence of electrolyte in transport and recombination in dye-sensitized solar cells studied by impedance spectroscopy. *Sol. Energy Mater. Sol. Cells,* **87**(1–4), 117-131.

Fabregat-Santiago, F., Bisquert, J., Palomares, E., Otero, L., Kuang, D., Zakeeruddin, S. M., & Grätzel, M. 2007. Correlation between Photovoltaic Performance and Impedance Spectroscopy of Dye-Sensitized Solar Cells Based on Ionic Liquids. *J. Phys. Chem. C,* **111**(17), 6550-6560.

Fakharuddin, A., Archana, P. S., Kalidin, Z., Yusoff, M. M., & Jose, R. 2013. Standardization of photoelectrode area of dye-sensitized solar cells. *RSC Adv.*, **3**(8), 2683-2689.

Fakharuddin A., R. Jose, P. S. Archana, & Yusoff, M. M. (2013b). On the scalability of dye-sensitized solar cells: Effects of photoelectrode area on the photovoltaic and charge transport parameters. *Ab. Am. Chem. Soc.,, Vol. 245.*

Fakharuddin A., Ahmed I., Khalidin Z., Yusoff M. M., & Jose., R. 2014a. Channeling of electron transport to improve collection efficiency in mesoporous titanium dioxide dye sensitized solar cell stacks. *App. Phy. Lett.*, **104**, 053905.

Fakharuddin, A., Ahmed, I., Khalidin, Z., Yusoff, M. M., & Jose, R. 2014b. Charge transport through split photoelectrodes in dye-sensitized solar cells. *J. Appl. Phys.* **115**(16).

Fakharuddin A., Ahmed I., Wali Q., Kalidin, Z., Yusoff, M. M., & Jose, R. 2014c. Probing Electron Lifetime and Recombination Dynamics in Large Area Dye-Sensitized Solar Cells by Electrochemical Impedance Spectroscopy. *Advanced Materials Research* **295**, 553-558.

Fakharuddin A., Bisquert J., Rajan J..2014d. Roadmap for dye-sensitized solar cells. *Energy Environ.Sci.*, accepted manuscript.

Fan, X., Chu, Z. Z., Wang, F. Z., Zhang, C., Chen, L., Tang, Y. W., & Zou, D. C. 2008. Wire-Shaped Flexible Dye-sensitized Solar Cells. *Advanced Materials*, **20**(3), 592-595.

First Solar. 2013. Industry benchmark Thin Film Modules. from http://www.firstsolar.com/Innovation/Advanced-Thin-Film-Modules. Retrieved 12-12-2013.

Fisher, A. C., Peter, L. M., Ponomarev, E. A., Walker, A. B., & Wijayantha, K. G. U. 2000. Intensity Dependence of the Back Reaction and Transport of Electrons in Dye-Sensitized Nanocrystalline TiO2 Solar Cells. *J. Phys. Chem. B*, **104**(5), 949-958.

Giordano, F., Guidobaldi, A., Petrolati, E., Vesce, L., Riccitelli, R., Reale, A., . . . Di Carlo, A. 2013. Realization of high performance large area Z-series-interconnected opaque dye solar cell modules. *Progress in Photovoltaics: Research and Applications*, **21**(8), 1653-1658.

Giordano, F., Petrolati, E., Brown, T. M., Reale, A., & Di Carlo, A. 2011. Series-connection designs for dye solar cell modules. *IEEE Transactions on Electron Devices*, **58**(8), 2759-2764.

Gonzalez-Vazquez, J. P., Anta, J. A., & Bisquert, J. 2010. Determination of the electron diffusion length in dye-sensitized solar cells by random walk simulation: Compensation effects and voltage dependence. *J. Phys. Chem. C*, **114**(18), 8552-8558.

Grätzel, M. 2003. Dye-sensitized solar cells. *J. Photochem. Photobiol.*, **4**(2), 145-153.

Grätzel, M. 2009. Recent Advances in Sensitized Mesoscopic Solar Cells. *Acc. Chem. Res.*, **42**(11), 1788-1798.

Green, M. A., Emery, K., Hishikawa, Y., Warta, W., & Dunlop, E. D. 2014. Solar cell efficiency tables (version 43). *Progress in Photovoltaics: Research and Applications*, **22**(1), 1-9.

Gregg, B. A., & Hanna, M. C. 2003. Comparing organic to inorganic photovoltaic cells: Theory, experiment, and simulation. *Journal of Applied Physics*, **93**(6), 3605-3614.

Hagfeldt, A., Boschloo, G., Sun, L., Kloo, L., & Pettersson, H. 2010. Dye-sensitized solar cells. *Chem. Rev.*, **110**(11), 6595-6663.

Halme, J., Boschloo, G., Hagfeldt, A., & Lund, P. 2008. Spectral characteristics of light harvesting, electron injection, and steady-state charge collection in pressed TiO2 dye solar cells. *J. Phys. Chem. C,* **112**(14), 5623-5637.

Halme, J., Vahermaa, P., Miettunen, K., & Lund, P. 2010. Device physics of dye solar cells. *Advanced Materials,* **22**(35), E210-E234.

Han, L., Fukui, A., Chiba, Y., Islam, A., Komiya, R., Fuke, N., . . . Shimizu, M. 2009. Integrated dye-sensitized solar cell module with conversion efficiency of 8.2%. *App. Phy. Lett.,* **94**(1).

Han, L., Islam, A., Chen, H., Malapaka, C., Chiranjeevi, B., Zhang, S., Yanagida, M. 2012. High-efficiency dye-sensitized solar cell with a novel co-adsorbent. *Energy Environ.Sci.,* **5**(3).

Hardin, B. E., Snaith, H. J., & McGehee, M. D. 2012. The renaissance of dye-sensitized solar cells. *Nat. Photon.,* **6**(3), 162-169.

Hashmi, G., Miettunen, K., Peltola, T., Halme, J., Asghar, I., Aitola, K., Lund, P. 2011. Review of materials and manufacturing options for large area flexible dye solar cells. *Renewable and Sustainable Energy Reviews,* **15**(8), 3717-3732.

He, J., Lindström, H., Hagfeldt, A., & Lindquist, S. E. 1999. Dye-Sensitized Nanostructured p-Type Nickel Oxide Film as a Photocathode for a Solar Cell. *Journal of Physical Chemistry B,* **103**(42), 8940-8943.

He, J., Lindström, H., Hagfeldt, A., & Lindquist, S. E. 2000. Dye-sensitized nanostructured tandem cell-first demonstrated cell with a dye-sensitized photocathode. *Solar Energy Materials and Solar Cells,* **62**(3), 265-273.

Hinsch A., J. M. K., R. Kern, I. Uhlendorf, A. Meyer, J. Holzbock, J. Ferber. 2001. Long term stability of dye-sensitized solar cells. *Prog. Photovolt: Res. Appl.,* **9**, 425-438.

Hinsch, A., Brandt, H., Veurman, W., Hemming, S., Nittel, M., Würfel, U., Fichter, K. 2009. Dye solar modules for facade applications: Recent results from project ColorSol. *Sol. Energy Mater. Sol. Cells,* **93**(6–7), 820-824.

Hinsch, A., Veurman, W., Brandt, H., Loayza Aguirre, R., Bialecka, K., & Flarup Jensen, K. 2012. Worldwide first fully up-scaled fabrication of 60 × 100 cm2 dye solar module prototypes. *Progress in Photovoltaics: Research and Applications,* **20**(6), 698-710.

Hopkins, J. A., Phani, G., & Skryabin, I. L. 2006. Methods to implement interconnects in multi-cell regenerative photovoltaic photoelectrochemical devices: Google Patents.

International Energy Agency (IEA). 2013. Key World Energy Statistics, 2013 *IEA report*. **2013**. 1-82.

Im, J. H., Lee, C. R., Lee, J. W., Park, S. W., & Park, N. G. 2011. 6.5% efficient perovskite quantum-dot-sensitized solar cell. *Nanoscale*, **3**(10), 4088-4093.

Ito, S., Ha, N. L. C., Rothenberger, G., Liska, P., Comte, P., Zakeeruddin, S. M., Grätzel, M. 2006. High-efficiency (7.2%) flexible dye-sensitized solar cells with Ti-metal substrate for nanocrystalline-TiO2 photoanode. *Chemical Communications*, (38), 4004-4006.

Ito, S., Murakami, T. N., Comte, P., Liska, P., Gratzel, C., Nazeeruddin, M. K., & Gratzel, M. 2008. Fabrication of thin film dye sensitized solar cells with solar to electric power conversion efficiency over 10%. *Thin Solid Films, 516*, 4613-4619.

Jennings, J. R., & Peter, L. M. 2007. A reappraisal of the electron diffusion length in solid-state dye-sensitized solar cells. *J. Phys.Chem. C*, **111**(44), 16100-16104.

Jennings, J. R., Liu, Y., Safari-Alamuti, F., & Wang, Q. 2012. Dependence of dye-sensitized solar cell impedance on photoelectrode thickness. *Journal of Physical Chemistry C*, **116**(1), 1556-1562.

Jiang, N., Sumitomo, T., Lee, T., Pellaroque, A., Bellon, O., Milliken, D., & Desilvestro, H. 2013. High temperature stability of dye solar cells. *Solar Energy Materials and Solar Cells*, **119**, 36-50.

Jose R., Thavasi, V., & Ramakrishna, S. 2009. Metal oxides for dye-sensitized solar cells. *J. Am. Ceram. Soc.*, **92**(2), 289-301.

Jun, Y., Son, J.-H., Sohn, D., & Kang, M. G. 2008. A module of a TiO_2 nanocrystalline dye-sensitized solar cell with effective dimensions. *Journal of Photochemistry and Photobiology A: Chemistry, 200*(2–3), 314-317.

Kalowekamo, J., & Baker, E. 2009. Estimating the manufacturing cost of purely organic solar cells. *Solar Energy*, **83**(8), 1224-1231.

Kalyanasundaram, K. (2010). *Dye-sensitized Solar Cells* ed (1). CRC press.Switzerland. **1.** 305.

Kato, N., Takeda, Y., Higuchi, K., Takeichi, A., Sudo, E., Tanaka, H., Toyoda, T. 2009. Degradation analysis of dye-sensitized solar cell module after long-term stability test under outdoor working condition. *Solar Energy Materials and Solar Cells,* **93**(6-7), 893-897.

Kay, A., & Grätzel, M. 1996. Low cost photovoltaic modules based on dye sensitized nanocrystalline titanium dioxide and carbon powder. *Solar Energy Materials and Solar Cells,* **44**(1), 99-117.

Kern, R., Sastrawan, R., Ferber, J., Stangl, R., & Luther, J. 2002. Modeling and interpretation of electrical impedance spectra of dye solar cells operated under open-circuit conditions. *Electrochim. Acta,* **47**(26), 4213-4225.

Kim, H. S., Lee, J. W., Yantara, N., Boix, P. P., Kulkarni, S. A., Mhaisalkar, S., Park, N. G. 2013. High efficiency solid-state sensitized solar cell-based on submicrometer rutile TiO2 nanorod and CH3NH3PbI3 perovskite sensitizer. *Nano Letters,* **13**(6), 2412-2417.

Kinoshita, T., Dy, J. T., Uchida, S., Kubo, T., & Segawa, H. 2013. Wideband dye-sensitized solar cells employing a phosphine-coordinated ruthenium sensitizer. *Nat. Photonics,* **7**(7), 535-539.

Kroon, J. M. 2005. Nanocrystalline dye-sensitized solar cells having maximum performance: Nanomax final report. *Energy Research Center report,* **ECN-C--05-078**, 1-41.

Kroon, J. M., Bakker, N. J., Smit, H. J. P., Liska, P., Thampi, K. R., Wang, P., Tulloch, G. E. 2007. Nanocrystalline dye-sensitized solar cells having maximum performance. *Progress in Photovoltaics: Research and Applications*, **15**(1), 1-18.

Kumar, E. N., Jose, R., Archana, P. S., Vijila, C., Yusoff, M. M., & Ramakrishna, S. 2012. High performance dye-sensitized solar cells with record open circuit voltage using tin oxide nanoflowers developed by electrospinning. *Energy Environ.Sci.*, **5**(1), 5401-5407.

Li, B., Wang, L., Kang, B., Wang, P., & Qiu, Y. 2006. Review of recent progress in solid-state dye-sensitized solar cells. *Solar Energy Materials and Solar Cells,* **90**(5), 549-573.

Lin, L. Y., Lee, C. P., Tsai, K. W., Yeh, M. H., Chen, C. Y., Vittal, R., Ho, K. C. 2012. Low-temperature flexible Ti/TiO 2 photoanode for dye-sensitized solar cells with binder-free TiO 2 paste. *Progress in Photovoltaics: Research and Applications,* **20**(2), 181-190.

Liu, Y., Wang, H., Shen, H., & Chen, W. 2010. The 3-dimensional dye-sensitized solar cell and module based on all titanium substrates. *Appl. Energy,* **87**(2), 436-441.

Maçaira, J., Andrade, L., & Mendes, A. 2013. Review on nanostructured photoelectrodes for next generation dye-sensitized solar cells. *Renewable and Sustainable Energy Reviews,* **27**(0), 334-349.

Martinson, A. B. F., Goes, M. S., Fabregat-Santiago, F., Bisquert, J., Pellin, M. J., & Hupp, J. T. 2009. Electron transport in dye-sensitized solar cells based on zno nanotubes: Evidence for highly efficient charge collection and exceptionally rapid dynamics. *J. Phys. Chem. A*, **113**(16), 4015-4021.

Mastroianni, S., Lanuti, A., Penna, S., Reale, A., Brown, T. M., Di Carlo, A., & Decker, F. 2012. Physical and electrochemical analysis of an indoor-outdoor ageing test of large-area dye solar cell devices. *ChemPhysChem*, **13**(12), 2925-2936.

Mathew, S., Yella, A., Gao, P., Humphry-Baker, R., Curchod, B. F. E., Ashari-Astani, N., Grätzel, M. 2014. Dye-sensitized solar cells with 13% efficiency achieved through the molecular engineering of porphyrin sensitizers. *Nature Chemistry*, **6**(3), 242-247.

Matteocci, F., Casaluci, S., Razza, S., Guidobaldi, A., Brown, T. M., Reale, A., & Di Carlo, A. 2014. Solid state dye solar cell modules. *Journal of Power Sources*, *246*, 361-364.

Nattestad, A., Mozer, A. J., Fischer, M. K. R., Cheng, Y. B., Mishra, A., Bäuerle, P., & Bach, U. 2010. Highly efficient photocathodes for dye-sensitized tandem solar cells. *Nature Materials*, **9**(1), 31-35.

Navas, J., Guillén, E., Alcántara, R., Fernández-Lorenzo, C., Martín-Calleja, J., Oskam, G.,Anta, J. A. 2011. Direct Estimation of the Electron Diffusion Length in Dye-Sensitized Solar Cells. *The J.Phys. Chem. L.*, **2**(9), 1045-1050.

Naveen Kumar, E., Jose, R., Archana, P. S., Vijila, C., Yusoff, M. M., & Ramakrishna, S. 2012. High performance dye-sensitized solar cells with record open circuit voltage using tin oxide nanoflowers developed by electrospinning. *Energy and Environmental Science*, **5**, 5401-5407.

Nelson, J. 1999. Continuous-time random-walk model of electron transport in nanocrystalline TiO_{2} electrodes. *Phys. Rev. B*, **59**(23), 15374-15380.

Nelson J. 2013. Can solar power deliver? *Phil. Trans. R. Soc. A*, **371**, 4.

NERL. 2014). Best research cell efficiencies (2014). http://www.nrel.gov/ncpv/images/efficiency_chart.jpg. Retrieved on 30 May 2014.

O'Regan, B., Gratzel, Michael. 1991. A low-cost, high-efficiency solar cell based on dye-sensitized colloidal TiO2 films. *Nature*, **353**, 737-740.

Odobel, F., Pellegrin, Y., Gibson, E. A., Hagfeldt, A., Smeigh, A. L., & Hammarström, L. 2012. Recent advances and future directions to optimize the performances of p-type dye-sensitized solar cells. *Coordination Chemistry Reviews*, **256**(21-22), 2414-2423.

Park, N. G. 2013. Organometal perovskite light absorbers toward a 20% efficiency low-cost solid-state mesoscopic solar cell. *Journal of Physical Chemistry Letters,* **4**(15), 2423-2429.

Perez, R., Zweibel, K., & Hoff, T. E. 2011. Solar power generation in the US: Too expensive, or a bargain? *Energy Policy,* **39**(11), 7290-7297.

Pettersson, H., Gruszecki, T., Bernhard, R., Häggman, L., Gorlov, M., Boschloo, G., Hagfeldt, A. 2007. The monolithic multicell: a tool for testing material components in dye-sensitized solar cells. *Progress in Photovoltaics: Research and Applications*, **15**(2), 113-121.

Pettersson, H., Nonomura, K., Kloo, L., & Hagfeldt, A. 2012). Trends in patent applications for dye-sensitized solar cells. *Energy & Environmental Science,* **5**(6), 7376-7380.

Pichot, F., Pitts, J. R., & Gregg, B. A. 2000. Low-temperature sintering of TiO2 colloids: application to flexible dye-sensitized solar cells. *Langmuir,* **16**(13), 5626-5630.

Priyanka, Mohan Lal, S.N. Singh. 2007. A new method of determination of series and shunt resistances of silicon solar cells. *Solar Energy Materials & Solar Cells*. **91**. 137–142.

D. Pysch, , A. Mette, S.W. Glunz. 2007. A review and comparison of different methods to determine the series resistance of solar cells. *Solar Energy Materials & Solar Cells*. **91**. 1698–1706.

Qi, B., & Wang, J. 2013. Fill factor in organic solar cells. *Physical Chemistry Chemical Physics*, **15**(23), 8972-8982.

Ramasamy, E., Lee, W. J., Lee, D. Y., & Song, J. S. 2007. Portable, parallel grid dye-sensitized solar cell module prepared by screen printing. *Journal of Power Sources*, **165**(1), 446-449.

Ray, K. L. 2010. *Photovoltaic efficiency at elevated temperatures.* Bachelor of Science, Massachusetts Institute of Technology.

Robertson, N. 2006. Optimizing dyes for dye-sensitized solar cells. *Ang. Chem. Int. Ed.*, **45**(15), 2338-2345.

Shozo, Y., Youhai, Y., & Kazuhiro, M. 2009. Iodine/iodide-free dye-sensitized solar cells. *Acc. Chem. Res.*, **42**(11), 1827-1838.

Skoplaki, E., & Palyvos, J. A. (2009). On the temperature dependence of photovoltaic module electrical performance: A review of effciency/power correlations. *Solar Energy, 83,* 614-624.

Snaith, H. J. 2012. The perils of solar cell efficiency measurements. *Nature Photonics,* **6**(6), 337-340.

Snaith, H. J., & Schmidt-Mende, L. 2007. Advances in liquid-electrolyte and solid-state dye-sensitized solar cells. *Advanced Materials,* **19**(20), 3187-3200.

Sodergren, S., Hagfeldt, A., Olsson, J., & Lindquist, S. E. 1994. Theoretical models for the action spectrum and the current-voltage characteristics of microporous semiconductor films in photoelectrochemical cells. *J. Phys. Chem.*, **98**(21), 5552-5556.

Solaronix. 2013. Solaronix Delivers the World's First Multi-colored Dye Solar Cell Facade, *solaronix news*. Retrieved on November 7, 2013.

Sommeling, P. M., Späth, M., Smit, H. J. P., Bakker, N. J., & Kroon, J. M. 2004. Long-term stability testing of dye-sensitized solar cells. *J. Photochem. Photobiol.,* **164**(1-3), 137-144.

Späth, M., Sommeling, P. M., Van Roosmalen, J. A. M., Smit, H. J. P., Van Der Burg, N. P. G., Mahieu, D. R., Kroon, J. M. 2003. Reproducible manufacturing of dye-sensitized solar cells on a semi-automated baseline. *Progress in Photovoltaics: Research and Applications,* **11**(3), 207-220.

Takashima, J., Fujii, T., & Furusaki, K. 2008. *Ball Grid Dye Sensitized Solar Cell with Hybrid Copper Polyimide substrate and Carbon Catalyst.* Paper presented at the Electrochemical Society meeting.

Takeda, Y., Kato, N., Higuchi, K., Takeichi, A., Motohiro, T., Fukumoto, S., Toyoda, T. 2009. Monolithically series-interconnected transparent modules of dye-sensitized solar cells. *Sol. Energy Mater. Sol. Cells,* **93**(6-7), 808-811.

Tanabe N. Recent progress in DSC module panel development at Fujikara Ltd. 2010. recent progress in DSC module panel development at Fujikara Ltd. *recent progress in DSC module panel development at Fujikara Ltd,* (Vol. **DSC-IC 2010**).

Toyodaa T, T. S., Jyunji Nakajimaa, Syouichi Doia, Syungo Fukumotoa, Atsushi Itoa, Tomoyuki Tohyamaa, Motoharu Yoshidaa, Tetsuo Kanagawaa, Tomoyoshi Motohirob, Tohru Shigab, Kazuo Higuchib, Hiromitsu Tanakab, Yasuhiko Takedab, Tatsuo Fukanob, Naohiko Katohb, Akihiro Takeichib, Kensuke Takechib, Masahito Shiozawab. 2004. Outdoor performance of large scale DSC modules. *Journal of Photochemistry and Photobiology A: Chemistry, 164*, 203-207.

Thomas, S., Deepak, T. G., Anjusree, G. S., Arun, T. A., Nair, S. V., & Nair, A. S. 2014. A review on counter electrode materials in dye-sensitized solar cells.. *Journal of aterials Chemistry A,* **2**(13), 4474-4490.

Toby Meyer, M. S., Asef Azam, David Martineau, Frédéric Oswald, Stéphanie Narbey, Grégoire Laporte, Robin Cisneros, Giulia Tregnano, Andreas Meyer. 2009. All Screen Printed Dye Sensitized Solar Modules *CleanTechDay 3rd Generation Photovoltaics, CSEM*. Basel: Solaronix.

Ubertini, S., & Desideri, U. 2003. Performance estimation and experimental measurements of a photovoltaic roof. *Renewable Energy*, **28**(12), 1833-1850.

Wang, H., & Hu, Y. H. 2012. Graphene as a counter electrode material for dye-sensitized solar cells. *Energy & Environmental Science*, **5**(8), 8182-8188.

Wang, L., Fang, X., & Zhang, Z. 2010. Design methods for large scale dye-sensitized solar modules and the progress of stability research. *Renewable and Sustainable Energy Reviews*, **14**(9), 3178-3184.

Wang, Q., Ito, S., Grätzel, M., Fabregat-Santiago, F., Mora-Seró, I., Bisquert, J., Imai, H. 2006. Characteristics of high efficiency dye-sensitized solar cells. *J. Phys. Chem. B*, **110**(50), 25210-25221.

Wang, Q., Moser, J. E., & Grätzel, M. 2005a. Electrochemical impedance spectroscopic analysis of dye-sensitized solar cells. *Journal of Physical Chemistry B*, **109**(31), 14945-14953.

Wang, Q., Moser, J. E., & Grätzel, M. 2005b. Electrochemical impedance spectroscopic analysis of dye-sensitized solar cells. *J. Phys. Chem. B*, **109**(31), 14945-14953.

Weerasinghe, H. C., Huang, F., & Cheng, Y.-B. (2013). Fabrication of flexible dye sensitized solar cells on plastic substrates. *Nano Energy, 2*(2), 174-189.

Wei, T. C., Feng, S. P., Chang, Y. H., Cherng, S. J., Lin, Y. J., Chen, C. M., & Chen, H. H. 2012. Fabrication and characterization of interconnected grid-type dye-sensitized solar modules. *Int. J. Electrochem. Sci.*, **7**(12), 11904-11916.

Wei, T. C., Lan, J. L., Wan, C. C., Hsu, W. C., & Chang, Y. H. 2012. Fabrication of grid type dye sensitized solar modules with 7% conversion efficiency by utilizing commercially available materials. *Prog. Photovolt: Res. Appl*.

Wei, W., Wang, H., & Hu, Y. H. 2014. A review on PEDOT-based counter electrodes for dye-sensitized solar cells. *International Journal of Energy Research*, n/a-n/a.

Wirth, H. 2013. Recent facts about photovoltaics in Germany. Germany: Division Director Photovoltaic Modules, Systems and Reliability, Fraunhofer ISE. **5**.86.

Wu, J., Xiao, Y., Tang, Q., Yue, G., Lin, J., Huang, M., . . . Sato, T. 2012. A large-area light-weight dye-sensitized solar cell based on all titanium substrates with an efficiency of 6.69% outdoors. *Advanced Materials*, **24**(14), 1884-1888.

Wu, M., & Ma, T. 2014. Recent Progress of Counter Electrode Catalysts in Dye-Sensitized Solar Cells. *The Journal of Physical Chemistry C*.

Xiaoxu Wang, Guangfei He, Hao Fong, and Zhengtao Zhu. 2013. Electron Transport and Recombination in Photoanode of Electrospun TiO2 nanotubes for Dye-Sensitized Solar Cells. *J. Phys. Chem. C*, **117**, 1641−1646.

Xiong, D., & Chen, W. 2012. Recent progress on tandem structured dye-sensitized solar cells. *Frontiers of Optoelectronics,* **5**(4), 371-389.

Yang, X., Yanagida, M., & Han, L. 2013. Reliable evaluation of dye-sensitized solar cells. *Energy & Environmental Science,* **6**(1), 54-66.

Yella, A., Lee, H.-W., Tsao, H. N., Yi, C., Chandiran, A. K., Nazeeruddin, M. K., Grätzel, M. 201). Porphyrin-Sensitized Solar Cells with Cobalt (II/III)–Based Redox Electrolyte Exceed 12 Percent Efficiency. *Science,* **334**(6056), 629-634.

Yum, J. H., Baranoff, E., Kessler, F., Moehl, T., Ahmad, S., Bessho, T., . . . Grätzel, M. 2012. A cobalt complex redox shuttle for dye-sensitized solar cells with high open-circuit potentials. *Nature Communications,* **3**.1-8.

Zardetto, V., Di Giacomo, F., Garcia-Alonso, D., Keuning, W., Creatore, M., Mazzuca, C., Brown, T. M. 2013. Fully plastic dye solar cell devices by low-temperature UV-irradiation of both the mesoporous TiO2 photo- and platinized counter-electrodes. *Advanced Energy Materials,* **3**(10), 1292-1298.

Zardetto, V., Mincuzzi, G., De Rossi, F., Di Giacomo, F., Reale, A., Di Carlo, A., & Brown, T. M. 2014. Outdoor and diurnal performance of large conformal flexible metal/plastic dye solar cells. *Applied Energy,* **113**(0), 1155-1161.

Zhang, Q., & Cao, G. 2011. Nanostructured photoelectrodes for dye-sensitized solar cells. *Nano Today*, **6**(1), 91-109.

Zhang, X. L., Huang, F., Nattestad, A., Wang, K., Fu, D., Mishra, A., . . . Cheng, Y. B. 2011. Enhanced open-circuit voltage of p-type DSC with highly crystalline NiO nanoparticles. *Chemical Communications*, **47**(16), 4808-4810.

Zhang, Y. D., Huang, X. M., Gao, K. Y., Yang, Y. Y., Luo, Y. H., Li, D. M., & Meng, Q. B. 2011. How to design dye-sensitized solar cell modules. *Solar Energy Materials and Solar Cells,* **95**(9), 2564-2569.

ZSW. 2013. ZSW produces world record solar cell Retrieved 13-12-2013, 2013, from http://www.zsw-bw.de/uploads/media/pi18-2013-ZSW-WorldrecordCIGS.pdf. Retrieved on 24 October 2013.

Appendix I

Table 2.2: Globally emerged commercial companies on dye-solar cells/modules developments. The statistics are taken from their websites/published reports on websites and Fakharuddin A. et al. (2014d), unless stated otherwise.

No	Company	Affiliation	Core Business	Major Achievements in DSCs
1	S Samsung SDI	Korea	Electronic devices such as LCDs, mobile phones, and more recently energy storage and harvesting devices	Dye solar panels for BIPVs, smart windows with integrated storage, tandems DSPs.
2	SHARP	Japan	Electronic products	Certified η of 11.9% in single cells by tuning haze effect, certified highest module PCE (8.2 %) in W-type module, cost effective back contact DSCs, 8.1% η in quasi *s*-DSCs.
3	G24 Power	UK	Solar power especially third generation PVs	Started DSC plant in 2007 (18000 sq. ft), flexible water proof bags, commercial application for indoor electronics, roll-to-roll processing capability of 800m in ~ 3hrs, specialized in indoor electronics such as key-boards, mouse, e-book cover, solar bags, MP3 etc.
4	Konarka	USA	Spinout company of MIT for DSCs	Licensed it DSC IP to G24.
5	Dyesol	Australia	DSCs materials and commercial development	DSMs, BIPVs, Integration of DSCs in roof material (in process), *s*-DSMs and *f*-DSMs. Developing DSMs and *s*-DSMs.
6	Solaronix	Switzerland	DSCs materials and commercial development	Panels of an active area ~200m^2 are shipped for EFPL with an estimated annual production of 2000kWh. Developing DSMs and materials for solar cells/modules.
7	Dynamo	Sweden	DSCs materials and commercial development	Preparing Co-based electrolytes and Porphyrine dyes.
8	Oxford PVs	UK	*s*-DSMs, PSMs	Currently working on perovkite solar modules.
9	Dyepower	Italy	Development of DSM for BIPV and facades	Running an automated pilot line for the production of A4 size DSMs and for larger area strings/panels. UV, humidity-freeze and damp-

			applications	heat IEC 61646 stability tests successfully passed on A4 size modules.
10	EFPL	Switzerland	Organic PVs, materials and characterization	Held the main patent on mesoporous dye solar cells structure. Highest uncertified η in DSCs (13%), one of the highest η in perovskite based solar cells (15%), the first report on DSMs in 1996 (monolithic series modules (10×10 cm^2) with η ~ 6%.
11	Fujikura	Japan	Optical fibers	Developing DSCs for both outdoor applications and indoor electronics such as mobile phones, testing ionic liquids and gel-electrolytes in modules, thermal stability and outdoor testing of more than 200 sub modules (20 cm^2) modules passed IEC 61646 (stability test).
12	3G Solar	Israel	DSCs technology	Installed DSC mini modules to charge computer peripherals, surveillance cameras, electronic bracelets and medical devices.
13	CSIRO	Australia	Research agency	Colorful and transparent DSMs for BIPVs, materials for cost-effective DSCs.
14	Taiyo Yuden Co. Ltd	Japan	Electronic components	Flexible DSC using Ti foil as counter electrode for a sub module of 15×15 cm^2 (o.3 mm thin), test race car using 2×8 m^2 connected sub-modules in world solar car rally in 2008 and achieved a speed of 11.8 km/h in cloudy weather which was almost similar to 12.5 km/h in sunny weather.
15	SONY Technology Centre	Japan	Electrical appliances	Started research on DSC in 2001, applications for terrestrial power and indoor electronics, achieved 11.1 % confirmed η in 2009 (APL, 94(073308)), W-type module designs utilizing 85% active area, “Hana-akari”a solar lamp powered by DSCs developed,
16	Shimane Institute of Technology	Japan	Governmental organization	J2 dye, large area DSC (1.25m × 0.75 m) developments and stability testing for 1000 h at 80 ^{o}C, ‘EneLEAF’ in collaboration with Nissha. Ltd.
17	Toyota/ Aisen Seiki	Japan	Components and systems for automotive industry	One of the earlier industrial R&D on DSMs, S-type monolithic connections, stability test in outdoor exposure in 2006 for 2.5 years.
18	Peccell	Japan	Venture company of Toin	Plastic modules of DSCs, 4 V in a serially connected module of 10 ×

	Technologies, Inc.		University of Yokohama	10 cm^2, The world largest fully developed plastic modules (0.8 × 2.1 m) is the lightest DSMs weight (800g/m^2) with a capability of providing >1000 V.
19	Eneos Co. Ltd	Japan	Iol company but established a joint sub company named as ‘Sanyo Eneos Solar Co. Ltd.’	Bi-layer photoanodes, solid state DSMs (10 ×10 cm^2).
20	NGK Spark Plug Co., Ltd.	Japan	Spark plugs	Started DSC research in 2003, adopted lithography in monolithic module fabrication, founder of ball grid DSC structures which replace Pt for catalysis purpose and utilizes 95% active area.
21	ITRI Taiwan (Industrial Tech. Research Inst. Of Taiwan)	Taiwan	Applied research and technical services	Transferred technology to Formosa Plastics and the mass production is expected at 2015.
22	Mitsubishi paper mills	Japan	Paper, pulp, and photosensitive materials	D-series dyes or indoline dyes perform better with ZnO due to metal free nature.
23	Panasonic Denko Co. Ltd.	Japan	Branch company of Panasonic, electronic appliances	See-through modules for indoor applications, stability testing and encapsulation to prevent electrolyte leaking, use of K9 dye instead N719 to improve stability.
24	KIST (Korean Ins. Of Sc. and Tech.)		Material for DSCs and device development	Flexible DSC especially stainless steel based devices with η ~4.2% higher than plastic based DSCs, molecular engineering helped in achieving an PCE of 11% at their labs, the technology is transferred to Dongjin Semichem Ltd.
25	J touch Taiwan	Taiwan	Touch panel solutions	Started indoor electronic by DSCs such as in portable time clocks.
26	Fraunhofer ISE	Germany	Environmentally friendly energy harvesting and storage research	Scalable development and stability research on DSMs, first large area (30 ×30 cm^2) glass frit based module design with thermal stability testing till 80 ^oC.
27	Institute of plasma Physics	China	Utilization of the fusion energy	500 W DSC power station was installed in 2004 with η ~5.9% in parallel module, research is oriented on photoanode optimization,

	(CAS, China)			device packaging and interconnections.
28	ECN (energy research center of the Netherlands)	Netherlands	Energy research institute	First EU lab for DSC development started in 1995, stability tests for 1000 and 10,000 h, introduced master plate design, installed semi-automated DSC manufacturing up to 100 cm^2.
29	Gunze Ltd.	Japan	Electronic components and garments	Wearable DSC a unique application (28 cells with required electronics are attached to a jacket and used as mobile charge).
30	Yingkou OPV Tech New Energy Co., Ltd.	China	Up scaling DSCs/DSMs	Colorful, artistic and transparent DSMs in form of glass windows, and screens. Flexible and portable DSMs are also manufactured and available for commercial use.
31	Ricoh	Japan	Electronic (imaging and printing device, for example)	*s*-DSMs for indoor lighting.
32	Merck	Germany	Chemicals and pharmaceuticals	Electrolytes for DSCs, precursors for various photoanode materials.
33	Acrosol	Korea	Research & development, solar panel manufacturer	NA
34	NLAB Solar(name changed to exeger)	Sweden	Industrial production of DSMs	Pilot plant installed for the production of DSMs as BIPV and AIPV.
35	Dyetec Solar (Dyesol-Pilkington JV)	USA/Global	DSMs in BIPV	Joint venture of Dye-sol and Pilkington.
36	Tata Steel Europe	India	Steel roofing	Joint venture of Dye-sol and Tata Steel.

Appendix II: Summary of DSMs development

Table 3: A comparison of PV performance and devices designs of a few DSMs is listed. The percentage of active to total area is also given for a meaningful comparison. Adopted from Fakharuddin A. et al., 2014d.

Connection type	Active Area (cm^2)	Active to total area	I_{SC} (mA)	V_{OC} (V)	FF	η (%)	Comments
Parallel (grid coated)	68	68%	NA	0.7	0.65	4.3	These designs are mostly grid coated using Ag or other metals such as Ni. This type of connection results in enhanced current density but creates stability issues in device. To avoid metallic grid exposure to electrolyte, it should be encapsulated into sealant thus adding complexity to fabrication process. The advantage of these designs is a more simple power management at the individual DSM level compared to series design where high levels of current matching are required. These designs also survive reverse bias degradation.
	187	62.3%	1296	0.7	0.52	4.84	
	81	81%	820	0.7	NA	4.3	
	75	NA	50	0.76	0.7	5.7	
	2246	63%	2100	9	0.62	5.9[a]	
	18	73%	235	0.63	0.67	5.47[b]	
	151	67%	2287	0.72	0.68	7.4[c]	
	15.12	60.5%	172	0.75	0.66	5.52	
Series+ Parallel	110	NA	120	2.2	NA	NA	This design reduces active area available on photoelectrode and provides lower J_{SC} but multiplies V_{OC}. The design is not widely adopted and has minimal scope for commercialization.
	NA	NA	23.45	1.85	0.58	3.19[d]	
	90	50	287	1.4	0.56	5.9	

Z-type	43	73	51	9	0.65	7	Z-type DSMs provide good performance and high active area. However they can suffer from lower FF due to excess interconnections which adds to series resistance. Careful encapsulation of vertical connections is necessary.
	47.5	47%	58	7.7	0.68	6.6	
	505	74%	169	20	0.53	3.5	
	512	73%	140	29	0.58	4.5	
W-type	25.5	85%	54	6.3	0.61	8.2^e	The highest certified efficiency reported in any DSM. However care design for current matching is required.
Series	19.75	94%	28.55	3.9	0.61	5.29	Any mismatch of current in cells will affect efficiency of the module.
Monolithic	90.25	90.25%	40	9	~0.6	<2.5	This design yields lower current density.
Ball Grid	80	95%	~1200	0.76	NA	~8%	Very high active area, similar performance of that of a single cell.
DSCs (Single cells)	~0.2		4.6	0.91	0.78	13	Routinely reported J_{SC} values in best performing *l*-DSCs.
	0.2	--	~4.6	0.93	0.74	12.3	
	0.22	--	4.57	0.73	0.72	11.1	
***s*-DSMs**	100	~45%	37	5.16	0.47	0.8	Pore-filling, lower photoelectrode thickness, high stability
	625	46%	28	10.6	0.35	0.32	
	112	52%	20	8	NA	0.9	
	2.25	NA	20	0.62	0.50	2.8	
	8	NA	~35	1.5	0.47	~2.5	
	13.5	54%	21.5	3.2	0.39	2	

sDSCs	0.2	--	19.2	0.73	0.73	10.2[f]	The highest efficiency solid state laboratory scale device.
Flexible DSMs	58	~60-70%	47	6.5	0.33	~3	Devices fabricated on conducting plastic (PET/ITO) or metallic substrates such as Titanium foil.
	900	NA	77	6.7	<0.5	2-3%	
	5.4	NA	69[g]	0.76	0.54	4.8	
	16.4	69%	30	3.8	0.53	3.3	
	100	90%	727	0.72	0.73	6.7[h]	
Large area panels	2246	63%	2100	9	0.62	5.9[a]	As per the definition of DSPs in section 5.3, large area panels are ≥ 1000 cm^2.
	14000	74%	945[i]	4.5	0.56	3.58	
	6000	48%	--	--	--	2.3	

[a] At 0.84 sun, 64 series and parallel connected DSMs;
[b] η 7% at 0.5 sun;
[c] CE consist of mixed Ti:Pt;
[d] 3D wire shaped DSM tree, I-V measured at 0.87 sun;
[e] the highest certified η in DSMs;
[f] reported η is without a mask;
[g] calculated with respect to active area only;
[h] Ti Foil as a substrate and photovoltaic performance is reported at 55 mW/cm^2;
[i] the reported photocurrent is only for a single DSM of area ~700 cm^2.

Appendix III: Peel Off test

“To confirm adhesion of mesoporous layer peel off test is carried out. In this test, an adhesive tape is pasted on a sintered TiO_2 film and then it is removed. If the paste is peeled off from the FTO, its adhesion with FTO is not considered well.”

Appendix IV: XRD of dye-anchored TiO_2 films

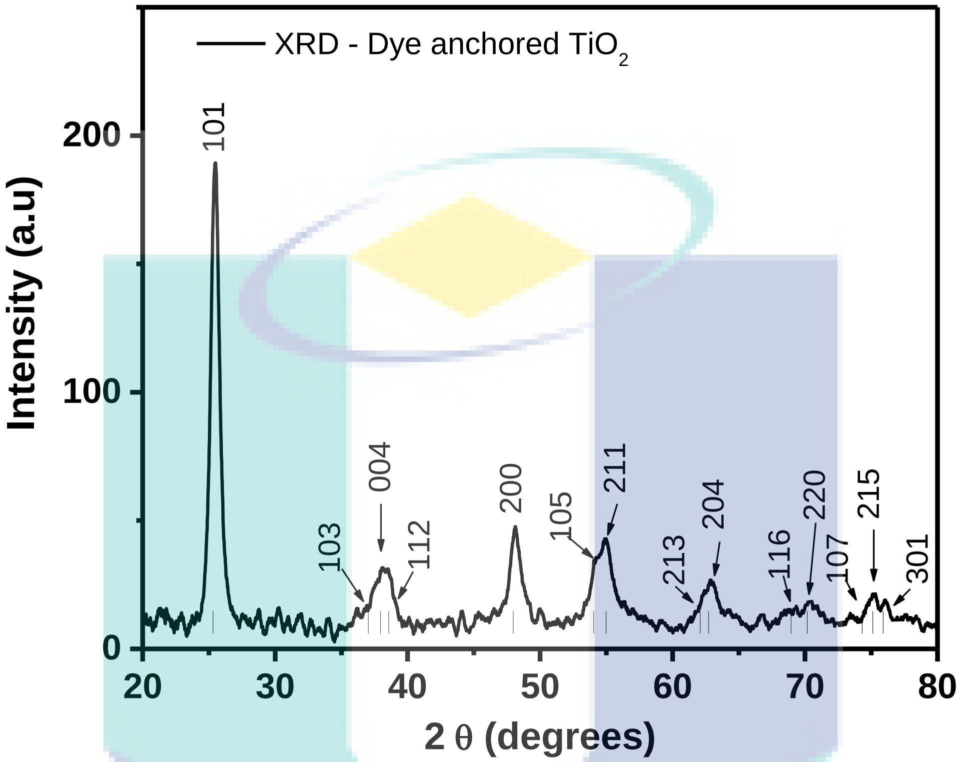

Figure: XRD pattern of dye anchored-TiO_2 .

Appendix V: Calculation of dye loading

The dye-loading is measured by desorption test. To calculate the amount of dye-anchored on a FTO, the anchored dye is first desorbed in 0.1 M NaOH in water/ethanol solution (1:1 vol ratio). The concentration of desorbed solution is thus calculated by measuring its absorption spectra and using Beer/Lambert equation ($c = (A/ \varepsilon l)$).

where c is the dye concentration, A is the absorbance, ε is the extinction coefficient, and l is the length of the optical path. The values of extinction coefficient are taken from literature and are 1.47×10^4 mol/cm^3 and 1.58 × 104 mol/cm^3 for N3 and N719 dyes respectively.

To convert the concentration into amount of dye absorbed on a unit area (t), we used the relation t = c*v*/s, where *v* is the volume of the dye solution and s is the area of the photoanode film.

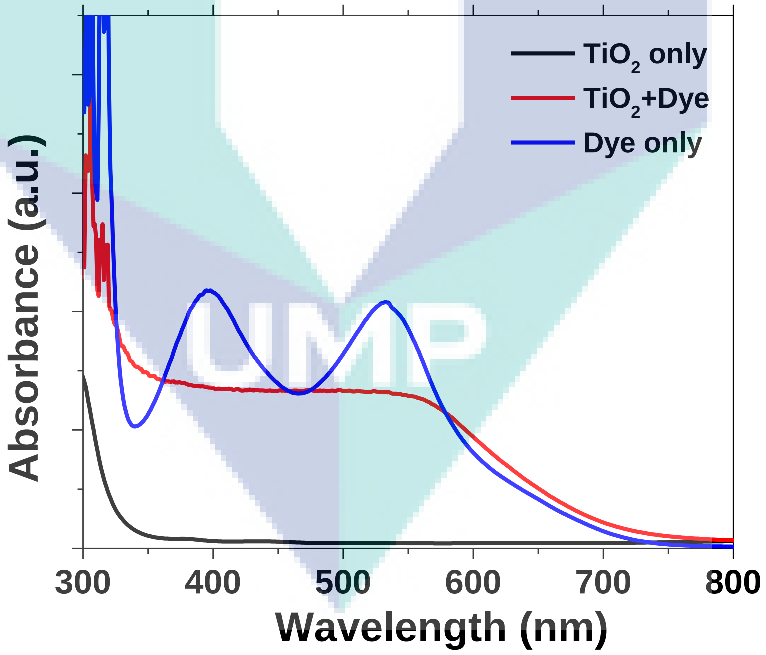

Figure: Absorbance of a typical TiO$_2$ film before and after dye anchoring.

Appendix VI: Publications list

1. **Fakharuddin A**., Di Giacomo F., Ahmed I., Wali Q., T.M. Brown, R. Jose. Role of morphology and crystallinity of electron transport layer on long term durable performance of perovskite solar cells (accepted), **J. Pow. Sources**, Jan 2015.

2. Ahmed I**., Fakharuddin A.,** Wali Q., Zainun A. R., Ismail J., R. Jose., " Mesoporous titania–vertical nanorod films with interfacial engineering for high performance dye-sensitized solar cells", **Nanotechnology** (accepted). Jan. 2015.

3. **Fakharuddin, A.;** Brown T. M. Fabregat-Santiage F., R. Jose; Bisquert J., "A perspective on the commercial production of dye-solar modules". **Energ. & Environ. Sci**. 2014, 7, 3952.

4. **Fakharuddin, A.;** I. Ahmed.; Kalidin, Z.; Yusoff, M. M.; R. Jose, "Charge transport in dye-solar cells stacks". **J. App. Phys**. 115(16), 2014.

5. **Fakharuddin, A.;** I. Ahmed.; Kalidin, Z.; Yusoff, M. M.; R. Jose, Channeling of electron transport to improve collection efficiency in mesoporous TiO_2 dye sensitized solar cell stacks. **App. Phys. Lett**. 104, 053905 (2014).

6. Wali Q, **Fakharuddin A.**, Ahmed I., Hasbi Mohd. Ab R., Ismail J., R. Jose. "Multichannel nanotubes of SnO2 by electrospinning for high efficiency dye-sensitized solar cells", **J. Mat. Chem. A.** 2014.

7. Giacomoa, F.D.; Zardettoa, V.; Ahmed, I.; **Fakharuddin A.;** R. Jose; Brown T.M.; Carlo A.D;, "TiO2 for hybrid solar cells and its application in large area plastic dye solar cells and high efficiency perovskite solar cells" **HOPV-2014**, Amesterdam, The netherlands. P-65 (online abstract).

8. **Fakharuddin, A.;** I. Ahmed.;Q. Wali.; Khalidin, Z.; Yusoff, M. M.; R. Jose, Probing Electron Lifetime and Recombination Dynamics in Large Area Dye-Sensitized Solar Cells by Electrochemical Impedance Spectroscopy, **Adv. Mater. Res.** Vol. 295 (2014) pp 553-558.

9. **Fakharuddin, A.;** Archana, P. S.; Kalidin, Z.; Yusoff, M. M.; R. Jose, Standardization of photoelectrode area of dye-sensitized solar cells, R. ***RSC Advances***. **2013**, *3*, 2683-2689.

10. **Fakharuddin, A.;** Archana, P. S.; Khalidin, Z.; Yusoff, M. M.; R. Jose, On the scalability of dye-sensitized solar cells: Effects of photoelectrode area on the photovoltaic and charge transport parameters, **AB. AM. CHEM. SOC**. 245(2013).

Patents

1. **A. Fakharuddin,** Z. Khalidin, M. M. Yusoff, R. Jose, " A dye sensitized solar cell device", PI2013000529 (6 March 2013).

2. **A. Fakharuddin,** Qamar wali, Z., Z. Khalidin, R. Jose "Nanowires based dye solar modules" applied 2014.